

*Fabrication and Characterisation of III-V
Semiconductor Nanostructures*



**AALBORG
UNIVERSITY**

STUDENT REPORT

MASTER'S THESIS

GROUP B

PHYSICS

AALBORG UNIVERSITY

SUBMITTED: 3RD OF JUNE 2021

TITLE SHEET



AALBORG
UNIVERSITY

STUDENT REPORT

10. Term Physics

Department of Materials and
Production

9000 Aalborg

Title:

Fabrication and Characterisation of
III-V Semiconductor Nanostructures

Project:

Master's Thesis

Project Period:

February 2021 - June 2021

Project Group:

Group B

Participants:

Matilde Kammer Sandager
Mads Blach Rossen Bjerring
Hans Christian Bonde

Supervisor:

Vladimir Popok

Number of Pages:

79

Number of Appendix Pages:

9

Abstract:

Controlled growth of III-V semiconductor nanostructures is of interest due to a vast amount of applications. For instance, the piezoelectric response of nanowires (NWs) has gained interest in energy harvesting and the optical response for light emitting diodes. The properties of NWs are highly reliant on the initial stages of nucleation, as well as the employed growth method. Hence, the nucleation stage of AlN and growth of nanostructures by DC magnetron sputtering has been investigated. Catalyst-assisted metal-organic chemical vapour deposition (MOCVD) was also tested for the NW formation. Characterisation of the electrical and structural properties of molecular beam epitaxy (MBE) grown GaN NWs was conducted as well.

Structural and electronic properties of ramified islands formed during AlN magnetron sputtering has been analysed using atomic force microscopy (AFM), Kelvin probe force microscopy (KPFM) and scanning electron microscopy (SEM), revealing "magic" heights in steps of approximately 5.3nm and a surface coverage that stabilises at 14%. The most probable reason for the island formation is suggested to be pre-sputtering of Al needed for the target cleaning. Thus, adjustment of the process is required for the growth of pure AlN structures. Formation of columnar AlN NWs using reactive magnetron sputtering has not been achieved. Flower-like structures with lamella components have been obtained. Tests of different processing parameters allowed for the development of a strategy towards controlling the AlN NW growth. Similar flower-like structures were also obtained using MOCVD and further research on the growth parameters tuning is required. MBE grown GaN NWs showed temperature dependent NW surface densities, where NWs were found to exhibit mixed polarity of both Ga- and N-facets.

PREFACE

This Master Thesis has been carried out by students at the Faculty of Materials and Production at Aalborg University.

We would like to express our sincere gratitude for the valuable feedback and meaningful discussions provided by our supervisor *Associate Professor Vladimir N. Popok*, both in this thesis and throughout our time at Aalborg University. His insights into the world of material science has motivated us all to pursue this field of physics during our degrees and in our future careers.

We are thankful for the time and effort of *Professor Zbigniew Zytkeiwicz* from the Institute of Physics at the Polish Academy of Sciences, who provided us with MBE-grown nanowires, along with a great e-mail correspondence concerning the sample information and useful literature.

The guidance and assistance during laboratory work provided by *Research Technician Peter Kjær Kristensen*, has been fundamental for the production and analysis of the samples presented in this thesis, for which we are very grateful.

A restoration of the MOCVD system, as well as a detailed introduction describing its working principles, have been provided by *Academic Officer Deyong Wang*, for which we truly appreciate.

All references in this project has been cited as follows: [xx,p. a], where xx indicates the reference number in the bibliography and a provides the page of the given source.

A list of abbreviations commonly used in this thesis is found in the table below

Abbreviation	Meaning
AFM	Atomic Force Microscopy
CPD	Contact Potential Difference
DC	Direct Current
DFT	Density Functional Theory
EDX	Energy Dispersive X-Ray
FET	Field-Effect Transistor
FM	Frank-Van der Merwe
GLAD	Glancing Angle Deposition
HEMT	High-Electron-Mobility Transistor
TEM	Transmission Electron Microscopy
HRTEM	High-Resolution Transmission Electron Microscopy
KPFM	Kelvin Probe Force Microscopy
LED	Light Emitting Diode
LLC	Load Lock Chamber
MBE	Molecular Beam Epitaxy
ML	Mono Layer
MOCVD	Metal-Organic Chemical Vapour Deposition
NW	Nanowire
PVD	Physical Vapour Deposition
RMS	Root Mean Square
RPM	Rounds Per Minute
SAG	Selected Area Growth
SAW	Surface Acoustic Wave
SC	Sputtering Chamber
SCCM	Standard Cubic Centimetres per Minute
SEM	Scanning Electron Microscopy
SK	Stranski-Krastanov
STM	Scanning Tunneling Microscopy
SZM	Structure Zone Model
TC	Transfer Chamber
UHV	Ultra-High Vacuum
VLS	Vapour-Liquid-Solid
VSS	Vapour-Solid-Solid
VW	Volmer-Weber
WZ	Wurtzite
XRD	X-Ray Diffraction
ZB	Zinc Blende

RESUMÉ

I halvlederindustrien forsøger man altid at skubbe grænserne for, hvad der er muligt indenfor anvendelser og optimering af forskellige apparater. De seneste år har der været en stigende interesse for halvledere som GaN, AlN og AlGaN, med stort fokus på ikke blot at udnytte egenskaber såsom båndgab, elektronmobilitet og termisk ledeevne [1], men også på at konstruere materialerne i bestemte strukturer med henblik på at øge deres ydeevne.

Ved at gro disse materialer med en velorienteret krystallinitet og i bestemte strukturer, som eksempelvis endimensionelle nanowires, kan en yderligere optimering af LEDer [2] og FETer [3] realiseres. Særligt i de piezoelektriske egenskaber af nanowires eksisterer der en udpræget interesse, blandt andet på grund af deres anvendelse indenfor energihøstning [4][5].

Halvledernanowires kan fabrikeres ved brug af en række forskellige teknikker. Fællesnævneren for dem alle, er at opbygning af en nanowire sker gennem overførslen af partikler i gasfasen til en overflade på et substrat, hvor de krystalliserer i den ønskede struktur.

Groning af nanowires kræver dog, at deponeringsparametrene lever op til specifikke krav, eller at substratet forbehandles på en sådan måde, at adsorberede atomer tvinges til at fastlægge sig i prædefinerede mønstre. Ikke blot er der udfordringer i forbindelse med groning af vertikale strukturer, men krystalkvaliteten og støkiometrien er også vigtige for, at de ønskede egenskaber opnås, hvilket også afhænger af groningsprocessen.

Ofte anvendte metoder for nanowire-groning inkluderer metalorganisk kemisk gasfasedeposering, molekylærstråleepitaksi og magnetronspøttering. De første to metoder er mere veletablerede når det kommer til fremstilling af nanowires, mens den sidstnævnte kræver yderligere raffinering, før kommerciel brug er en realitet.

Af disse årsager omhandler dette speciale de tre forskellige metoder, som kan bruges til at gro nanowires. Metoderne, samt deres fordele og ulemper, vil blive præsenteret med det formål at give indsigt ind i, hvordan de forskellige parametre har indflydelse på groningen af nanostrukturer. Dette gøres med henblik på at opnå forståelse for, hvordan groning i den vertikale retning kan fremmes.

Ud fra denne motivation, er forskellige AlN-prøver blevet produceret, både ved hjælp af substratbehandling med katalysatorer, men også gennem justering af de parametre, som kan påvirke groningsprocessen. Prøver med GaN-nanowires er blevet tilsendt af Professor Zbigniew Zytckiewicz fra Institutet for Fysik ved det Polske Akademi for Videnskab. Analysen af prøverne består i strukturbestemmelse gennem scanning-elektronmikroskopi og atomisk kraftmikroskopi. Yderligere kompositionelle og elektriske egenskaber er henholdsvis blevet undersøgt ved energidispersiv røntgenspektroskopi og Kelvin probe kraftmikroskopi.

Begyndelsen af groningsprocessen er af interesse, da denne lægger fundamentet, hvorpå resten af groning bygger. Derfor er øer af AlN groet gennem magnetronsputtering analyseret. Det blev fundet, at disse øer eksisterer i bestemte "magiske" højder på cirka 5.3nm. Disse øers dækning af substratoverfladen viste sig at stabilisere omkring 14%. Ø-formationen er en effekt, som stammer fra den indledende rensning af Al-targetet, der udføres i sputtersystemet. For at opnå groning af ren AlN, er det nødvendigt at undersøge denne process yderligere.

Søjlelignende strukturer af AlN blev groet med magnetronsputter, men der opnåedes ikke groning af fritstående nanowires. Blomsterlignende strukturer blev dannet ved metalorganisk kemisk gasfasedeponering, men yderligere undersøgelser af groningsprocessen er nødvendige, før nanowires kan produceres. Molekylærstrålepitaksigroede nanowires udviste stærkt temperaturafhængige overfladedensiteter, og forskellige polariteter blev fundet med Kelvin probe kraftmikroskopi.

CONTENTS

1	Introduction	9
2	Structure and Properties of AlN and GaN	10
2.1	Wurtzite Structure	10
2.1.1	Planes and Directions	11
2.1.2	Nanowire Polarity	11
2.1.3	Surface Energies	13
2.2	Microstructural Defects and Lattice Mismatch	14
3	Formation of Nanostructures	18
3.1	Crystal growth	18
3.1.1	Equilibrium Growth Modes	18
3.1.2	Kinetics of Crystal Growth	19
3.1.3	Nucleation of Crystals	20
3.2	Nanowire Growth Mechanisms	21
3.2.1	Selective Area Growth	21
3.2.2	Catalyst-Assisted Growth Mechanisms	22
3.2.3	Catalyst-Free Growth Mechanisms	24
4	Growth of Nanowires	26
4.1	Molecular Beam Epitaxy-Grown Nanowires	26
4.1.1	Review of Nanowires Grown by Molecular Beam Epitaxy	27
4.2	Metal Organic Chemical Vapour Deposited Nanowires	31
4.2.1	Review of Nanowires Grown by Metal Organic Chemical Vapour Deposition	31
4.3	Magnetron Sputter Deposited Nanowires	36
4.3.1	Review of Nanowires Grown by Reactive Magnetron Sputtering	36
5	Experimental	40
5.1	AlN Island Grown by DC Magnetron Sputtering	40
5.2	Nanowires Grown by MOCVD	41
5.3	Nanowires by MBE	42
5.4	Sample Preparation and Analysis	42
6	Results and Discussion	44

6.1	Nucleation of Ramified Islands	44
6.1.1	Formation of Islands under AlN Magnetron Sputter Deposition	44
6.1.2	Formation of Islands during Preliminary Target Cleaning	49
6.1.3	General Considerations for Ramified Island Growth	54
6.2	AlN Structures Grown by DC Magnetron Sputtering	55
6.2.1	Catalyst-Free AlN Nanostructures	55
6.2.2	Catalyst-Assisted AlN Nanostructures	56
6.3	Morphology and Composition of AlN Nanostructures Grown by MOCVD	58
6.4	GaN Nanowires Grown by MBE	64
6.4.1	Morphology of GaN Nanowires	64
6.4.2	Electrical Properties of GaN Nanowires	67
7	Conclusions	69
	Bibliography	72
	Appendix A Growth Parameters of Samples Grown Using DC Magnetron Sputtering	80
	Appendix B Growth Parameters of Samples Grown Using MOCVD	83
	Appendix C Growth Parameters of Samples Grown Using MBE	84
	Appendix D Coverage Analysis of Ramified Islands	85
	Appendix E Al Cluster-Chain Formation	86
	Appendix F The Structure Zone Model	87
	Appendix G Distribution Analysis of Nanowire CPD	88

INTRODUCTION

The practical applications of semiconductor nitrides such as GaN, AlN and ternary alloy AlGaIn are almost endless due to their intrinsic material properties. The combination of thermal conductivity, high electron mobility, inherent bandgap and high breakdown voltage makes them excellent candidates for a large number of electronic devices in various fields of research [1]. In the world of thin film fabrication, these materials allow construction of SAW devices [6][7] and HEMTs [8], just to name a few.

These material properties may be further exploited by arranging the grown material into vertical 1D nanostructures. Specifically the growth of nanowires (NWs) show great promise in the improvement of existing applications, as well as development of new ones [9]. By using NWs it is possible to optimise LEDs [2], manufacture improved FETs [3] and generate high piezoelectric responses for energy harvesting purposes [4][5].

The aforementioned NWs may be fabricated by several methods, where the preferred techniques are molecular beam epitaxy (MBE) and metal-organic chemical vapour deposition (MOCVD). A widely used industrial technique is reactive magnetron sputtering, however the growth of AlN and GaN NWs is underdeveloped. The desired nanostructure is achieved either by careful calibration of the growth environment, or by preliminary treatments of the substrate, in order to promote vertical growth. A crucial step in achieving high performing nano-devices is optimising the orientation, crystal quality and stoichiometry of the finished structures. Thus, the growth behaviour of NWs are of particular interest in order to realise the desired properties.

This thesis is concerned with the growth and characterisation of AlN and GaN NWs deposited by both catalyst-assisted and catalyst-free methods, using MBE, MOCVD and reactive direct current (DC) magnetron sputtering techniques. Hence, the growth modes of these techniques will be emphasised, both through theoretical considerations and by a review on state-of-the-art NW growth. The initial nucleation stage is of crucial importance when pursuing vertical growth, and as such, the early growth stages of DC magnetron sputtered AlN nano-islands will be studied by atomic force microscopy (AFM), scanning electron microscopy (SEM) and Kelvin probe force microscopy (KPFM). Furthermore, the deposition parameters during catalyst-assisted MOCVD growth of NWs will be explored by SEM and energy-dispersive X-ray spectroscopy (EDX). Lastly, MBE grown NWs will be structurally and electrically characterised by SEM, AFM and KPFM.

STRUCTURE AND PROPERTIES OF AlN AND GaN

The applications of III-V nanostructures are dependent on their unique properties. This thesis is mainly concerned with AlN and GaN, hence, this chapter will be dedicated to understanding their structure and properties.

2.1 Wurtzite Structure

AlN and GaN are III-V semiconductors typically exhibiting a hexagonal wurtzite (WZ) structure containing two group III and two group V atoms, as illustrated by the WZ unit cell in Fig. 2.1(a). Each unit cell is made up of three lattice vectors \vec{a}_1 and \vec{a}_2 with equal magnitude and an angle of 120° between them, and a vector \vec{c} which is perpendicular to the former two [10, p. 11]. The lattice constants of the WZ structures are summarised for AlN and GaN in Tab. 2.1 along with their bandgap energies, E_g [11, p. 6]. The unit cell atoms can also be represented by two interpenetrating tetrahedrons aligned along the c -axis [12] as shown in Fig. 2.1(b).

Table 2.1 Lattice constants a and c for AlN and GaN, along with corresponding bandgap energies.

	a	c	E_g
AlN	3.11Å	4.98Å	6.28eV
GaN	3.19Å	5.19Å	3.43eV

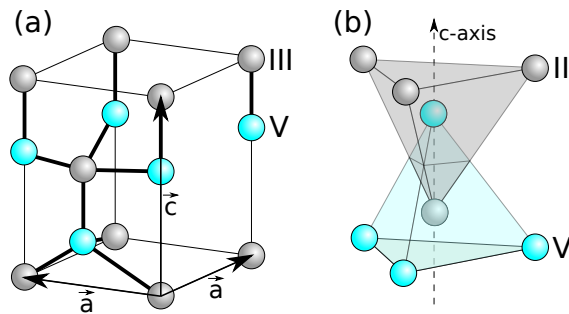


Figure 2.1 (a) Illustration of a WZ unit cell along with the lattice vectors. (b) shows the tetrahedrons formed by identical atoms in the cell. Inspired by [13, p. 5].

2.1.1 Planes and Directions

The directions and planes in crystal lattices are important when investigating properties and characterising their growth directions, e.g. using X-ray diffraction (XRD) [14]. Particularly for hexagonal crystals the use of four-index Bravais-Miller notation, $hkil$, is instructive, where $i = -h - k$ [15, p. 108]. With this notation, the symmetry of different planes become more apparent. Various brackets are used to assign different meanings to the numbers: $(hkil)$ denotes a plane, $[hkil]$ a direction perpendicular to the plane, $\{hkil\}$ a family of planes and $\langle hkil \rangle$ a family of directions [16, p. 56]. Negative values of any of their constituent integers are shown with a bar above it, such that $(hki-l) = (hki\bar{l})$. The family of planes $\{0001\}$, $\{1\bar{1}00\}$ and $\{11\bar{2}0\}$ in a WZ cell are usually referred to as c -, m - and a -planes, respectively. The m - and a -planes are perpendicular to the c -plane. An illustration of different planes in a hexagonal cell are shown in Fig. 2.2.

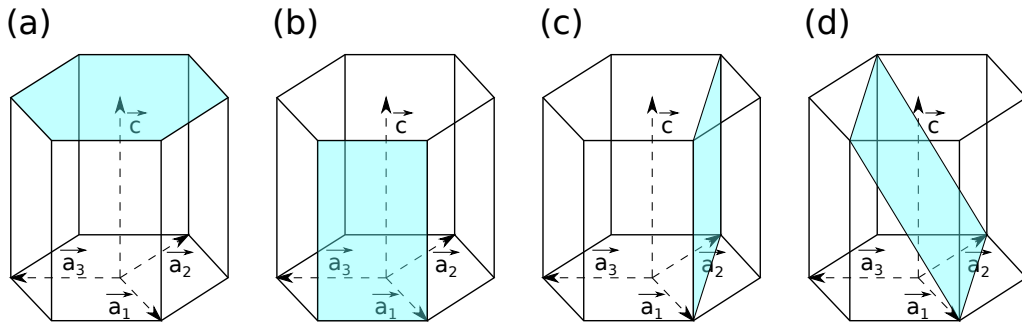


Figure 2.2 Some of the important planes in the WZ unit cell (a) the (0001) - or c -plane, (b) $(1\bar{1}00)$ - or m -plane, (c) $(11\bar{2}0)$ - or a -plane and (d) a semi-polar $(11\bar{2}2)$ -plane. Inspired by [11, p. 11].

Due to the lack of inversion symmetry in AlN and GaN, the (0001) - and $(000\bar{1})$ -planes are not equivalent. The (0001) -plane ends with group III atoms at the face and the $(000\bar{1})$ -plane with group V, making them polar [17]. These planes are often referred to in terms of their III-V constituents. For instance, one would call the GaN (0001) -plane Ga-polar and the $(000\bar{1})$ -plane N-polar. The m - and a -planes (see Fig. 2.2) are non-polar. Any plane inclined between the polar and non-polar planes are called semi-polar, such as the $(11\bar{2}2)$ -plane [18].

2.1.2 Nanowire Polarity

The III- or V-polarity introduced above influences the charge density at the top and bottom facets of NWs, and are thus of interest for fabrication of electronic devices. For instance NW based LEDs [19] and energy harvesting devices [20] are polarity sensitive, as the local band-bending and piezoelectric effects are altered for different polarisations. The polarity of GaN NWs are of particular interest in this thesis, as these will be analysed in Ch. 6. Hence, the remainder of this section will introduce the measuring techniques and characteristics of polarity in GaN NWs.

Techniques for polarity investigations are plentiful [21][22][23], but the use of Kelvin probe force microscopy (KPFM) allows for a non-destructive and large scale option, which makes statistical considerations on the number of different polarities easier [22][24][25].

The difference in work function of Ga- and N-polar NW tops [26] can be measured by KPFM. The local contact potential difference (CPD) has been found to be lower for N-polar NWs as compared to Ga-polar [24], which is used for identifying the polarity of individual NWs. However, this is not generally agreed upon in literature, as others find the reverse relation [22][26]. Variations in the CPDs are also found in different studies, which may be due to the specific material of the AFM tip used, local humidity or surface oxidation.

Hetzl et al. [24] studied the polarity of GaN NWs by KPFM, and found that the N-polar surfaces exhibited lower CPD than the Ga-polar, as compared to a reference sample of known polarity. One of their KPFM measurements are found in Fig. 2.3.

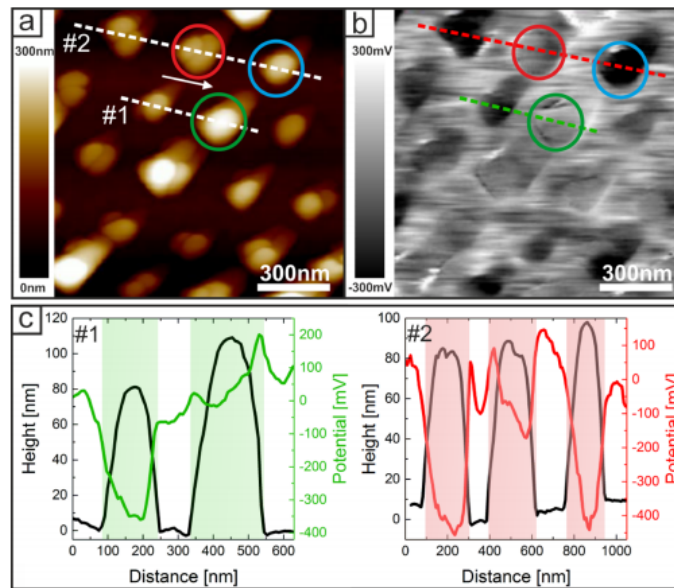


Figure 2.3 KPFM measurements of GaN NWs (a) topography, (b) CPD map, (c) line profile of the topography and CPD of line 1 shown in (a) and (d) line profiles formed by line 2. Reprinted with permission from [24]. Copyright 2017 American Chemical Society.

The dotted lines indicated by 1 and 2 in Fig. 2.3(a) and (b) indicate the placement of the respective topography and CPD measurement profiles shown in the left and right panels in (c). A clear correlation between the topography and CPD of NWs with similar heights was found, where the low CPD NWs (indicated by a blue circle) were classified as N-polar and the relatively higher CPD NWs (indicated by a green circle) as Ga-polar NWs. Polarity characterisation were also obtained using the KOH chemical etching technique, which further supported the KPFM measurements.

The ability to control the polarity of III-V NWs is of interest, however, it is hard to pin-point the determining parameter for polarity control, as studies find conflicting results in the pursuit of polarisation-controlled NW growth [27]. A well-known effect is the interaction between the NW and substrate during the initial growth of NWs. For instance, III-V buffer layers has been found to promote the growth of NWs polarised in the same direction as the underlying layer [23].

2.1.3 Surface Energies

When a solid surface is created, the unfavourable energy cost of dangling bonds leads to increased energies at the surface compared to that of bulk. The most stable shape of a nanostructure is to some extent determined by a minimisation of the total surface energy, and thus, the crystalline planes with the lowest surface energies are most likely to be found on the surface [28, p. 521].

Through density functional theory (DFT) calculations, Zhang et al. [29] found the energy of the N-polar $(000\bar{1})$ -plane of WZ GaN to be $168.3\text{meV}/\text{\AA}^2$, and the Ga-polar (0001) -plane to be $198.2\text{meV}/\text{\AA}^2$. The a -planes showed a surface energy of $103.0\text{meV}/\text{\AA}^2$, and the m -planes a slightly lower surface energy of $96.9\text{meV}/\text{\AA}^2$.

The surface energies of WZ AlN was also calculated using DFT in a study by Holec and Mayrhofer [30], where it was found that the N-polar $(000\bar{1})$ -plane had a surface energy of $374\text{meV}/\text{\AA}^2$, the Al-polar (0001) -plane $355\text{meV}/\text{\AA}^2$, the m -planes $145\text{meV}/\text{\AA}^2$ and the a -planes $234\text{meV}/\text{\AA}^2$.

For both GaN and AlN the surface energies are lowest for m -planes, thus, the most energetically favourable structure of a NW is a c -plane top with m -planar sidewalls. Comparing the c -planes, the N-polar plane exhibits the lowest surface energy for GaN, and the Al-polar plane for AlN. Thus it could be expected, that GaN NWs would most likely be N-polar, while AlN NWs would be Al-polar. It should be noted, that in reality, the shape of a NW is not defined entirely by these energetic equilibrium shapes, but can be expected to be influenced greatly by adatom kinetics.

The surface energy is also affected by any strain present in the material. In a study by Ko et al. [31] the structure of N-polar GaN NWs with m -planar sidewalls was studied. Simulations based on DFT were carried out to estimate the surface energy for both compressively and tensily strained $(000\bar{1})$ - and $(1\bar{1}00)$ -planes in GaN. The results are shown in Fig. 2.4, where it can be seen that a compressive biaxial strain in the $(000\bar{1})$ -plane leads to an increase in the surface energy for the $(000\bar{1})$ -faceted NW tops, and a decrease in the surface energy of the $\{1\bar{1}00\}$ -faceted sidewalls. The opposite is the case when the strain is tensile, where the surface energy of the NW tops increases, and the surface energy of the sidewalls decreases. This shows, that a tensile strain promotes vertical growth and results in NWs with higher aspect ratios. It also shows that Si(111) is a good candidate for GaN NW growth, since the strain induced in the NW from the lattice mismatch at the interface is expected to be tensile, as will be discussed further in Sec. 2.2.

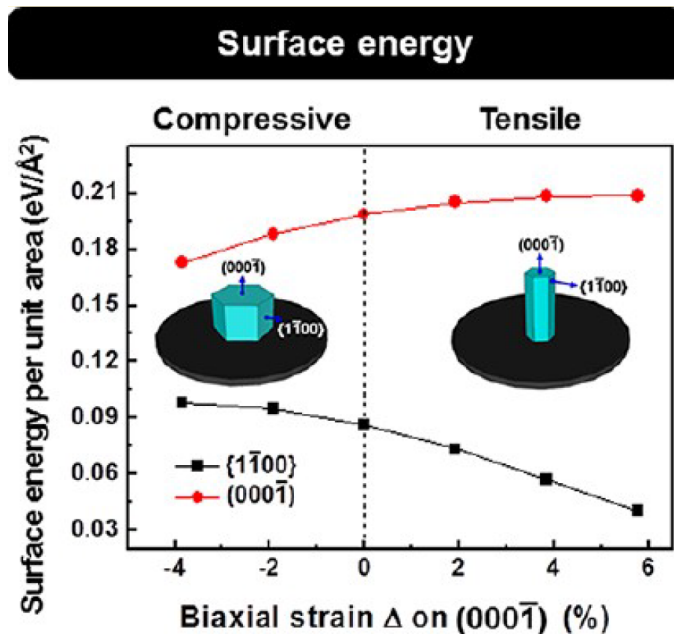


Figure 2.4 Surface energy of $(000\bar{1})$ - and $\{1\bar{1}00\}$ -planes as a function of biaxial strain on the $(000\bar{1})$ -plane for WZ GaN. Reprinted (adapted) with permission from [31]. Copyright 2012 American Chemical Society.

2.2 Microstructural Defects and Lattice Mismatch

Crystal structures may experience two main types of crystal defects: point defects related to single atoms such as vacancies, impurities and interstitials and line defects like dislocations concerning rows of atoms [32, p. 530], as illustrated in Fig. 2.5. Point defects are often associated with the temperature and lattice vibrations of the crystal, allowing for the probability of an atom to migrate from a lattice site leaving behind a vacancy, as shown in Fig. 2.5(a). A more intrusive defect are line defects such as dislocations, which may disrupt some of the electronic properties and crystal quality of semiconductors, reducing their overall performance [33]. Dislocations often extend through the entire crystal lattice. An edge dislocation is shown in Fig. 2.5(b).

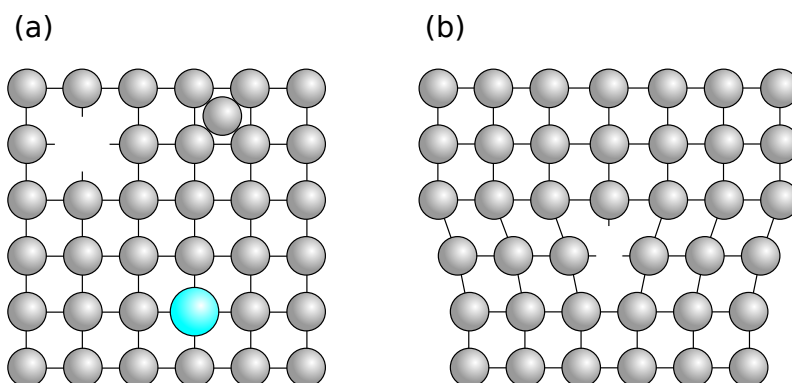


Figure 2.5 Illustration of commonly occurring defects. (a) Vacancy, impurity (blue atom) and interstitial point defect (atom in between lattice atoms). (b) Edge dislocation. Inspired by [32, p. 531].

Dislocation defects are created from mechanical strain in the lattice, which often occur when two materials with different lattice constant create a common interface. This strain is associated with the lattice mismatch between the substrate and layer, expressed by [34, p. 39]

$$\varepsilon = \frac{a_S - a_L}{a_S}. \quad (2.1)$$

Here, a_S and a_L refers to the unstrained lattice constant of the substrate and overlayer, respectively. This mismatch may induce strain which is either compressive or tensile, dependent on the sign of ε . If $\varepsilon > 0$ the strain is tensile, and if $\varepsilon < 0$ the strain is compressive as illustrated in Fig. 2.6(a) and (b), respectively. If the strain becomes too large, dislocations start to form in order to relax the strain.

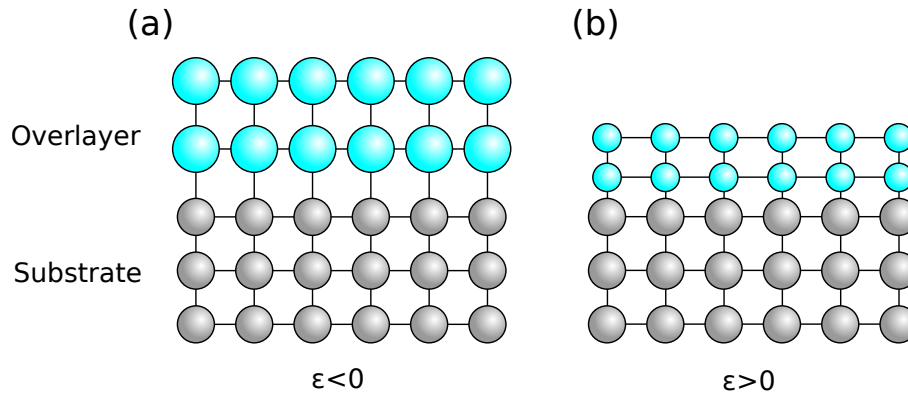


Figure 2.6 Overlayer and substrate with different lattice constants resulting overlayers with (a) compressive strain and (b) tensile strain. Inspired by [34, p. 39].

The large interface area between a substrate and a thin film is prone to dislocation formation as strain builds up. The substrate-material interface of NWs is vastly lower, which almost completely removes dislocations. For instance, NWs grown from GaN show little to no defects and strain [35]. However, stacking faults are often found in NWs. Stacking faults occur when the stacking sequences of the crystal is altered as illustrated in Fig. 2.7. Imagine a close packed hexagonal layer (A), with an identical layer (B) deposited on top which is turned 60° in order to touch the interspaces of the underlying lattice. The third layer may then be rotated back 60° in order to obtain the ABABAB WZ structure, or turned an additional 60° to create a (C) layer as found for zinc blende (ZB) structures. Disturbances to these layer sequences are the origin of these stacking faults [32, p. 572][36, p. 297].

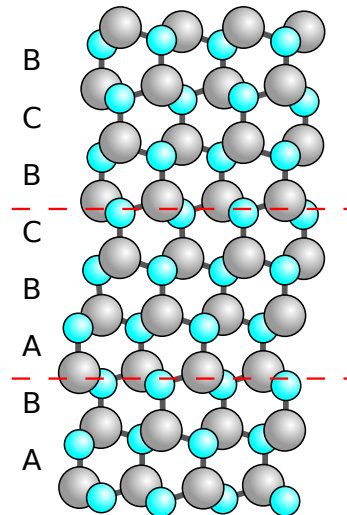


Figure 2.7 A common stacking fault arising from the disorder of stacking sequences of WZ.

As a reduction in strain is desirable, the use of Si(111) is instructive, as this orientation of Si shares the hexagonal symmetry of the WZ structured AlN and GaN [10, p. 17]. However, by using Eq. (2.1), the lattice mismatch between Si(111) and AlN is calculated to be 21.4% , and for GaN the mismatch is 18.4%, which is a very high value in both instances. Even though dislocations are not prevalent in NWs, it is still desirable to avoid them, as dislocations may disrupt carrier mobility and alter the piezoelectric response of a NW. As found by Beznasyuk et al. [37] a solution may be to reduce the lateral dimension of the NW, as this causes the mismatch strain to be relaxed at the sidewalls of the NW, reducing crystal defects.

Stacking faults resembling ZB GaN has been observed, along with dislocations forming in the interface between coalesced NWs [38]. Similarly, Meng et al. [39] studied the stacking faults and dislocations of AlN NWs, finding 26% out of 369 NWs to exhibit stacking faults and/or dislocations, as shown in Fig. 2.8.

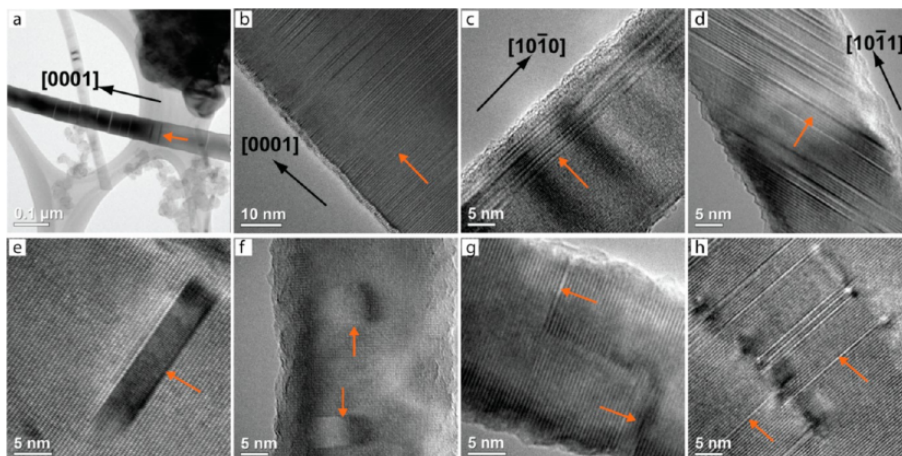


Figure 2.8 TEM images of stacking faults occurring in AlN grown in different directions: (a and b) [0001], (c) [10 $\bar{1}$ 0], (d) [10 $\bar{1}$ 1]. (e-h) shows stacking faults bounded by dislocations, where stacking fault are marked by an orange arrow. Reprinted with permission from [39]. Copyright 2009 American Chemical Society.

The stacking faults were found to occur in the $\{0001\}$ -planes in NWs grown in the $[0001]$, $[10\bar{1}0]$ and $[10\bar{1}1]$ directions, as shown in the high-resolution transmission electron microscopy (HRTEM) images in Fig. 2.8(a), (b), (c) and (d), respectively. Stacking faults were also found to disrupt the lattice into dislocations, which formed loops in order to terminate the dislocations (Fig. 2.8(e) and (f)), or by zig-zag dislocation which connect the stacking faults (Fig. 2.8 (g) and (h)).

FORMATION OF NANOSTRUCTURES

Growth of crystalline material is a complicated process, and the finished structure is influenced by the interplay between several different growth mechanics. The aim of this chapter is to provide an understanding of the general mechanics, which are involved in crystal growth, and their role in the growth of nanostructures. A special treatment is given to the nucleation and growth of NWs, with the intention of clarifying the particular mechanisms which facilitate growth in the vertical direction.

3.1 Crystal growth

The growth of crystalline structures are usually divided into two different regimes, dependent on the thermodynamics involved. For growth occurring in equilibrium, thermodynamic properties of the system may help describe growth. Far from equilibrium, the growth is better described by the kinetics of adatoms on the growth surface [34, p. 207].

3.1.1 Equilibrium Growth Modes

Solid-on-solid growth in thermodynamic equilibrium can be divided into three modes [40, p. 312], which are presented below. The evolution of growth corresponding to the three growth modes as the number of monolayers Θ is increased is illustrated in Fig. 3.1.

- Frank-Van der Merwe (FM) or layer-by-layer growth (Fig. 3.1 (a)), where a complete epitaxial layer is formed on the substrate before the next layer starts to grow, i.e. strictly two-dimensional growth takes place. This mode requires for the lattice mismatch to be very small ($|\varepsilon| < 1.5\%$).
- Stranski-Krastanov (SK) or layer-plus-island growth (Fig. 3.1 (b)) where the substrate is initially covered by a wetting layer, followed by the formation of three-dimensional islands as the strain increases. This growth mode is typically seen when $\varepsilon \geq 1.5\%$.
- Volmer-Weber (VW) or island growth (Fig. 3.1 (c)). In this case, three-dimensional islands nucleate and grow directly on the substrate surface. This happens if the lattice mismatch is sufficiently large for even the strain in a single monolayer to be thermodynamically unfavourable.

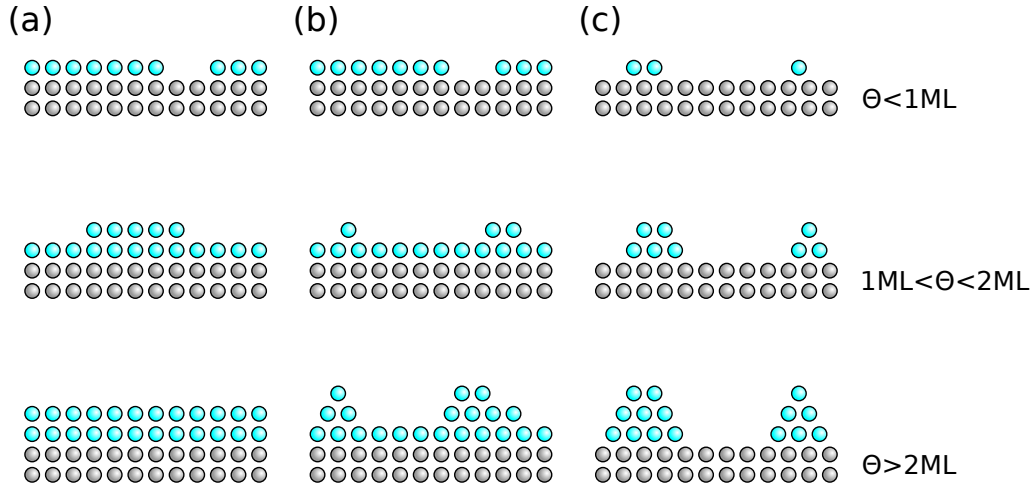


Figure 3.1 Evolution of a crystal corresponding to (a) FM-type, (b) SK-type and (c) VW-type growth, with Θ indicating the number of deposited monolayers. Inspired by [41].

While the growth modes described above are instructive, it should be noted that they apply only to solid crystalline materials grown under equilibrium conditions. The growth methods which are of interest for this thesis are away from equilibrium, where the morphology of the grown structures is mainly determined from factors related to kinetics.

3.1.2 Kinetics of Crystal Growth

The growth of a nanostructure away from equilibrium is governed by five processes which are critical for the resulting structures [28, p. 33]. These processes involve the adsorption of an atom on to the substrate surface, desorption from the surface into the vapour phase, surface diffusion, incorporation and 2D evaporation from a step, as illustrated in Fig. 3.2.

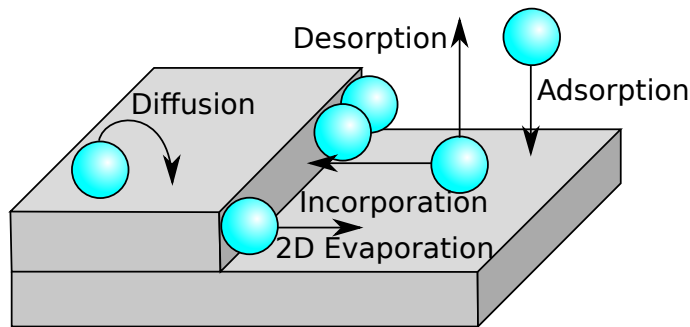


Figure 3.2 The five kinetic processes of an adatom on a surface: adsorption, desorption, surface diffusion, incorporation and 2D evaporation. Inspired by [28, p. 32].

The rate of these processes are highly dependent on the substrate temperature, as well as the potential landscape the adatoms are moving in. Each of these thermally activated kinetic processes, are governed by an activation energy, E_A , and may be expressed by [34, p. 269]

$$\tau(T) = \nu_0 e^{-\frac{E_A}{k_B T}}, \quad (3.1)$$

where $\tau(T)$ represents the mean adatom residence time on the surface, ν_0 is the attempt rate of one of the processes, which is proportional to the thermal oscillation frequency of the lattice [28, p. 33]. In other words, in order for the adatom to migrate on the surface, it has to overcome certain energy barriers for any kinetic process to occur.

These potential energies are summarised in Fig. 3.3, where the first case is the adsorption energy, E_a , which is governed by the Lennard-Jones potential between the adatom and the surface. Here, physisorption and chemisorption creates an activation barrier for the adatom to overcome, in order for the adatom to escape the surface [42]. The second case is diffusion of the adatom, where the energy barrier, E_A , is dependent on the lattice and temperature of the surface, as the adatom attempts to jump to neighbouring lattice sites. The third case involves the energy required to escape a kink or step, ΔE , also known as an Ehrlich-Schwoebel (ES) barrier [34, p. 281]. An adatom approaching a descending step experiences a repulsive force due to the ES barrier, resulting from the lack of nearest neighbours at the step edge. An adatom approaching an ascending step often leads to trapping of the adatom due to the step edge potential (ΔE), where the subsequent ES barrier further aids in trapping the adatom.

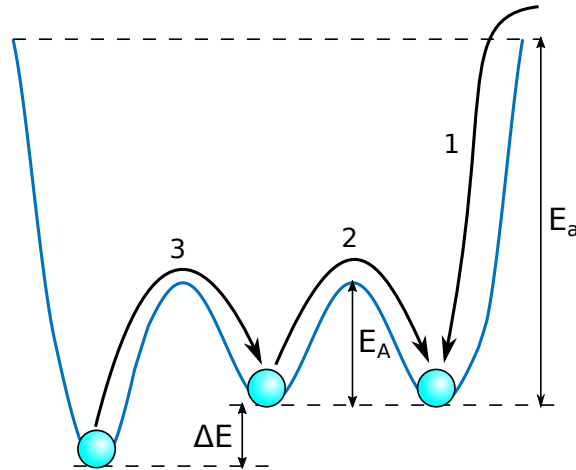


Figure 3.3 Kinetic energy barriers illustrating the (1) adsorption, (2) diffusion and (3) step edge barriers. Inspired by [28, p. 33].

3.1.3 Nucleation of Crystals

Nanostructures form on a substrate surface through nucleation of adatoms. Particles arrive at the surface with a flux F , where they are adsorbed. An adsorbed adatom diffuses across the surface, after which it either re-evaporates, collides with another adatom and starts nucleating, or becomes captured by an already existing cluster of particles. The mean time from the adatom's arrival at the surface until one of these events occurs is described by τ_a , τ_n and τ_c for re-evaporation, nucleation and capture, respectively.

The stability of a cluster depends on the number of particles, x , which it contains. More atoms are able to escape from small clusters, and thus, if x is not sufficiently large, the cluster might decay back into individual atoms. If a cluster reaches a critical size, i , it becomes stable,

and are no longer prone to decay. At this point, adatoms are more likely to become incorporated, and the cluster continues growing. The nucleation process of adatoms is illustrated in Fig. 3.4.

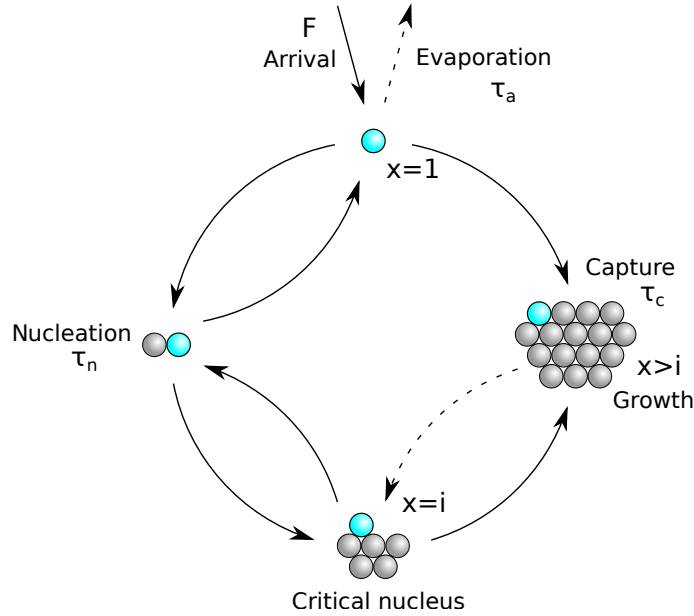


Figure 3.4 The nucleation processes of a diffusing adatom on a surface. Inspired by [34, p. 270].

It can reasonably be assumed, that only single mobile adatoms ($x = 1$) are able to participate in the growth process. The density of these adatoms (n_1) on a surface can be described by the rate equation [34, p. 272]

$$\frac{dn_1}{dt} = F(1 - Z) - \frac{n_1}{\tau_a} - \frac{n_1}{\tau_n} - \frac{n_1}{\tau_c}, \quad (3.2)$$

where Z is the fraction of the surface, which is already covered by stable clusters. The fact that τ_a , τ_n and τ_c are highly dependent on temperature allows for some control over the nucleation process, which is of interest when growing nanostructures such as NWs, where growth in the vertical direction is desired.

3.2 Nanowire Growth Mechanisms

In order to achieve the growth of NWs and suppress thin film formation, several methods may be utilised in order to promote a vertically preferred growth orientation. This section will describe some of these methods, and discuss their advantages and drawbacks.

3.2.1 Selective Area Growth

Prior to growth, templating techniques can be used to treat the substrate, such that NW formation is highly favoured. This is often referred to as selective area growth (SAG), and usually requires the addition of preliminary steps involving lithography to prepare the substrate. A common SAG

method involves the use of a mask, which is usually produced by depositing a layer of SiO_2 or SiN_x [43] on a substrate and patterning it using electron-beam lithography.

An example of NWs grown using SAG can be seen in Fig. 3.5, which shows a SEM image from a study by Choi et al. [44], where GaN NWs were deposited on a SiO_2 masked GaN film using MOCVD.

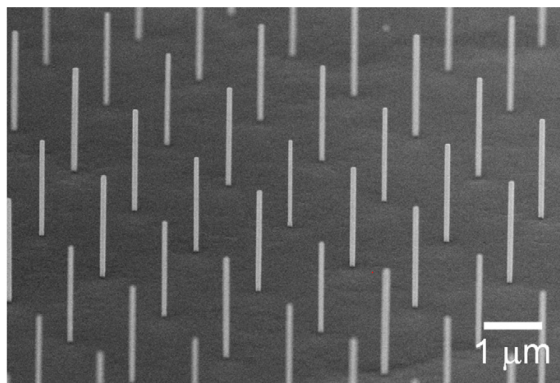


Figure 3.5 SEM image of GaN NWs grown using a SiO_2 mask. Reprinted from [44], with permission from Elsevier.

As shown in Fig. 3.5, Choi et al. succeeded in growing high quality narrow NWs with a diameter of only 50nm which have been neatly arranged in the desired pattern. The diameter of the NWs does not correspond directly to the hole size of the mask, which was set to 25nm, but the two were found to be strongly correlated, providing great control over the NW dimensions.

Generally, the ability to control both the arrangement and diameter of NWs is the greatest advantage of using SAG. However, the obvious drawback is that the extra steps which must be added prior to growth are often time consuming and costly.

3.2.2 Catalyst-Assisted Growth Mechanisms

One of the most common growth mechanisms of NWs is the vapour-liquid-solid (VLS) method [45]. It involves vapour reactants, which decompose and grow into a solid NW through the assistance of a liquid metal catalyst. Here, a liquid metal droplet is placed on a substrate surface, and the sample is then put into a vacuum chamber, where it is exposed to the vapour reactants. The adsorption energy is lower on the surface of the droplet compared to that of the surrounding substrate, and thus the droplet is preferred as a nucleation site. As adsorbed reactants are diffused into the droplet, the droplet eventually becomes supersaturated. At this point material starts to precipitate and crystallise at the solid-liquid interface. As the process continues, a solid NW emerges beneath the droplet, which remains on the top of the wire throughout [46, p. 3]. The lateral dimensions of the resulting NW can somewhat be controlled because its diameter is correlated to the size of the catalytic droplet. An illustration of the VLS process can be seen in Fig. 3.6.

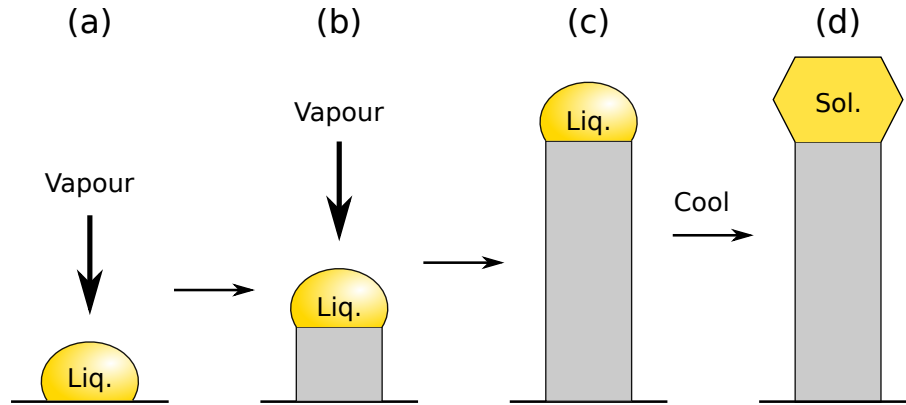


Figure 3.6 VLS growth mechanism of a NW. (a) A liquid catalyst sitting on the substrate surface is exposed to vapour reactants. (b) The catalyst collects the vapour reactants, which precipitates and solidifies at the catalyst-solid interface. (c) A NW is formed with the liquid catalyst present on the top. (d) As the NW is cooled the catalyst solidifies on its top. Inspired by [47].

Catalysts are typically made by coating a substrate in a thin film of the desired metal and annealing it. Thin films are only metastable because of their high interfacial energy, thus when heated they start transforming into more energetically favourable islands [48]. Often annealing is done above the melting point of the metal to ensure that the film completely dewets the substrate, but a phase transition into the liquid state is not generally required, as dewetting has also been observed for films kept in a solid state [49]. Generally a thicker film will result in larger catalysts [50]. The position and surface density of the catalysts can also be tuned by depositing droplets in a more controlled manner, e.g. by using dip-pen lithography [51]. The high level of control is a big advantage for VLS grown NWs, but some drawbacks are also present. After the sample is cooled, the catalytic droplets are solidified at the top of each NW, and thus an extra step to remove the unwanted material is necessary [9].

While VLS is one of the most widely used NW growth methods, there are still some controversies about the exact role of the catalytic particle. In the traditional VLS mechanism described above, the catalyst is necessary for any material to solidify at the substrate surface, and thus the possibility of growth anywhere else on the substrate is completely excluded. However, it can be argued that this model is rather simplistic, and that interactions between adatoms which are adsorbed onto the substrate and the catalyst are likely to contribute to the NW growth. In this scenario, the catalytic particle serves more generally as an agent for lowering the energy required for adatoms to nucleate at the liquid-solid interface [52]. This framework makes it possible to combine the VLS mechanism with kinetic models, which also treats the catalytic particle as a sink for diffusing adatoms, as done in a number of publications [53][54][55]. Several studies also find, that the catalytic nature is preserved even if the catalyst remains in a solid state throughout the growth [54][56][57]. In this case, the growth mechanism is referred to as vapour-solid-solid (VSS), but since the role of the catalyst is unchanged, the VLS and VSS mechanisms have more similarities than differences [52].

3.2.3 Catalyst-Free Growth Mechanisms

While the use of templates and catalyst particles provide great control over the growth process, the extra preliminary steps which must be taken, as well as the foreign materials which will inevitably be introduced into the system, are generally disadvantageous. To eliminate these issues, attempts have also been made on producing NWs directly on a substrate, without the deposition of any catalytic particles or masks prior to growth. This spontaneous growth of NWs requires specific growth conditions to be met, which will cause the deposited material to favour growth in the vertical direction as opposed to the lateral. To achieve this, it is often necessary to tune several parameters. The many influences from parameters which must be considered, as well as the different techniques which can be employed for growing NWs, makes it difficult to pinpoint a single mechanism, that adequately describes catalyst-free NW growth.

By combining several mechanisms, an attempt to create a model describing catalyst-free III-V NW growth has been created by Ristić et al. [58]. This particular model is based upon the growth of GaN NWs on Si(111) using MBE, but many of the growth mechanics described can be generalised to other III-nitrides, substrates, and growth techniques as well. The model is based on the nucleation processes described in Sec. 3.1.3, and divides NW formation into two stages: the nucleation stage and the growth stage, which are illustrated in Fig. 3.3(a) and (b), respectively.

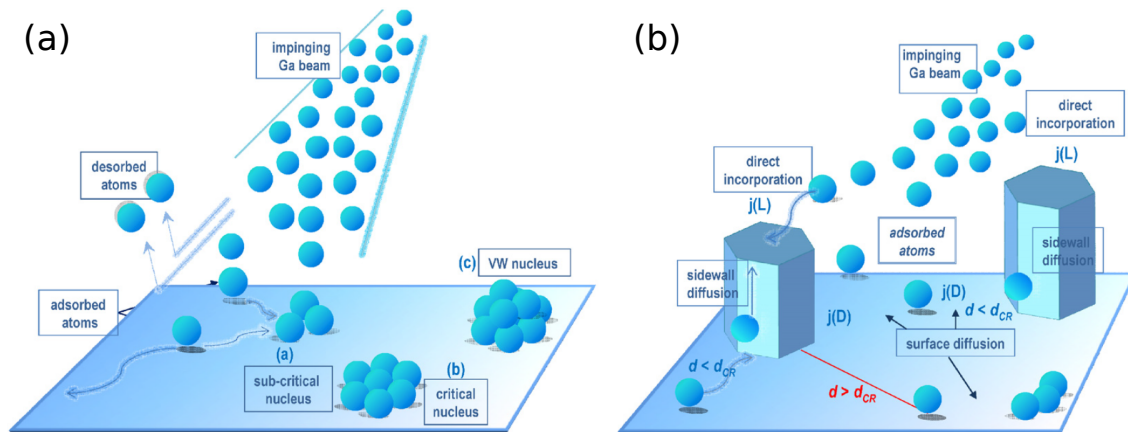


Figure 3.7 Diagram of the growth model developed by Ristić et al. illustrating (a) the nucleation stage and (b) the growth stage of GaN NWs. Reprinted from [58], with permission from Elsevier.

The nucleation stage is characterised by VW-type island growth caused by the lattice mismatch between Si(111) and GaN. The lattice mismatch is very large, and thus, no wetting layer can be expected. Ga adatoms are adsorbed onto the substrate and diffuse across its surface, where they might re-evaporate or collide with other Ga particles and begin nucleating. After the nucleus reaches its critical size such that $d > d_{cr}$, additional Ga adatoms which collide with it are incorporated and larger clusters start to form. These clusters form the foundation for further NW growth. The critical size increases as the temperature is raised, because atoms are more likely to desorb at higher temperatures, and thus it is expected that the NW diameter can to some extent be controlled by varying the temperature.

The cluster growth becomes saturated and the final island surface density is reached when the distance between the islands is around twice the diffusion length λ of the Ga adatoms, which is given by

$$\lambda = \sqrt{2}a \exp\left(\frac{E_a - E_A}{2k_B T}\right), \quad (3.3)$$

where a is the average jumping distance between adsorption sites. From Eq. (3.3) it can be seen that λ is controlled by varying the temperature, but also the V/III ratio plays an important role, because E_A for Ga adatoms is significantly increased if a large excess of N is present on the surface [59], which reduces λ .

After the nucleation process is complete, growth continues in the vertical direction. Here Ga atoms contribute to growth both in two ways: through direct incorporation of impinging atoms on the top of the clusters from described by the flux $j(L)$, and by diffusing on the substrate and along the sidewalls, where they arrive with a flux $j(D)$. Due to the typically low roughness of the GaN NW sidewalls, adsorption sites are few and far between, which causes the diffusion length to increase. On top of the NWs more adsorption sites are present, making it less likely for adatoms to diffuse away [58]. The model also points to the fact that the sticking coefficient for the c -planes of GaN is larger than for the m -plane, which means that impinging particles are more likely to stick to the NW top than to the sidewalls. The combination of all these effects are responsible for the highly anisotropic growth that results in the formation of NWs. The model predicts that some height variations between the NWs can be expected, because islands reach their stable size at different times during the nucleation stage. The diameter, however, is not expected to vary much as long as the temperature and V/III-ratio are kept constant.

While the above-presented model is instructive for understanding some of the basic growth mechanisms involved, when attempting to promote vertical growth in nanostructures, there are many possible growth effects which are not accounted for. Thus a more thorough study of the influences related to the applied deposition technique and specific growth conditions is necessary.

GROWTH OF NANOWIRES

Fabrication of NWs can generally be divided into two types: top-down and bottom-up. Using top-down methods, NWs are carved out from bulk material by removing redundant material using lithography-based techniques. This allows for manufacturing of very uniform NWs, which can be customised in the desired shape for a particular application. However, since the resolution of the lithographic techniques is limited, only NWs above a certain size (usually around 100nm in diameter) can be consistently grown. Another problem is that the NWs are prone to damage, as the redundant material is etched away, leaving amorphous areas on the NW surfaces [9].

Bottom-up methods allows for NW growth without wasting any material, and since bulk III-V materials can be costly, this approach is generally favourable for growth of these types of NWs. They also make it possible to grow thinner NWs of high quality. Bottom-up methods rely on assembly of particles into epitaxial NW structures. A number of different deposition techniques can be applied to fabricate NWs. This chapter will consist of a review on the literature concerning the most common bottom-up techniques for NW growth.

4.1 Molecular Beam Epitaxy-Grown Nanowires

A common method of growing NWs is molecular beam epitaxy (MBE). MBE deposition is carried out in a UHV chamber, where a substrate is subjected to pure gasses of the desired materials. Evaporation of solid or liquid materials such as Al and Ga are typically done using Knudsen crucibles[41, p. 38] as effusion cells, while N gas is supplied directly to the chamber. MBE is characterised by a very slow deposition rate, which allows for a controlled deposition of epitaxial layers on top of a crystalline substrate. Growth of III-V NWs is often heteroepitaxial, both because III-V bulk material substrates are not very cost-effective, but also because the strain induced by the lattice mismatch between substrate and deposited material results in VW growth, which help facilitate the growth of NWs rather than continuous film [9].

MBE generally provides for the most controlled growth, and NWs with a diameter as small as 20nm can be grown [60]. However, it is not preferable in industry, because of slow deposition rates and thereby reduced efficiency, and because MBE requires for the deposition chamber to be able to reach ultra high vacuum (UHV) at around 10^{-8} Pa. One upside to MBE is the possibility of achieving NWs without the use of catalytic particles [61].

4.1.1 Review of Nanowires Grown by Molecular Beam Epitaxy

In a study by Bertness et al. [62], GaN NWs were grown using catalyst-free MBE. Growth was carried out on Si(111) substrates with a thin AlN buffer at temperatures around 820°C and in a very N-rich environment. The morphology of the resulting NWs can be seen in Fig. 4.1, where a (a,c) top view and (b) side view is shown for two specimens. Bertness et al. identifies the NW sidewalls as m -planes and the growth to be in the c -axis direction, which is characterised by the hexagonally shaped cross-section clearly shown in Fig. 4.1(a) and (c).

The driving mechanism for NW growth is explained by the much higher sticking coefficient for the $\{0001\}$ -planes compared to the $\{1\bar{1}00\}$ -planes. Initially a seed crystal forms spontaneously on the substrate surface, and adatoms within a diffusion length are believed to incorporate onto its top eventually forming a NW. For this mechanism to work, the temperature must be kept high, such that the difference in sticking coefficients as well as the surface diffusion length are enhanced.

This is backed by the observation, that growth below 760°C led to the formation of more continuous films. It is also further supported by the fact that more densely grown NWs tends to widen as they grow, as shown in Fig. 4.1(b), because re-evaporated adatoms are more likely to collide with a neighbouring NW and get incorporated. The slow growth rate and high re-evaporation typical for MBE pushes growth closer to equilibrium than other growth methods, and thus the NW shape is expected to be more influenced by thermodynamics. This could explain why MBE-grown GaN NWs often exhibit clearly hexagonal cross-sections which are also observed in several other studies [63][64][65].

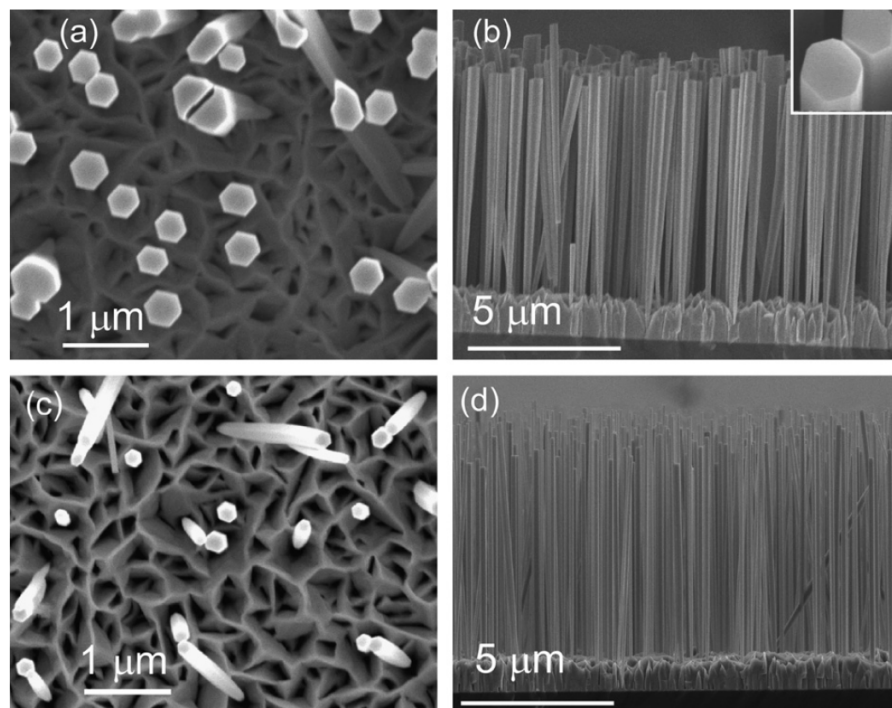


Figure 4.1 SEM images showing (a,c) top views and (b,d) side views of GaN NWs. Reprinted from [62], with permission from Elsevier.

A more detailed study on the effects of temperature on the morphology of MBE-grown GaN NWs was carried out by Mata et al [66]. NWs were grown in the range of 775-825°C with a temperature gradient, such that the temperature is highest in the middle of the sample and decreases towards the edge. SEM images of a sample can be seen in Fig. 4.2, showing measurements of areas grown with (a) lower temperature and (b,c) higher temperature. The surface density and NW diameters were observed to significantly decrease as the temperature was increased above 790°C, and no NWs formed above 805°C. Furthermore a much larger dispersion in the length of the NWs is found as the temperature is increased.

These observations are explained by the large Ga desorption which can be expected at higher temperatures. During the nucleation phase, clusters must reach a critical size before NW growth occurs. If Ga desorption is high, nucleation is less likely to happen, hence the time it takes for critical size to be reached will vary more between clusters, and as a consequence NWs will vary more in height. The increased diffusion length of the adatoms at high temperatures as well as shadowing effects causes the surface density of the NWs to decrease.

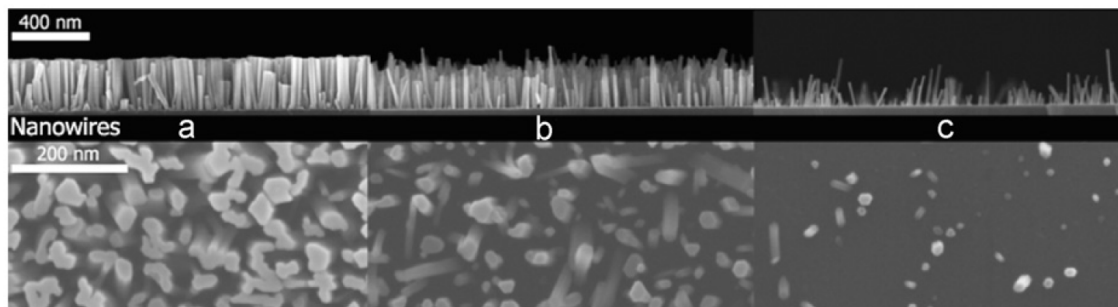


Figure 4.2 SEM images of GaN NWs grown at (a) a lower temperature and (b,c) higher temperatures. Reprinted from [66], with permission from Elsevier.

In a study by Landré et al. [67] catalyst-free AlN NWs were grown by MBE on Si(001) substrates covered by a thin layer of amorphous SiO₂. The substrate was chosen to insure a lack of epitaxial relationship with the intention of promoting VW-type growth. The AlN NWs were grown in the range of 900-950°C. It is argued that the growth temperature should be higher than what is typically used for GaN NW growth, because the diffusion of Al is lower than of Ga. The grown NWs are shown in Fig. 4.3. The NWs were found to be highly *c*-oriented and free of strain and dislocations. TEM images revealed that no wetting layer at the SiO₂-AlN interface was present, indicating that VW-type growth was achieved. However, the NWs are partially coalesced at the top, suggesting that even higher temperatures might be necessary to obtain free-standing NWs.

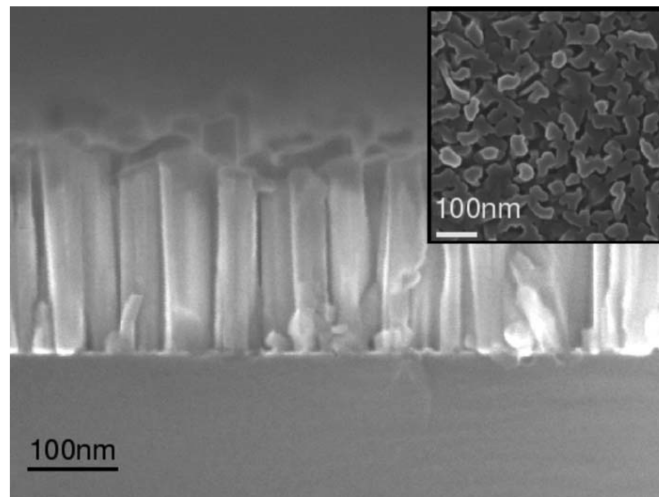


Figure 4.3 Cross-sectional SEM image of AlN NWs. The inset shows the top view. Reprinted from [67], with the permission of AIP Publishing.

The importance of keeping the atmosphere N-rich during deposition was studied by Ristić et al. [58]. SEM images of AlGaIn NWs grown on AlN buffered Si(111) can be seen in Fig. 4.4, where panel (a) shows NWs grown under conditions of higher N-excess than the case presented in panel (b). While both samples show that a film of wide columns form in the initial growth stages, it is clear that lowering the N-excess results in much wider and more coalesced columns. This is believed to be related to the increased diffusion of Ga adatoms on the substrate caused by the decreased amount of N. In both cases, NWs were still able to form on top of and between the columns.

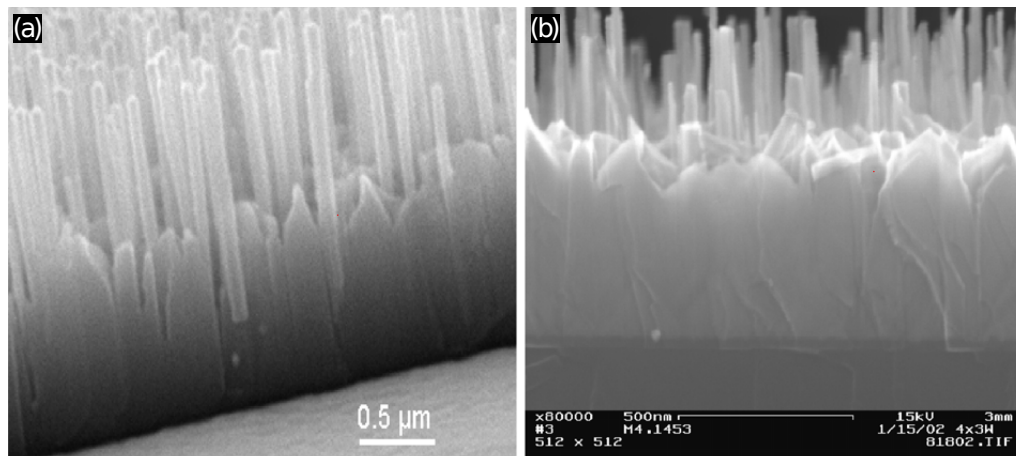


Figure 4.4 SEM images of AlGaIn NWs of AlN buffered Si(111) grown with (a) a lower V/III ratio (b) a higher V/III ratio. Reprinted from [58], with permission from Elsevier.

The importance of having a large lattice mismatch, which initialises a VW-type growth is also emphasised in the same study by Ristić et al. [58]. Here, GaN NWs deposited under the same conditions, were grown on both AlN buffered Si(111) and bare Si(111), as shown in Fig. 4.5(a) and (b), respectively. Since the AlN buffer layer reduces the lattice mismatch at the interface, the GaN initially forms wide columns with tendencies to coalesce. Between and on top of the

partially coalesced columns, thinner and more defined NW structures are able to form. However, when grown on bare Si(111), separate NWs were found from the beginning with no signs of any coalescence, emphasising the ability for a large lattice mismatch to promote vertical growth.

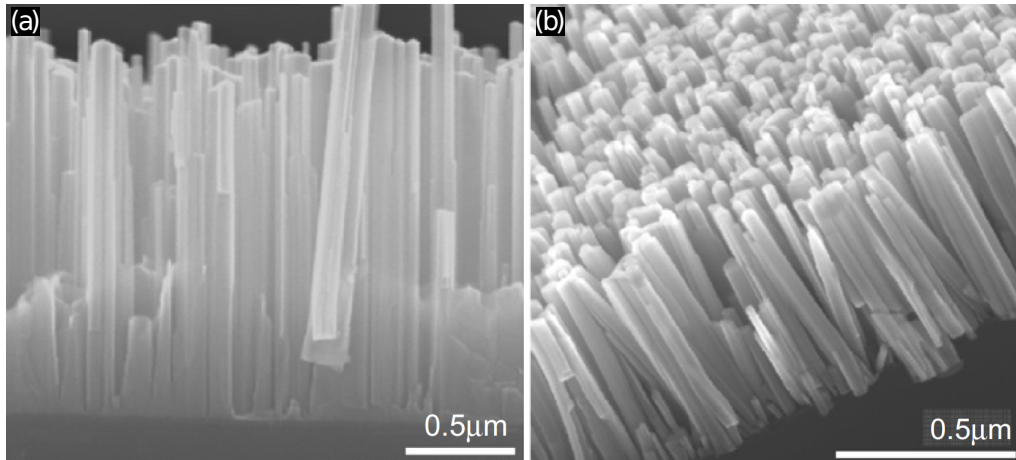


Figure 4.5 SEM images of GaN NWs grown on (a) AlN buffered Si(111) and (b) bare Si(111) substrates. Reprinted from [58], with permission from Elsevier.

A different approach was taken by Zhao et al. [68], who succeeded in growing dislocation-free AlN NWs using MBE. Growth was done on a Si substrate, which was pre-deposited with GaN NWs as illustrated in Fig. 4.6(a). The template was made by depositing a Ga layer that formed small droplets on the substrate which was kept at 790°C. Subsequently, N gas was introduced and GaN NWs began to nucleate. After nucleation the Ga supply was cut, the substrate temperature raised to 800°C and Al gas introduced, causing AlN NWs to grow on top of the GaN. Fig. 4.6 shows an illustration of a single NW, and a SEM image of the AlN/GaN NWs. The NWs presented in Fig. 4.6(b) are *c*-oriented, highly uniform and have diameters of around 50-60nm. These results might suggest that AlN NW growth can be achieved at lower temperatures if the substrate is prepared appropriately.

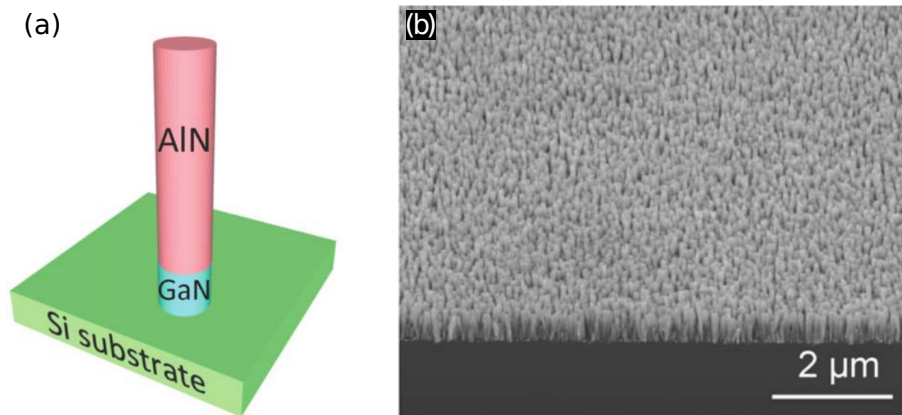


Figure 4.6 (a) an illustration of an AlN NW grown on a GaN NW template in a Si substrate. (b) A SEM image of this type of AlN/GaN NWs. Modified from open access source [68].

4.2 Metal Organic Chemical Vapour Deposited Nanowires

Contrary to MBE and other physical vapour deposition (PVD) techniques, which rely on direct vapour to solid phase transitions, MOCVD relies on chemical reactions occurring at the surface of a substrate to form solids [69, p. 689]. The MOCVD growth of III-V structures is based on supplying precursors containing the group-III and group-V reactants into a reactor. The reactor is configured in a way such that the gases are mixed and flow towards the heated substrate, in close vicinity to which pyrolysis causes release of III- and V-group elements leading to the formation of III-V compound on the substrate [70, p. 32][71]. Nowadays, MOCVD is one of the most widely used methods for III-V materials growth.

4.2.1 Review of Nanowires Grown by Metal Organic Chemical Vapour Deposition

The influence of temperature on the growth of MOCVD-grown GaN NW was studied by Köster [72]. Here, the NWs were grown on SiN_x covered sapphire substrates without the use of catalytic particles. It was found, that even a small decrease in temperature from 1000°C to 970°C had a large impact on the growth of the NWs. The surface density was found to be five times as high, the diameters of the NWs twice as small, the deposition rate increased, and the structural quality of the NWs greatly decreased. These effects can be explained by the decrease in diffusion length at lower temperatures. The lower diffusion length makes it more likely for adatoms to collide during the initial nucleation stage, which increases the surface density of clusters. The critical cluster size is reduced because of the lower probability for atoms to re-evaporate, causing the diameters of the grown NWs to be smaller. The deposition rate increases, because of a reduction in the pre-reactions which occurs in the gas phase, and the crystalline quality of the NWs is reduced, both because of the higher deposition rate and the decreased diffusion length, which prevents proper crystal formation. A sample produced, where the temperature was reduced from 1000°C to 800°C in steps of 50°C during growth can be seen in Fig. 4.7. Here, the large impact of reducing the temperature becomes apparent. The bottom parts of the structures where the growth temperature is 1000° are NW-like, with smooth sidewalls and few defects. As the temperature decreases, porous and highly defective structures begins to form.

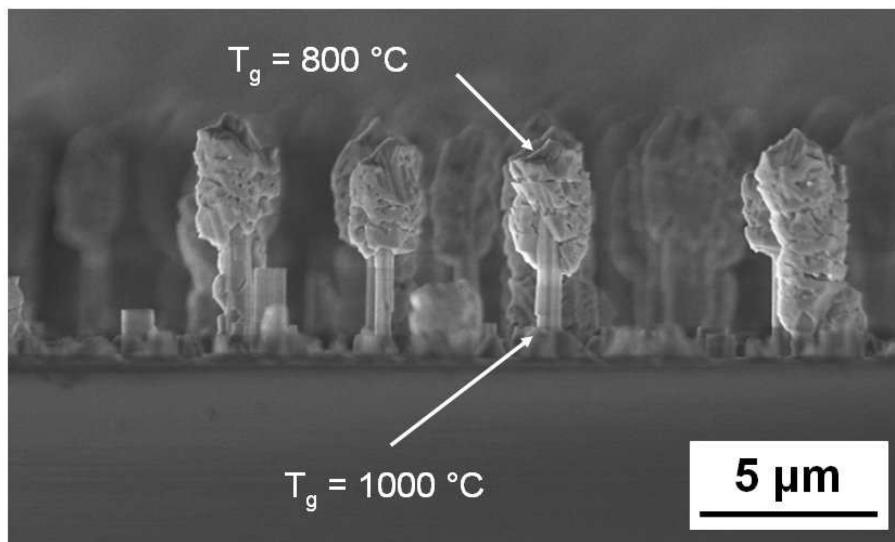


Figure 4.7 A SEM image showing GaN nanostructures grown with a step-wise reduction in temperature from 1000°C to 800°C. Reprinted from open access source [72].

The flow rates of the group-III and V precursors also have a pronounced effect on the NW morphology, as found by Kang et al. [73]. GaAs NWs by Au catalyst-assisted MOCVD were studied at different V/III ratios. They found increases in the TMGa flow to be more important in altering the morphology and quality of NWs, as opposed to the AsH₃ flow. When decreasing the V/III ratio, the increased Ga content resulted in increased axial growth and lower tendency for NWs to be tapered. Increased AsH₃ flows was found to have the opposite effect. The surplus and high diffusion length of Ga, combined with the growth occurring in a diffusion regime where substrate and NW sidewall diffusion is dominant, was believed to be the main contributors to the increased heights. MOCVD is usually performed with a large supply of the group-III precursor ($V/III > 1$), in order to promote the favoured vertical growth, as long as the temperature is high enough for sufficient pyrolyses of the precursors [74][75].

In a study by Ra et al. [76], the influence of the chamber pressure during MOCVD of GaN NWs on Si(111) substrate was investigated. Before deposition, the substrate was prepared with catalyst particles with diameters around 150-200nm consisting of an alloy of Au and Ga. The GaN NW growth was done at 950°C in an environment of N excess, where a different process pressure was chosen for each sample in the range of 200-700Torr. The resulting NWs can be seen in Fig 4.8. The study finds, that NWs begin to form at 200Torr, as shown in Fig. 4.8(a), but that they are short, irregular in shape and have a very low surface density. This can be explained by the large diffusion length expected at low pressures. As the pressure is increased, the NWs become longer and more closely spaced. However, at 300-400Torr as shown in Fig. 4.8(b) and (c), respectively, the NWs grow in random directions. The optimal process pressure is reached at 500-600Torr as shown in Fig. 4.8(d) and (e), where the NWs have a high surface density, are vertically ordered and have relatively uniform diameters in the range of 40-90nm. If the pressure is further increased to 700Torr as in Fig. 4.8(f), the shapes and sizes of the NWs become more irregular. For the sample

grown under the optimal process pressure of 600Torr, EDX measurements revealed, that no Au were present on top of NWs. This indicates that growth was not driven by the VLS mechanism, but rather the catalysts acted as preferred nucleation sites. The NW here were found by XRD to be primarily *c*-axis oriented, which is also supported by the clear hexagonal symmetry found for the NW tops.

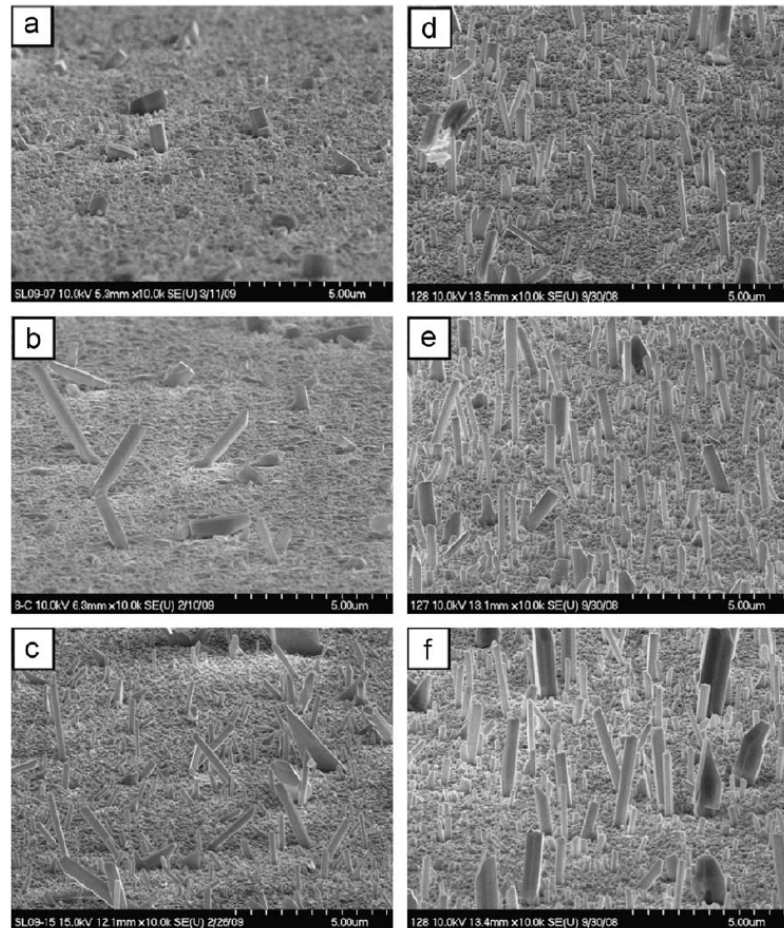


Figure 4.8 SEM images of GaN NWs grown under process pressures of (a) 200Torr, (b) 300Torr, (c) 400Torr, (d) 500Torr, (e) 600Torr and (f) 700Torr. Reprinted from [76], with permission from Elsevier.

The influence of the process pressure during MOCVD growth of GaN NWs was also studied by Ko et al. [31]. Here, catalyst-free growth was performed on Si(111) substrates. The growth rate V_G for the deposited material was described using the following formula:

$$V_G \propto \frac{1}{1/(k_0 p \exp(-E_A/k_B T)) + \sqrt{p}}, \quad (4.1)$$

where p is the pressure and k_0 a pre-exponential factor, which is determined such that $k_a - k_d = k_0 p \exp(-E_A/k_B T)$, where k_a and k_d are the rate of adsorption and desorption, respectively. To grow NWs, V_G should be high for $(000\bar{1})$ -planes, and low in the $\{1\bar{1}00\}$ -planes. From Eq. (4.1) it is clear to see that the impact on V_G of varying p depends heavily on the value of k_0 . If k_0 is very large, the second term in the denominator will dominate as p increases, leading to a $p^{-1/2}$

dependence and a decreasing V_G . Conversely, if k_0 is small, the first term will dominate, and V_G increases with p . The dependencies are visualised in Fig. 4.9. Ko et al. argue, that since NW growth is carried out with a low V/III molar ratio, the NH_3/H_2 ratio is low, and thus the desorption rate can be expected to be quite high. Thus k_0 is expected to have a low value, hence growth rate depends on pressure in accordance with the blue line in Fig. 4.9.

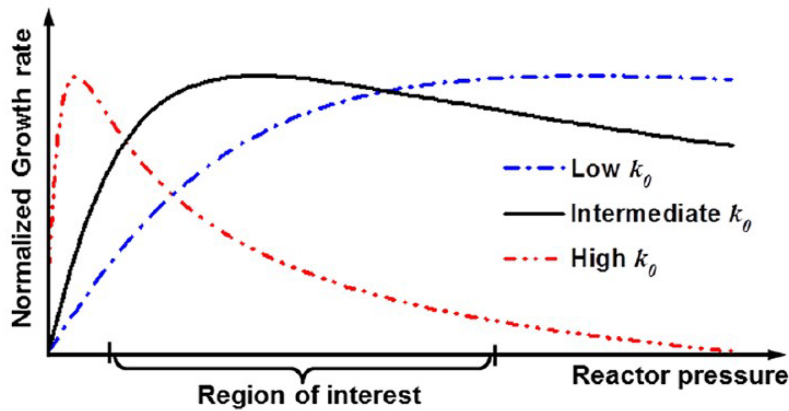


Figure 4.9 Growth rate as a function of pressure for different values of k_0 . Reprinted (adapted) with permission from [31]. Copyright 2012 American Chemical Society.

Experimentally, Ko et al. observed that the growth rate in the $[000\bar{1}]$ direction increases significantly as the pressure during growth is raised, while in the $[1\bar{1}00]$ direction it remains approximately the same, as shown in Fig. 4.10. This is explained by the large difference in the activation energy, which is around 0.93eV for the $(1\bar{1}00)$ -plane and 0.2eV for the $(000\bar{1})$ -plane. In the context of Eq. (4.1), larger activation energies will cause the growth rate to be less sensitive to changes in pressure. The found dependence is contrary to that typical for thin film growth, where increasing the of process pressure leads to a decrease in the growth rate.

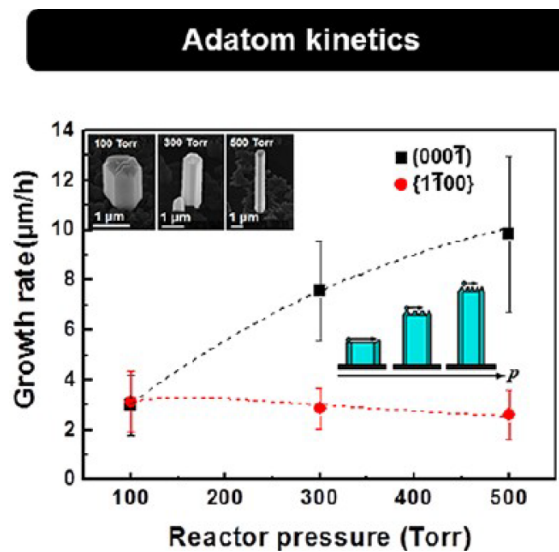


Figure 4.10 Growth rate of the $(000\bar{1})$ - and $(1\bar{1}00)$ -planes of GaN NWs at different pressures. The inset in the top left corner shows the morphology of GaN NWs grown with process pressures of 100Torr, 300Torr and 600Torr. Reprinted (adapted) with permission from [31]. Copyright 2012 American Chemical Society.

An attempt to grow AlN NWs using MOCVD was done by Cimalla et al. [77]. Growth was carried out on both sapphire and SiO₂ covered Si substrates at a working pressure of 75Torr and temperatures in the range of 900-1000°C. To induce VLS growth, the substrates were prepared with Au and Ni catalytic particles with diameters ranging from 20-1500nm. In Fig. 4.11 a SEM image of a sample is shown, grown under high N/Al conditions with a substrate temperature of 1000°C and a catalyst diameter of 100-200nm. Three-dimensional flower-like nanostructure is formed. The structure emerges due to lamella formation on top of the catalytic particle, which is attributed to the limited diffusion of Al adatoms. Increasing the temperature can enhance Al diffusion, but it also introduces other problems. High temperatures can stimulate the evaporation of catalysts, and cause large catalytic particles to become inhomogeneous, which might promote the growth of porous AlN. Smaller catalytic particles might evaporate completely, which was found for catalysts with diameters of 20nm. However, some NW-like structures were observed on catalysts with diameter around 100nm.

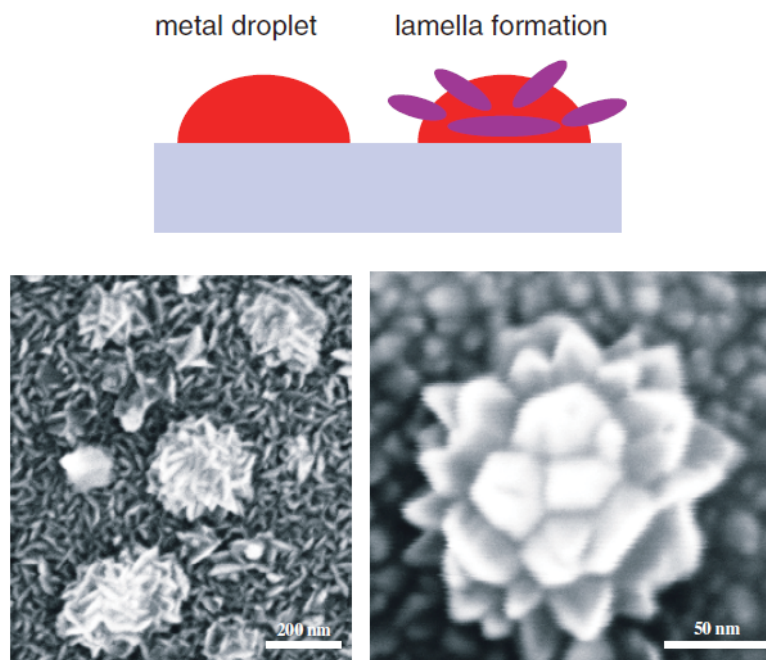


Figure 4.11 Schematic of lamella formation on a metal droplet. The SEM images show AlN structures with lamella formation giving them a flower-like appearance. Reprinted from [77], with permission from John Wiley and Sons.

4.3 Magnetron Sputter Deposited Nanowires

Magnetron sputtering has been found to be a fast and reliable method of depositing materials on a larger scale compared to MBE and MOCVD, which makes this technique of high industrial interest. Magnetron sputtering has several advantages compared to other methods: it is possible to grow a wide range of materials, where doping of the material is possible and large areas can be covered. As opposed to MOCVD, no toxic gasses have to be involved, and growth conditions can in some cases be held at room temperature. However, the process also provides less control, and keeping the quality and uniformity of the grown NWs high can be challenging.

Similar to MBE, a magnetron sputtering system consists of a UHV chamber, in which a substrate is placed. Particles are sputtered of a target by bombardment with gas ions (usually Ar), and adsorbed onto the substrate surface, thus forming a film or structures of the same material as the target. Additional reactive gas can also be supplied, enabling a reaction to with the target material in order to form a compound. In this case the process is called reactive magnetron sputtering. Often, N is used, allowing the growth of metal-nitrides.

4.3.1 Review of Nanowires Grown by Reactive Magnetron Sputtering

Selecting the proper temperature is crucial for vertical growth in magnetron sputtering, as made evident by Serban et al. [78], who have grown GaN NWs on Si(111) at different temperatures. SEM images showing their results can be seen in Fig. 4.12, which shows that at a substrate temperature of 800°C the GaN is a continuous films with no signs of NW formation. Raising the temperature to 900°C causes the GaN to grow in a columnar structure. Further increasing the temperature to 950°C results in separated wide NWs, while at 1000°C the NWs becomes longer, thinner and more separated. This emphasises that high temperatures are necessary for NW formation to occur. An inverse relationship between the NW length and diameter was found, as the temperature was changed. Gradually decreasing the temperature, yields lower and thicker NWs, converging towards a film structure.

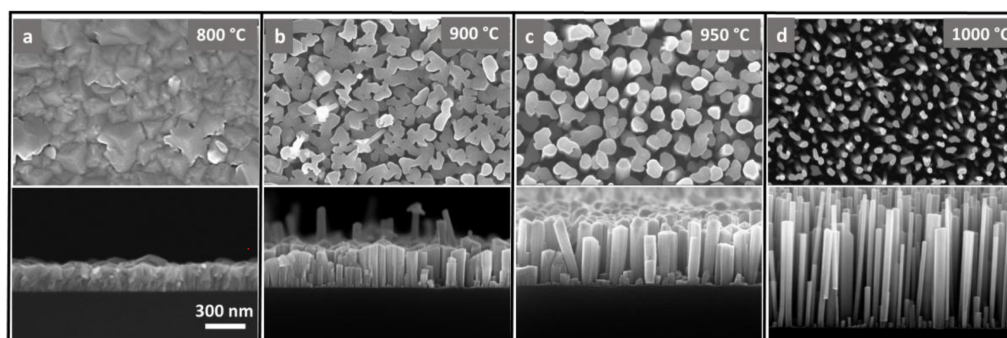


Figure 4.12 GaN NWs grown at different temperatures ranging from 800°C to 1000°C. Reprinted from open access source [78].

Catalyst-free GaN NWs grown by magnetron sputtering has been investigated by Junaid et al. [79], with a special focus on the effects of the ratio of N and Ar during deposition. NWs

were produced with different contents of N and Ar during deposition using Si(111) as a substrate. Temperature and pressure were kept constant at 1000°C and 0.67Pa, respectively. Cross-sectional and top view SEM images are shown in Fig. 4.13. Panels (a) and (b) show the morphology of NWs grown at an Ar/N ratio of 0.11, where a large aspect ratio has been achieved. A high Ga flux, along with the N-rich environment which restricts Ga adatom mobility, promotes the number of nucleation sites and consequently increases the surface density of NWs. Similar results for the surface density of NWs are found for Ar/N ratios of 0.43 and 1, as shown in Fig. 4.13 (c), (d) and (e), (f), respectively. However, lower aspect ratios indicate the formation of larger GaN nucleation sites, formed by the less N rich environment which increases Ga adatom mobility. The formation of an almost continuous GaN film at an aspect ratio of 4 is displayed in Fig. 4.13 (g) and (h). The low N content may transition the sputtering from poisoned to metallic, effectively increasing the Ga flux which results in a more N-deficient growth. Combined with the desorption of the Ga adatoms, this leads to a lower nucleation density with larger grains and lower growth rate.

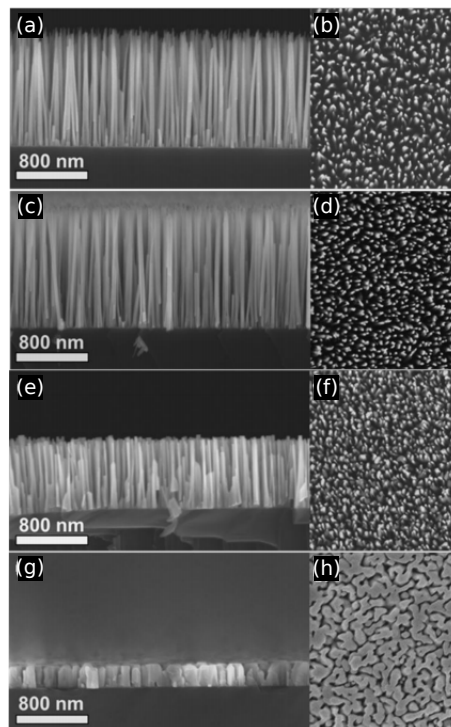


Figure 4.13 SEM images showing the cross section (left) and top view (right) of GaN NW samples grown at (a, b) Ar/N ratio of 0.11, (c, d) Ar/N ratio of 0.43, (e, f) Ar/N ratio of 1 and (g, h) Ar/N ratio of 4. Reprinted from open access source [79].

SAG may also be used when depositing by magnetron sputtering, as studied by Serban et al. [80]. They employed a TiN mask on a Si(001) substrate as the SAG template. It was found that increasing the temperatures from 875°C to 975°C improved the growth at the templated sites, as shown in Fig. 4.14. At 875°C NWs grow randomly and non-oriented, both inside and around the patterned mask. At 925°C growth at the template sites is achieved. At 940°C and 950°C the NWs show flat tops with more pronounced hexagonal structure. A small window between 965°C and 975°C was found, where the diffusion driven regime changes to desorption, as found by the reduced

NW length. Finally at a temperature of 985°C, the desorption regime dominates completely, where the patterned masks were filled with GaN, but further vertical growth was halted.

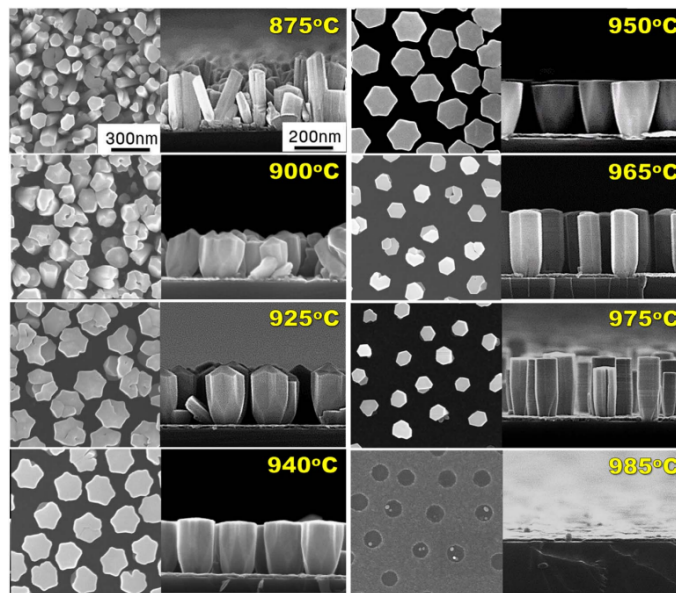


Figure 4.14 Top-view and cross-sectional SEM images of SAG of GaN by patterned Si substrates at different temperatures. Reprinted from open access source [80].

Modifying the substrate surface structure to function as a form of SAG was explored by Verbeno et al. [81], who grew self-assembled W NWs by magnetron sputtering. By utilising a miscut angle of a sapphire substrate in the $[1\bar{2}10]$ direction, small step edges are revealed. By placing the beam of the sputtered W at a specific angle (β) to be larger than the miscut angle (α) such that $\beta > \alpha$, as shown in Fig 4.15(a), particles are deposited at the step terraces and clusters appear at the step-edge due to shadowing effects. Further declination of the incoming beam angle, where $\beta \leq \alpha$, enhances the shadowing effects, which favours growth of NWs at the steps of the vicinal surface of the sapphire.

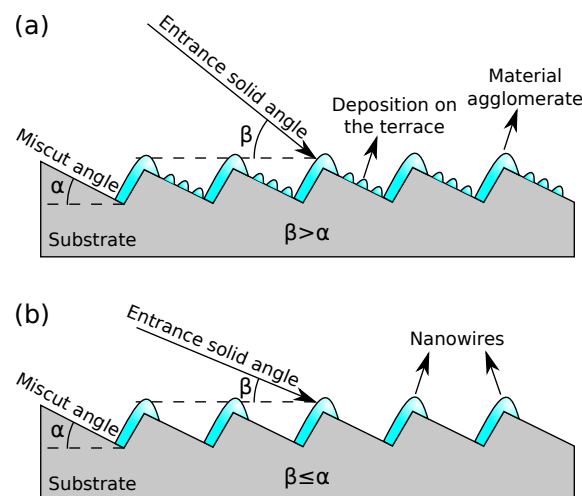


Figure 4.15 Schematic of the miscut angle NW growth model. (a) shows the deposition when the particle beam angle (β) is smaller than the miscut angle (α). (b) shows the formation of NWs when $\beta \leq \alpha$. Inspired by [81].

In general, the effects of shadowing may be employed in order to create different 3D structures. The method of glancing angle deposition (GLAD) has found to produce growth in the vertical direction and the formation of NWs, as studied by S. Mukherjee [82]. By comparing the structure zone model (SZM), which is further described in App. F, to deposition by GLAD at different angles $\beta \geq 80^\circ$ to the substrate, they suggested a growth model which encompasses GLAD. The left panel of Fig. 4.16 shows SEM images of some of these structures occurring at different homologous temperatures, corresponding to (a) rods, (b) columns, (c) protrusions and (d) equiaxed grains with whiskers.

The right panel of Fig. 4.16(f) illustrates these different structures, and compares them to the SZM of Fig. 4.16(e). Starting from the lowest homologous temperatures, θ , (right panel of Fig. 4.16(f)) where the limited surface diffusion due to low substrate temperatures, is believed to be the reason for the NWs (rods) occurring. At higher temperatures ($\theta = 0.24 \pm 0.2$), the columnar structures arise due to increased growth rates and enhanced shadowing. Increasing the temperature ($\theta \approx 0.35$) results in protrusions, as higher diffusion promotes lateral growth on the top of columns, which allows some of the columns to collect an over-proportionate amount of the incoming flux of particles, leaving the smaller columns unable to grow at the same rate. Above $\theta = 0.5$, the surface and bulk diffusion dominate the growth, which makes shadowing effects less predominant, resulting in grainy structures. However, a probability of a whisker to nucleate is found due to crystalline defects acting as a nucleation point, where further growth occurs due to strong shadowing effects.

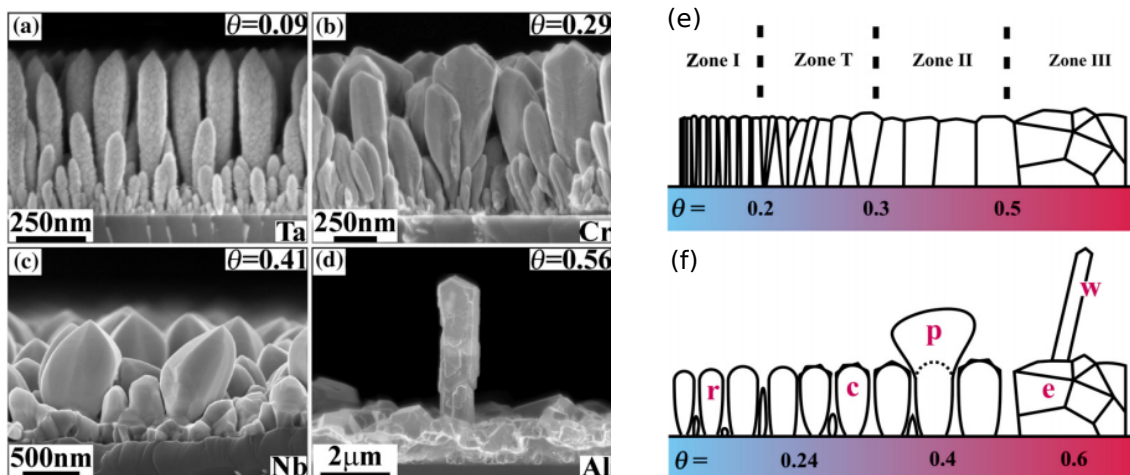


Figure 4.16 (Left) cross-sectional SEM images showing different GLAD'ed structures, (a) rods, (b) columns, (c) protrusions and (d) equiaxed grains with whiskers. (Right) homologous temperature dependent growth. (e) the original SZM (f) illustration of GLAD structures. Reprinted from [82], with permission from Elsevier

EXPERIMENTAL

The production of nanostructures require careful understanding of the technical aspects of the methods used, along with knowledge of the analysis techniques employed to study the structures. This thesis is concerned with the initial nucleation and nanostructures growth of AlN by reactive DC magnetron sputtering, and attempts of NW growth by MOCVD. Thus, a description of the sputtering and MOCVD machines used will be presented. The specifications on the analysis systems used will be given as well.

5.1 AlN Island Grown by DC Magnetron Sputtering

AlN structures grown by DC magnetron sputtering were carried out by a Flextura 200 system, produced by Polyteknik A/S. The Flextura 200 system consists of a load lock chamber (LLC), where the samples are mounted before being carried through the transfer chamber (TC) into the sputtering chamber (SC), where the sputter deposition takes place. A schematic setup of the system can be seen in Fig. 5.1.

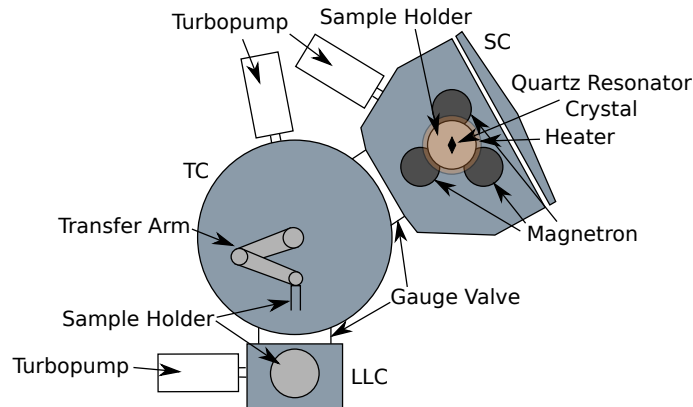


Figure 5.1 Schematic illustration of the different chambers and their constituent parts of the Flextura 200 system.

The SC is equipped with three magnetrons, and thus is capable of using three different targets for deposition. A sample holder is fixed facing down above the magnetrons. When initiating the deposition process the wafer can be heated and rotated, which is controlled by setting a predetermined temperature and RPM. Ar is used to form plasma in front of the target to sputter off material. To provide initial cleaning of the target and to ensure the deposition of material under well-controlled conditions, the wafer is shielded from the magnetrons by a shutter. The system is

equipped with an additional N gas line, in order to grow nitride compounds.

Full control of the different steps and parameters of the Flextura 200 system is possible: substrate temperature, magnetron ramp up time, target cleaning time, process pressure, supply of reactive gas and deposition time. During studies of AlN island nucleation, these parameters have been varied in order to further pursue the results obtained. The specific parameters for grown samples can be found in Tab. A.1, along with a more elaborate description of their relation to the sputtering process in App. A.

5.2 Nanowires Grown by MOCVD

In this study attempts for growing NWs by MOCVD have been made using an Emcore D180 system. The reaction chamber is a Swancore type shower head which is schematically shown in Fig. 5.2. As shown in Fig. 5.2(b) NH_3 is injected from the centre of the shower head and three independently controlled alkyl injection zones are positioned radially outward from the centre on each side. III/V source mixing occurs on the surface of the substrate as the group V species flows to the perimeter of the rotating sample holder. The sample holder is designed for wafers with diameters of 2in and can be rotated at up to 1500RPM, creating efficient III/V mixing conditions at the substrate surface. Any excess gas is pumped out through the exhaust from the bottom side. During deposition the system can be heated up by two filaments located beneath the sample holder to a maximum of 1100°C .

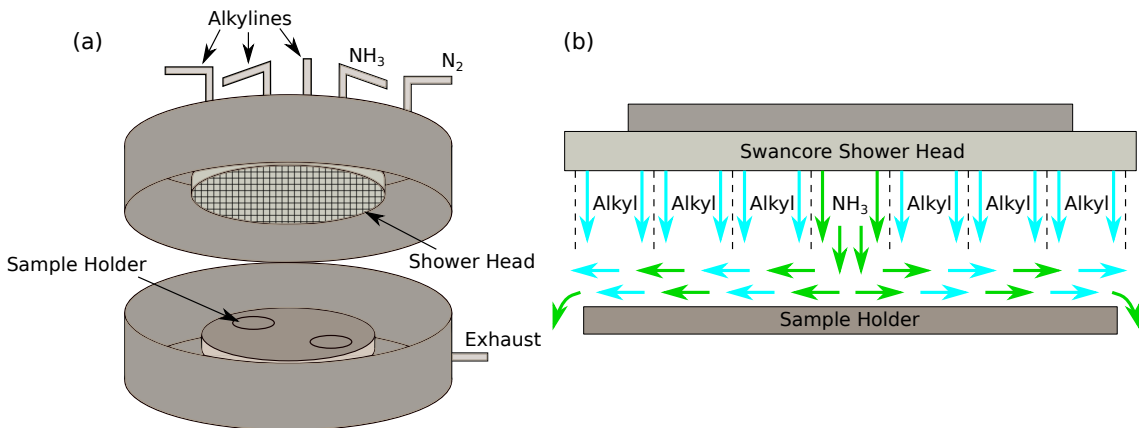


Figure 5.2 (a) Schematic of the MOCVD system and (b) working principle of the Swancore shower head including gas flow.

All attempts for NW growth have been conducted using a catalyst-assisted approach with Au nanoparticles. The Au nanoparticles have been produced by sputtering a thin film for 2min on a Si(111) substrate, followed by annealing at 800°C for 10min in vacuum. A SEM image of the Au nanoparticles, showing diameters up to 200nm, can be seen in Fig. 5.3.

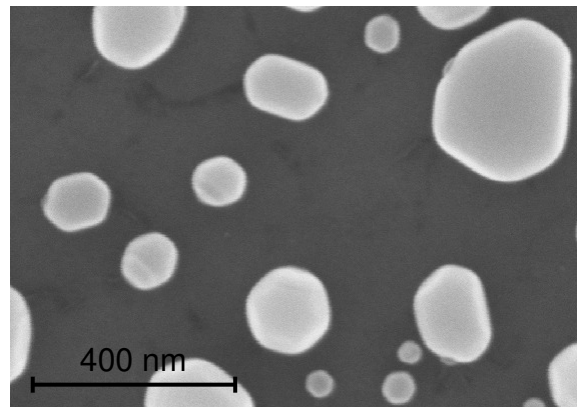


Figure 5.3 SEM image of Au nanoparticles acting as catalysts for all MOCVD grown AlN NWs.

The MOCVD system allows for control of temperature, rotation speed, process pressure, individual gas flows and deposition time. Parameters for all produced samples can be found in Tab. B.1 in App. B.

5.3 Nanowires by MBE

During the first few month of this project the MOCVD system was under maintenance. Therefore, four sample with MBE grown GaN NWs have been acquired from a group at the Institute of Physics at Polish Academy of Sciences lead by Professor Zbigniew R. Zytkeiwicz. 3in Si(111) wafers which were ex situ chemically etched to remove any oxide formation have been used for the NW growth. During growth the substrates have been heated to approximately 790° in the center, with a gradient resulting in temperature change of 30°C towards the edges. For the initial stages of growth, first N was supplied to the growth chamber before a N/Ga \approx 2 ratio was achieved. It is therefore found that an approximately 2nm thick film of Si_xN_y is grown on the surface prior to the NW formation [83]. Known specific deposition parameters can be found in Tab. C.1 in App. C.

5.4 Sample Preparation and Analysis

A cleaning process on all samples produced in this thesis has been carried out in order to minimise the presence of unwanted particles, which may interfere with the subsequent analysis. Here the wafer is placed in a beaker with acetone and submerged into an ultrasonic bath for 5min. The wafer is then thoroughly rinsed, first with acetone and then isopropanol, followed by an evaporation of the isopropanol using a N₂ gun.

After the samples has been produced, the wafer is either cut into 1 × 1cm peaces by a saw and cleaned again, or cracked by applying pressure with two scalpels positioned such that a particular plane is broken and then gently blown with N₂.

Samples presented in the following results and discussion chapter has been analysed by different techniques, which illuminate the morphological and compositional properties of the samples.

A Zeiss CrossBeam XB 1540 SEM has been used in order to give insight into the samples surface morphology, with resolution down to a few nanometers. An EDX microscope is connected to the SEM, increasing the utility of the device to include stoichiometry measurements and constituents of the near surface layers.

An Ntegra Aura nanolaboratory has been used for measuring topography by tapping mode AFM and surface potential distribution by KPFM. The measurements were carried out using either commercial Si cantilevers, whisker type Si cantilevers or Au-coated Si cantilevers. All AFM and KPFM measurements presented in the results has been corrected with a second degree polynomial.

RESULTS AND DISCUSSION

This chapter consists of a presentation of the results obtained through the experimental procedures clarified in Ch. 5, directly followed by an analysis and discussion. The samples will be referenced by their name indicated in Tab. A.1, B.1 and C.1 of the appendix, which provide the deposition parameters.

6.1 Nucleation of Ramified Islands

To investigate the growth mechanisms of AlN, a study on the early nucleation stages has been conducted. The emergence of ramified islands on the substrate surface was found, as shown in Fig. 6.1(a), where a SEM image of a typical sample surface can be seen. As these islands are of interest when describing the initial growth mechanics of AlN, this section will focus on the formation and growth of these islands. The exact morphology of the ramified islands are more readily seen from the zoom of an island shown in Fig. 6.1(b).

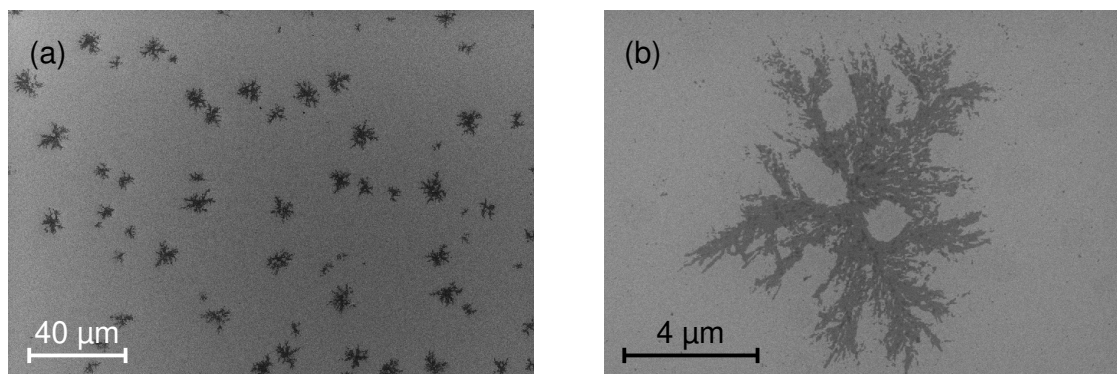


Figure 6.1 SEM images of (a) multiple ramified island formed across the Si(111) surface of sample Isl180 and (b) a zoom of an individual island.

6.1.1 Formation of Islands under AlN Magnetron Sputter Deposition

In this initial study, the evolution of islands depending on the deposition time was carried out. For this purpose, a series of samples were produced where the preliminary target cleaning process was kept identical, but the main deposition times varied in the range of 5-720s.

SEM images of the samples revealed, that the lateral dimensions and surface density of islands remains roughly the same for all samples. A rigorous study has been performed to estimate the exact island coverage percentage of each sample. Here, ten SEM images were taken at different

areas on the surface of each sample. In each image, islands were distinguished from the background based on the contrast difference. A comprehensive description of the image analysis is given in App. D, where an example of a coverage-analysed SEM image is given (Fig. D.1). The mean coverage found from the analyses along with the standard deviation for each sample are summarised in Tab. 6.1. The deposition time (in seconds) for each sample is indicated by the number following Isl in its sample name.

Table 6.1 Percentages of surface covered by ramified islands, calculated from contrast difference of SEM images, along with their standard deviations.

Sample Name	Island coverage [%]	Standard deviation [%]
Isl5	5.7	2.6
Isl15	5.5	0.9
Isl30	5.8	1.1
Isl60	5.5	2.3
Isl180	5.8	1.7
Isl360	5.1	1.1
Isl720	5.6	1.0

From Tab. 6.1, it is clear that island coverage is nearly identical for each sample. Taking the standard deviations into account, the small differences in coverage are insignificant, and island coverage can be regarded as independent on deposition time.

To investigate how the deposition time influences the structure of individual islands, AFM measurements were carried out to determine their heights. As a reference for these height measurements, the topography of a clean Si(111) wafer was measured using AFM, in order to assure that its surface was sufficiently smooth as to not obscure the topographic measurements of islands. The result from a $2 \times 2 \mu\text{m}$ measurement is shown in Fig. 6.2, which reveals a very smooth and flat surface with a root mean square (RMS) of 0.2nm.

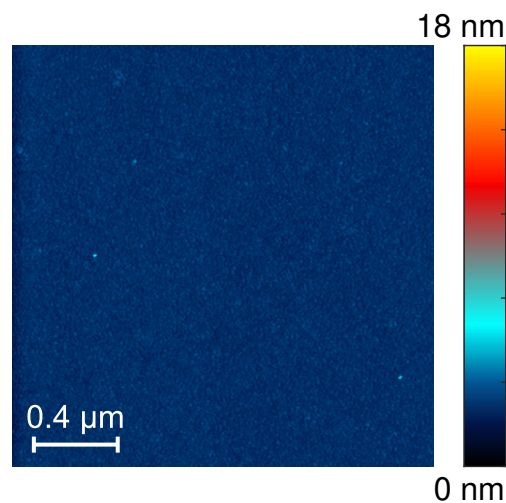


Figure 6.2 $2 \times 2 \mu\text{m}$ AFM image of Si(111) surface with native oxide layer with an RMS of 0.2nm.

AFM images of islands from the samples produced at deposition times of 60s (Isl60) and 720s

(Isl720) are shown in Fig. 6.3(a) and (b). The red lines across the island arms in (a) and (b) indicate the locations, where a height profile has been measured as presented below in Fig. 6.3(c) and (d), respectively.

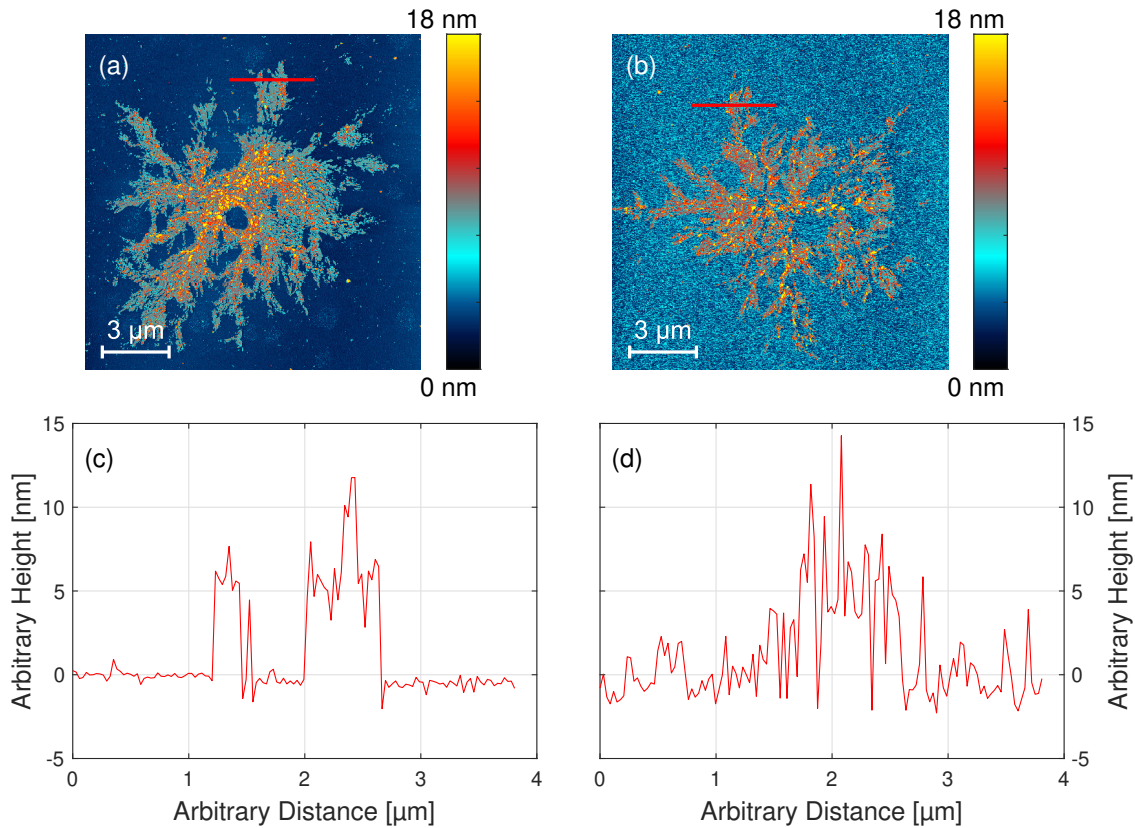


Figure 6.3 AlN ramified island on Si(111) substrate deposited for (a) 60s and (b) 720s. Height profiles shown in (c) and (d), are taken from the red lines indicated in (a) and (b), respectively.

The topography indicates distinct steps on both samples as seen from the sharp blue/orange/yellow contrast in Fig. 6.3(a) and (b). This is further emphasised in the height profiles. Specifically the height profile of Isl60 depicted in Fig. 6.3(c) shows the clear tendency for a step to be around 5nm. The tendency is less pronounced in the height profile for Isl720 in Fig. 6.3(d). However, this can be expected, as the surface roughness of the surroundings of the islands is significantly higher as can be seen in Fig. 6.3(b). The increased roughness is believed to stem from an AlN layer starting to form on the substrate between the ramified islands.

AFM measurements of the samples grown with other deposition times were found to be very similar to those presented in Fig. 6.3. These results led to the hypothesis that AlN grows in "magic" stable sizes of approximately 5nm in height.

To test this hypothesis, AFM measurements of ten different islands on each of the samples were carried out. Then, histograms were made to show the number of measured height values falling within a particular interval. A typical example of a height distribution based on a histogram for an AFM measurement of a single island can be seen in Fig. 6.4.

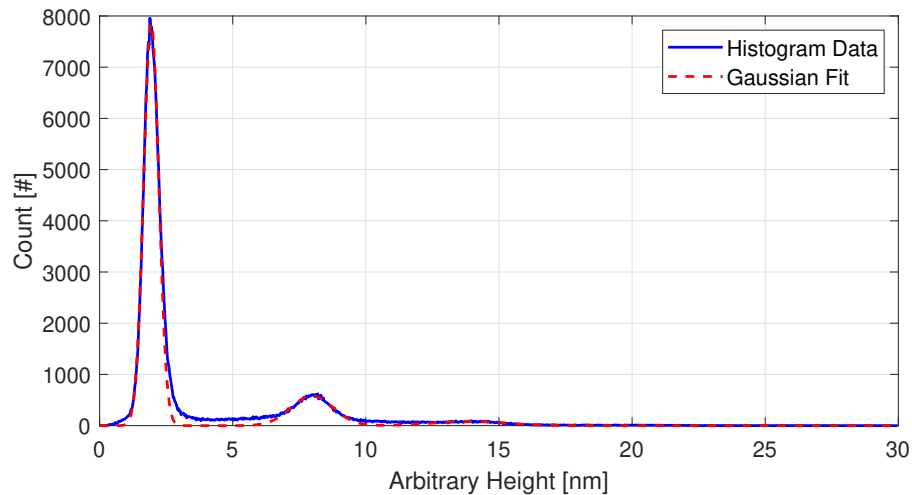


Figure 6.4 Histogram of the ramified island height obtained from Fig. 6.3(a), along with a fit constructed by the sum of three Gaussian functions, corresponding to the surrounding surface, first layer and second layer.

From Fig. 6.4 it is clear that the frequency of observed heights have peaks in two distinct regions. The first peak is related to heights measurements on the surrounding surface, the next peak to the height corresponding to the first layer. A very small peak around 13-14nm also seem to form which likely stem from the formation of a second layer. Gaussian fits where done on each peak to determine the layer heights on a sample, where the height of the first layer is determined as the difference between the means of the first and second fit, and the height of the second the difference between the means of the second and third. The grand mean for the first and second layer of the ten islands are given in Tab. 6.2, along with their standard deviations.

Table 6.2 Height measurements of first and second layer of the ramified islands, calculated as a mean value from ten measurements, along with their standard deviations.

Sample Name	First Layer [nm]	Second Layer [nm]	Standard Deviation of Layer 1 [nm]	Standard Deviation of Layer 2 [nm]
Isl5	4.7	5.3	0.3	0.2
Isl15	4.5	4.9	0.2	0.4
Isl30	5.4	5.5	0.3	0.2
Isl60	5.8	5.8	0.1	0.2
Isl180	5.3	5.4	0.1	0.2
Isl360	5.3	5.4	0.3	0.5
Isl720	4.4	5.3	0.6	0.2

From Tab. 6.2 it can be seen, that the layer heights are very similar for all samples, ranging from 4.4nm to 5.8nm for the first layer, and 4.9nm to 5.8nm for the second. This indicates that the magic heights are identical for both layers of the islands, and that they are independent of the deposition time.

While the samples are identical both in term of their surface coverage and magic heights, some differences become apparent, when comparing the surface structures of samples with different deposition times. This can be seen in Fig. 6.5, where samples with deposition times of (a) 15s and (b) 720s are shown.

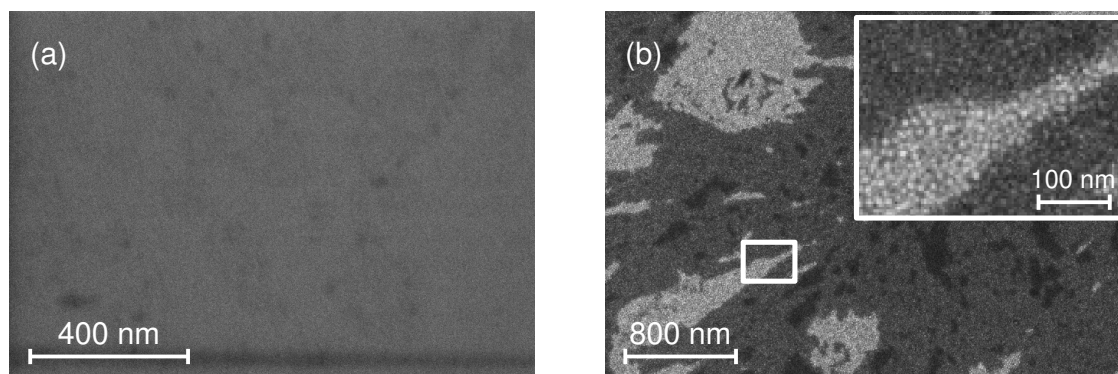


Figure 6.5 SEM image of (a) the surface morphology of the Isl15 sample away from any islands, and (b) the surface morphology both on top of and next to an island on the Isl720 sample, including an inset showing a zoom of the area indicated by the white rectangle.

As shown in Fig. 6.5(a), at a deposition time of 15s, the sample surface away from the island is smooth. In Fig. 6.5(b), it can be seen that after 720s of deposition, the surface is generally more textured both on top of the island and beside it. The inset shows a zoom of the surface, which reveals that the surface has a uniform grainy structure, which seems unaffected by whether it grows directly on top of an island or beside it. It is hypothesised, that after the islands are formed, a continuous grainy layer of AlN begins covering the entire sample. Thus, on-sputtered adatoms seemingly diffuse neither away nor towards the islands, but cover the entire sample independent of the underlying structure.

The exact elemental composition of both the islands and the continuous grainy layer shown in fig. 6.5(b) is still unknown. Through EDX measurements, the atomic percentages of Al and N were obtained on top of an island and in incremental steps beside the island, as shown in Fig. 6.6, for four samples with deposition times of 5s (Isl5), 15s (Isl15), 30s (Isl30) and 180s (Isl180). This allows both for determining the composition of the grainy layer, as well as investigating, if the islands differ from their surrounding material in composition. The results of EDX measurements are shown in Tab. 6.3, where the atomic percentages of Al and N can be seen. Subscripts indicate measurements taken on the island (I) and on the surface beside the island (S). Atomic percentages beside the islands are taken from the average of the measurements of the areas indicated by 2, 3, 4 and 5 as shown in Fig. 6.6.

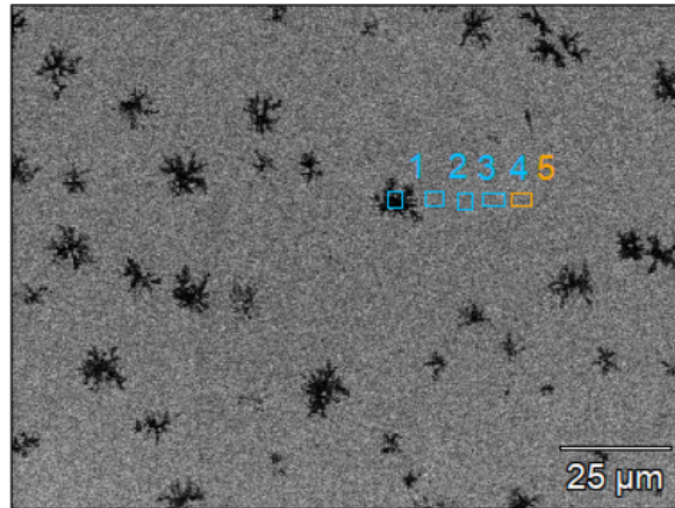


Figure 6.6 Example of a SEM image showing the placement of EDX measurements taken on and beside an island on sample Isl180.

Table 6.3 Mean results of EDX measurements showing the atomic percentage of Al and N on four samples on an island (subscript I) and on the surrounding surface (subscript S).

Sample	Atomic Percentage of Al [%]	Atomic Percentage of N [%]
Isl5 _I	0	0
Isl5 _S	0	0
Isl15 _I	1	1
Isl15 _S	1	1
Isl30 _I	2	4
Isl30 _S	2	4
Isl180 _I	10	11
Isl180 _S	12	12

The increasing amounts of both Al and N which is detected beside the islands suggest, that the continuous grainy layer observed at increased deposition times (see Fig. 6.5(b)) does indeed consist of AlN.

On each sample, no significant difference in the atomic percentages of either Al or N were found between islands and the surrounding material. Hence, it cannot be concluded, that islands differ in composition from their surroundings. However, the signal from both Al and N was too weak to be detected at a deposition time of 5s. Thus, it is likely that the amount of material, which constitutes the island is simply too low to be measured. Hence, the signal is dominated by the continuous AlN layer, and the composition of the islands remain unknown.

Note, that while the atomic percentage of N is higher than that of Al, it is not an indicator of non-stoichiometric AlN, but is a known effect when measuring lighter elements such as N.

6.1.2 Formation of Islands during Preliminary Target Cleaning

The fact that islands appeared already at a deposition time of 5s, and that they were essentially unchanged for increased deposition times led to the hypothesis, that islands form before the main deposition process. As described in App. A, prior to deposition, several steps are performed in the

Flextura 200 system during the preliminary target cleaning. During the target cleaning process, the path between target and sample is blocked by a shutter. However, small amounts of sputtered material might be able to circumvent the shutter and reach the substrate. To investigate whether the island formation was related to this, a series of five samples were produced where only the target cleaning process was performed and the shutter never removed.

Three samples were made to determine if the islands stem from the Al sputtered during target cleaning. Here, the ramp up time was kept at 20s (identical to that of the first series of samples), and the target cleaning time was set to 20s (IslAl), 40s (IslAl40) or 160s (IslAl160). No N was supplied at any point during this procedure.

An additional two samples were made to test the influence of the presence of N during target cleaning. For one sample (IslAlN) the ramp up time was set to 10s, then N was introduced, such that target cleaning was done in an environment of N for 20s. For the other sample (IslAlNOnly), N was supplied immediately to ensure that N was present before any sputtering could occur. Then target cleaning was carried out for 50s in the environment of N.

On all samples, ramified islands were found. Thus, islands are formed before the main deposition process, hence they are a product of the preliminary target cleaning process. Since islands formed even on samples, where no N was supplied at any point in the process, the islands likely consist of pure Al. Fig. 6.7 shows SEM images revealing the microstructure of island arms on a samples, where target cleaning was carried out (a) under pure Al conditions (IslAl40) and (b) in an environment of N (IslAlN).

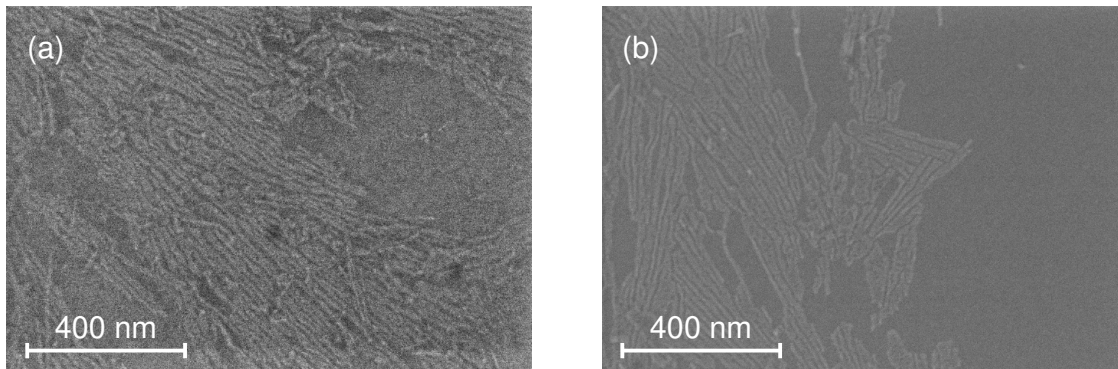


Figure 6.7 SEM image of cluster-chains forming on ramified islands on (a) the IslAl40 sample and (b) the IslAlN sample.

In Fig. 6.7 it can be seen than the structure of the island arms in both (a) and (b) consist of what are believed to be thin chains of clusters. The similarity of the structures for both samples indicate, that most probably the presence of N during target cleaning does not have any notable impact on the initial growth mechanisms of the islands. The microstructural formation of these cluster-chains, may be due to local preferred incorporation at step edges of the Si(111) surface, which fits well with Al cluster-chains measured by Kushvaha et al [84], as shown in Fig. E.1 of App. E. In their study it was found that increased deposition time led to preferential growth in the lateral directions, as opposed to increasing the height of the cluster-chains, and preferred

attachment to the sides of cluster-chains led to aggregation into a larger island.

An apparent difference in the surface coverage was observed, when the target cleaning in an N-depleted environment was extended from 20s to 40s, as can be seen in the SEM images shown in Fig. 6.8(a) and (b), respectively.

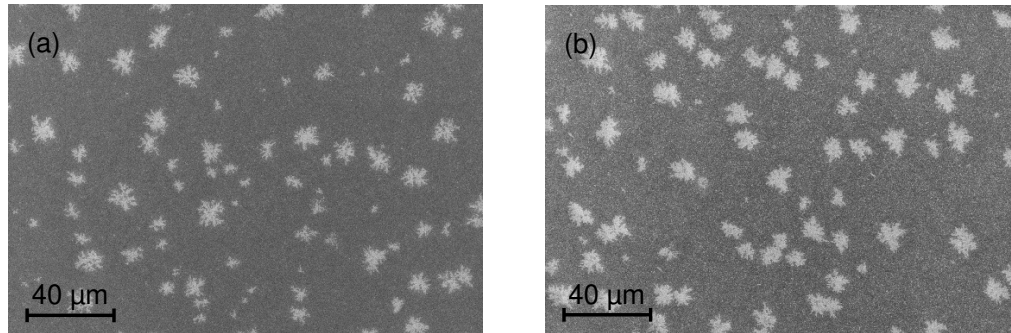


Figure 6.8 SEM image of (a) IslAl and (b) IslAl40 showing the coverage of ramified island on the Si(111) substrate surface after Al target cleaning (where the shutter shields the sample) for 20s and 40s, respectively.

While the number of islands roughly remains the same for both samples shown in Fig. 6.8, the lateral dimensions of the islands seems to have increased.

Analysis of island coverage from SEM images was done on the samples. Results are summarised in Tab. 6.4.

Table 6.4 Percentage surface covered by ramified islands calculated by contrast difference from SEM images. Results are based on the mean value of ten coverage analysed SEM images.

	Island coverage [%]	Standard deviation [%]
IslAl	5.6	0.7
IslAl40	14.4	2.0
IslAl160	13.6	1.1
IslAlN	3.5	4.9
IslAlNOnly	7.8	0.7

The surface coverage for the samples presented in Tab. 6.4 varies significantly, contrary to what was found for the surface coverage of the samples presented in Tab. 6.1, which were all similar. This strongly suggest, that island formation is not related to the main deposition process, but depends only on the conditions of the preliminary target cleaning process. It is worth noting, that IslAl exhibits a surface coverage of 5.6%, which is similar to those presented in Tab. 6.1. In the case of these samples, target cleaning with pure Al has been carried out for the same amount of time (20s), which suggest, that islands generally consist of pure Al.

The increase in the lateral dimensions of the islands as the target cleaning time is increased from 20s (IslAl) to 40s (IslAl40) causes the surface coverage to increase significantly from 5.6% to 14.4%. However, increasing the target cleaning time to 160s (IslAl160) did not lead to any further island growth, as seen by the island coverage percentage of 13.6%. The surface coverage was expected to steadily increase with target cleaning time, as step edges of the islands would facilitate

the incorporation of additional adatoms. The islands would eventually aggregate into a continuous layer, as also found elsewhere [85]. However, in this case the growth follows the multilayer growth mode, which leads to the formation of multilayered islands [86, p. 321]. It is possible, that at some point during the target cleaning process, impinging Al adatoms begin to nucleate into smaller clusters during their random walk on the substrate, instead of incorporating into existing islands. It is well-known that the activation energy of clusters are higher than single adatoms [87], which reduces the diffusion lengths, and inhibits the further growth of islands. A roughening caused by these clusters may limit the diffusion length of single adatoms on the substrate surface further.

For the samples, where the target cleaning was carried out in presence of N (IslAlN and IslAlNOnly), the island surface coverage does not reach 14%. It is likely that this observed decrease in the growth rate of the islands is a consequence of target poisoning, which can greatly decrease the sputtering yield, and thus lead to slower growth. It is also possible, that the presence of N on the surface reduces the diffusion length of adatoms. This effect has been found for Ga adatoms, where large amounts of N present of the surface caused a significant increase in E_A , resulting in a reduced diffusion length [59]. Thus, the island surface coverage in presence of N reaches only 7.8% as can be seen in Tab. 6.4 for IslAlNOnly.

AFM measurements has been carried out to determine, if the changes in the preliminary target cleaning process influences the tendency for islands to form in magic heights. The results are shown in Tab. 6.5.

Table 6.5 Height measured of first and second layer of ramified islands. Results obtained for samples IslAl and IslAlN are found from the mean value of two measurements, and IslAl40 from ten measurements.

	First Layer [nm]	Second Layer [nm]	Std 1 [nm]	Std 2[nm]
IslAl	4.8	5.2	0.5	0.7
IslAl40	5.6	6.0	0.3	0.1
IslAlN	5.4	5.2	0.1	0.8

As can be seen in Tab. 6.5, AFM measurements reveal that the islands still grow in layers of magic heights similar to those presented in Tab. 6.2. It should be noted that for IslAl and IslAlN, only two islands were measured, and thus these height values are less statistically reliable.

The CPD of a material, gives insight into its electronic and compositional states. The measured CPD values represent the difference between the work function of the local sample surface and the cantilever tip coating (Au in this case). As different materials have dissimilar work functions, the measured CPD of different materials should yield distinguishable results. Thus, if the islands grown in an environment of N consist of AlN, they should exhibit a different CPD compared to that of a pure Al island. Hence, KPFM measurements were carried out on IslAl40 as shown in Fig. 6.9, and on IslAlN as shown in Fig. 6.10, both with the corresponding (a) topography and (b) CPD map. Height and CPD profiles made from the red lines in (a) and (b), are shown in (c) and (d) in both cases, respectively.

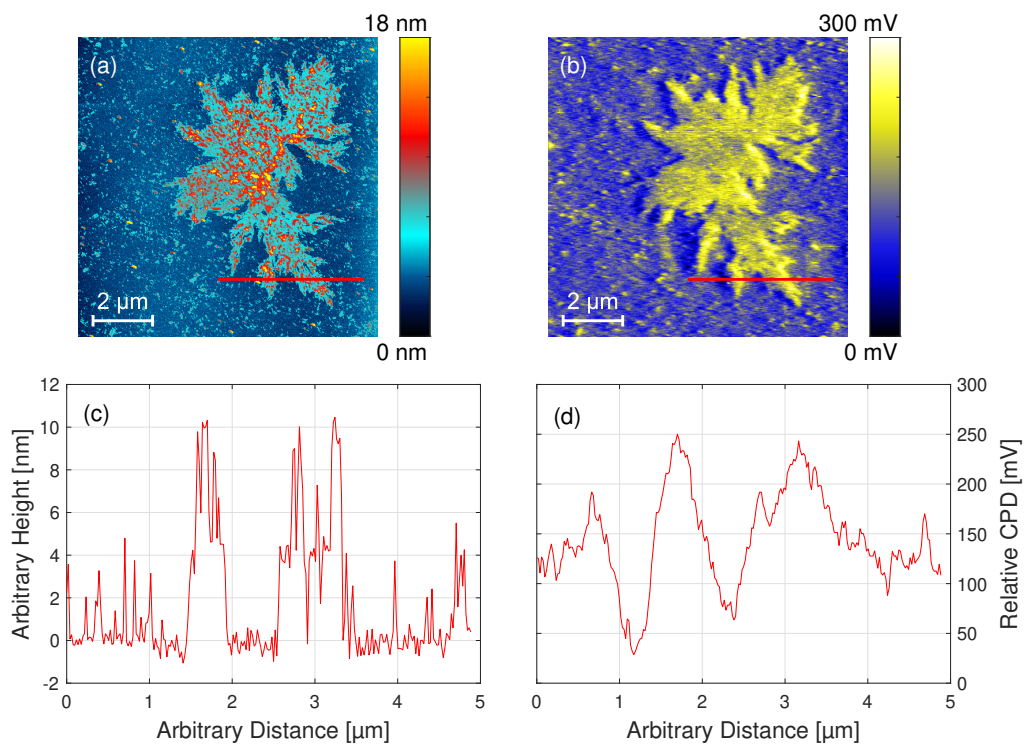


Figure 6.9 AFM measurement of a ramified island on sample IslA140 (a) topography and (b) the corresponding CPD map. Height and CPD profiles in (c) and (d), are taken from the red lines indicated in (a) and (b), respectively.

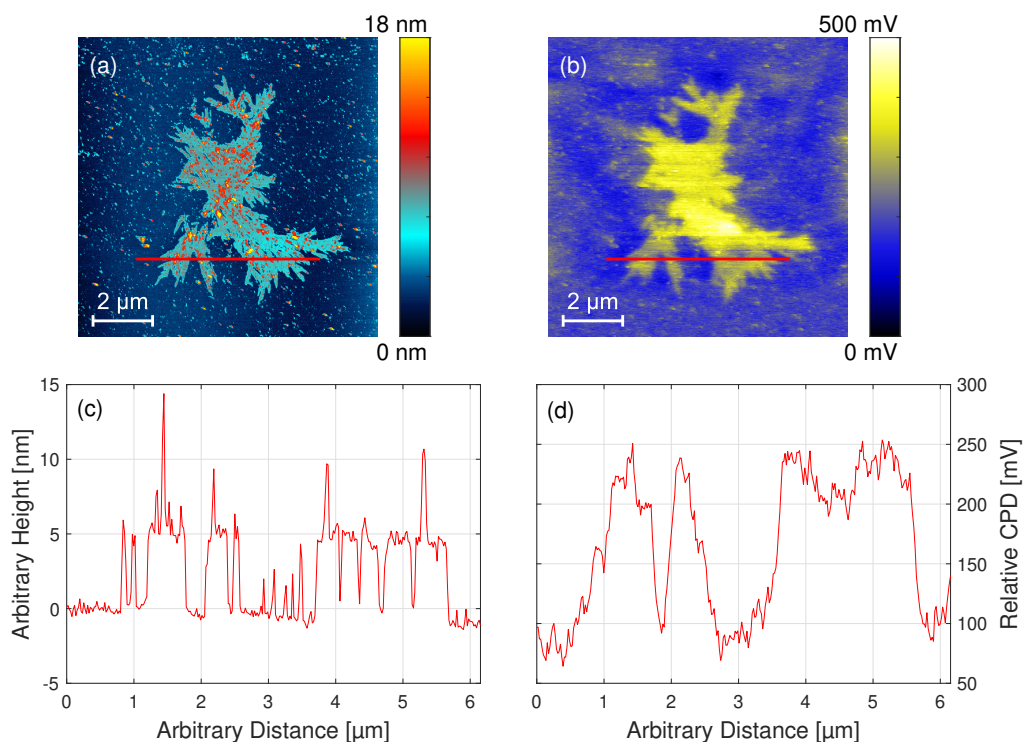


Figure 6.10 AFM measurement of a ramified island on sample IslAIN (a) topography and (b) the corresponding CPD map. Height and CPD profiles in (c) and (d), are taken from the red lines indicated in (a) and (b), respectively.

A clear correspondence between the surface topography and the local CPD is found in Fig. 6.9 and 6.10 from (a) and (b), respectively. Thus, the composition of the islands is clearly distinguishable from the material surrounding them.

However, as found from the CPD ranges in the profiles of Fig. 6.9(d) and 6.10(d), the relative CPDs are roughly the same at 150mV. These results support the idea that the islands are made of pure Al, and the supply of N has not been incorporated into the islands. This may also help explain why no notable morphological differences between N-depleted and N-rich growth environments have been found, as shown in Fig. 6.7 and the topography of Fig. 6.9(a) and 6.10(a).

6.1.3 General Considerations for Ramified Island Growth

In summary, the ramified islands form during the target cleaning process prior to the main deposition, and thus can be thought of as a parasitic effect in the magnetron sputtering system.

The islands are most probably made of pure Al, and always seem to form in layers with magic heights of around 5nm.

To understand the magic heights some additional investigations have been conducted. The magic height was assumed to be 5.3nm, which is the mean of all layer heights, and calculations were carried out to determine how many a and/or c lattice constants of Al_2O_3 , AlO and Al, which can fit into this magic number. The best agreement was obtained for FCC structured Al with lattice constant $a = 4.049\text{\AA}$ [88, p. 4-139], showing a very accurate correspondence to the height of 13 unit cells.

The idea of these calculations in number of unit cells is supported by Tournet [89], who found that Al thin film deposited on Si(111) formed a very homogeneous and unstrained structure. The Al thin film showed a lattice constant identical to that of bulk even down to few monolayers. This tendency of relaxed crystalline formation with lattice constant corresponding to that of bulk Al was also found down to 4ML by Liu et al. [90]. Though studies on stable height formation at 13 Al unit cells has not been found, clusters of magic sizes are a well known phenomenon [91][92]. Thus, these layers may consist of clusters with particularly stable sizes, but to verify this hypothesis a more comprehensive investigation must be conducted.

6.2 AlN Structures Grown by DC Magnetron Sputtering

This section will present the attempts of vertical NW growth by DC magnetron sputtering. Catalyst-free and catalyst-assisted approaches will be investigated, where the internal structure of the samples are of particular interest.

6.2.1 Catalyst-Free AlN Nanostructures

The SZM proposed by Thornton [93], which is further explained in App. F, predicts the formation of columnar structures with voided boundaries in Zone I and T for magnetron sputter deposited samples, which in theory would be able to produce well separated NWs. These zones span a large homologous temperature range, which for AlN means a substrate temperature range of $<600^{\circ}\text{C}$ for Zone 1 and $300\text{-}1050^{\circ}\text{C}$ for Zone T [1, p. 25]. The GaN samples grown by Junaid et al. [79] shown in Fig. 4.13 span the same zones [1, p. 17].

Two samples corresponding to the Zone 1 (RT and RTHP) and one sample corresponding to Zone T (GR07) have been made. Top-view and cross-sectional SEM images of these samples are shown in Fig. 6.11.

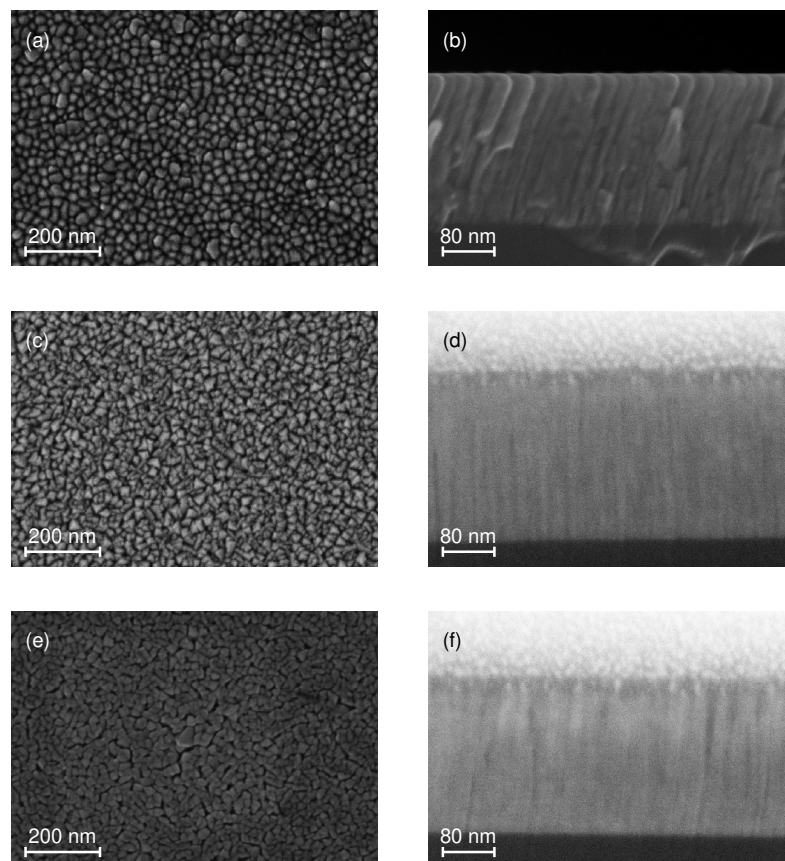


Figure 6.11 SEM images of temperature dependent morphology of nanostructures, showing the top-view (a), (c) and (e), as well as cross-sectional images (b), (d) and (f), for GR07, RT and RTHP, respectively.

The SEM image of a magnetron sputtered AlN sample, with a substrate temperature of 697°C and deposition pressure of 0.4Pa, are shown in Fig. 6.11(a) and (b). Columnar structures are visible, but with no indication of well-separated NW formation. The relatively high temperature enhances surface diffusion, which according to the SZM promotes the formation of a continuous film, with the columnar structure arising from preferred growth at nucleation sites. A cross-sectional image of the same sample is found in Fig. 6.11(b), which reveals the columnar structures, but with a high packing density. This corresponds well with the Zone T of the SZM. The tilt of the columns is a scanning artifact stemming from the SEM measurement and must thus be disregarded.

Fig. 6.11(c) shows a similar top-view SEM image of a sample (RT) with a significantly reduced substrate temperature of 27°C, but at the same process pressure. The reduced temperature should eliminate surface diffusion, such that shadowing effects dominate, promoting vertical growth. This is not found, instead a grainy surface with dense columns similar to the ones found on GR07 are formed, as found in Fig. 6.11(b). From the cross-sectional SEM image of Fig. 6.11(d), narrow and tightly grown columns can be seen. An explanation for this could be that the particle flux is too high, such that adatoms collide almost immediately and start nucleating. This would result in a high density of AlN nucleation sites, from which vertical columns may arise.

Fig. 6.11(e) show a sample (RTHP) grown at 35°C with a process pressure raised to 0.85Pa. The increased pressure should decrease the adatom energy further, as a smaller mean free path is available in the SC, resulting in an increased collision rate of the particles in the chamber. The decreased energy will further aid in the reduction of surface diffusion, which may lead to a preferential accumulation of adatoms at the site of impingement. Again, a dense columnar structure is found, which may again be attributed to a high particle flux. The cross-sectional SEM image of Fig. 6.11(f) shows a very similar crystal morphology to the one with a lower deposition pressure (RT) in (d), which suggests that the reduced adatom energy has not severely changed the surface diffusion during growth.

The growth model introduced in Sec. 3.2.3 may help explain why a preferred separation between the columns has not been achieved. The low substrate temperature is not sufficient to re-evaporate adatoms, resulting in an overabundance of nucleation sites. After the nucleation has occurred, the many columns grow as expected in the vertical direction, but inevitably coalesce due to the large column density.

6.2.2 Catalyst-Assisted AlN Nanostructures

In an attempt to grow more separated NWs, two samples were produced where the substrate had been prepared with catalytic particles. One sample substrate was covered with small Au particles with diameters around 20nm as can be seen in Fig. 6.12(a). Then sputter deposition of AlN was performed for 1h at room temperature resulting in the structure shown in Fig. 6.12(c).

On the other sample, larger Al particles with diameters around 100nm were deposited in situ. This was achieved by depositing pure Al for 40s at 678°C without any preliminary target cleaning.

In Fig. 6.12(b), a SEM image of a sample (IslAlNoShutter) prepared using this procedure is shown. Subsequently, main sputtering of AlN was performed for 1h at room temperature, with the results shown in Fig. 6.12(d).

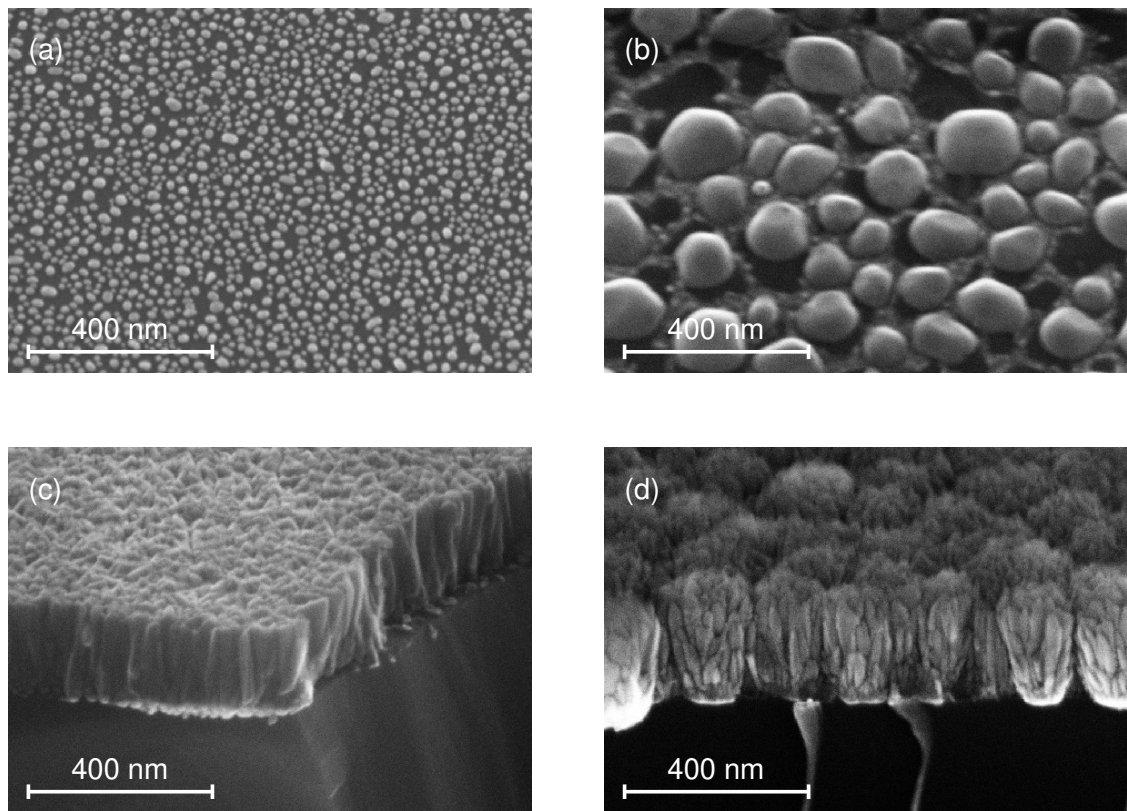


Figure 6.12 SEM images of catalyst nanoparticles (a) Au and (b) Al used for sputtered AlN growth shown in (c) and (d), respectively.

As can be seen in Fig. 6.12(c), the addition of Au catalysts does not result in separated NWs, but rather in a dense columnar structure, similar to those of the thin films presented above in Fig. 6.11. At the interface between the film and the substrate in Fig. 6.12(c), somewhat distinguishable grains with similar lateral dimensions as the Au catalyst seem to form, but the grown structures above the interface are completely coalesced. It might be the case that the Au catalyst particles are simply too closely spaced for coalescence to be avoided. Another possibility is, that the catalysts are too small for any stable NWs to form. In a study by Maliakkal et al. [54], it is argued, that the Gibbs-Thomson effect dominates when the catalysts are around 23nm and below in diameter. The Gibbs-Thomson effect describes the increased vapour pressure observed for curved surfaces. Assuming that the catalytic particles are spherical, the vapour pressure increases exponentially as the catalyst radius decreases [28, p. 15]. As such, significantly more desorption is expected from small catalysts, which can suppress the growth of NWs. The optimal size catalytic growth may vary, but good results are often found at diameters around 150-200nm [76].

Fig. 6.12(d) shows, that using large Al catalysts has quite a significant impact on the resulting structure. Separated flower-bud structures seemingly grow on top of the catalysts. This suggest

that the catalysts manage to act, as intended, as preferred nucleation sites for diffusing adatoms. This tendency for AlN to form nanoflowers was also found by Pietrantonio et al. [94], who studied AlN grown by magnetron sputtering. Here, nanoflowers grew on top of an RhB substrate containing grains and droplets up to micrometer size, which were found to act as preferred nucleation sites. In this study, it was observed that increasing the substrate temperature from 300°C to 500°C led to nanoflowers becoming more round, and flower-petals more smooth, which might stem from the increased diffusion of adatoms. Thus, it is possible that the diffusion of Al adatoms is too low for a continuous NWs to form, and that the formation of nanoflowers might be avoided by enhancing the diffusion through an increase in the substrate temperature.

This idea was tested and another sample was produced with Al catalysts identical to those presented in Fig. 6.12(b), and sputter deposited with AlN for 10min at around 900°C. A SEM image of the sample is shown in Fig. 6.13

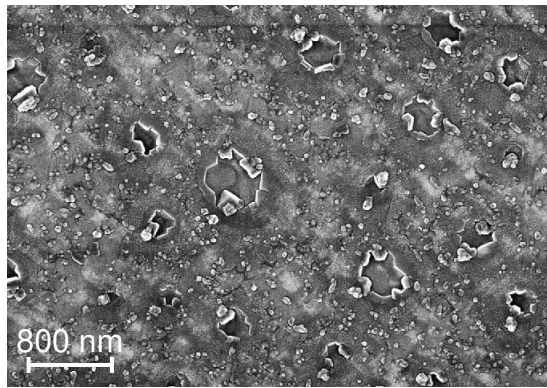


Figure 6.13 SEM image of sputter deposited AlN on Al catalyst at high temperature ($\sim 900^\circ\text{C}$), with formation of craters.

The sample surface shown in Fig. 6.13 has a generally grainy microstructure with some large crater-like indents. It is believed that the craters are a result of evaporation of the Al catalysts. As the substrate is heated to 900°C, a large amount of the Al can be expected to start evaporating. As a result, the surface no longer contains any catalytic particles to facilitate nanostructure growth.

6.3 Morphology and Composition of AlN Nanostructures Grown by MOCVD

In this section we present the results for the growth of nanostructures using MOCVD. The general aim of this part of the study was to adjust different growth parameters to facilitate growth in the vertical direction, in an attempt to eventually achieve NW growth. All MOCVD-grown samples were made on substrates prepared with Au catalyst particles. The process used for producing the catalysts is described in Sec. 5.2, and were identical for all samples. A SEM image showing the surface of a catalyst-prepared substrate can be found in Fig. 5.3.

To understand the growth evolution of the nanostructures, the influence of deposition time was studied. In Fig. 6.14, SEM images are presented, showing two samples (MOCVD2 and MOCVD4) grown under similar conditions but with a deposition time of (a) 25min and (b) 1h, respectively.

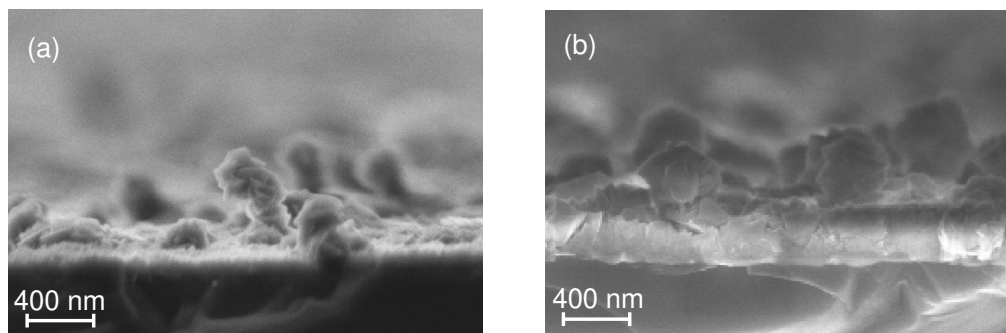


Figure 6.14 Cross-sectional SEM images of sample with MOCVD grown nanostructures grown for (a) 25min (MOCVD2) and (b) 1h (MOCVD4).

At a lower deposition time, clear vertical growth occurs, where randomly oriented flakes are arranged in a rod-like structure as shown in Fig. 6.14(a). Increasing the deposition time leads to suppression of the vertical growth, and flakes form in the wider structures as observed in Fig. 6.14(b). As growth conditions otherwise are identical, the widening of the columns may arise due to insufficient adatom energy to climb the flaky sidewalls of the vertical structures. Instead, the Al particles are forced to attach to the bottom of the rod and start incorporating there.

Another effect occurs at a deposition time of 1h as shown in Fig. 6.15, which shows SEM images of protrusions found on two samples (MOCVD4 and MOCVD5) grown under similar conditions.

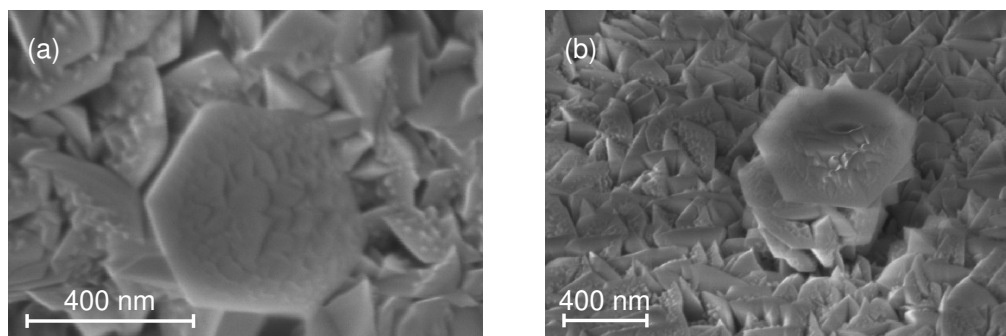


Figure 6.15 SEM image of hexagonal structure on (a) sample MOCVD4 after 1h of deposition time. (b) shows the same structure at an angle of 45° on sample MOCVD5, with identical growth conditions apart from a small reduction in TMAI supply.

At 1h of deposition time, some of the protrusions, which consist of randomly oriented flakes, develop hexagonally shaped flat tops, as shown in both Fig. 6.15(a) and (b). This hexagonal structure usually corresponds to c -planes in a WZ material, and was observed in several studies [62][31][76]. As discussed in Sec. 2.1.3, the most favoured shape for a WZ NW is a hexagonal rod with m -planar sidewalls and a c -plane top caused by the very low surface energy of m -planes [30]. In Fig. 6.15, the hexagonal shape is found only at the top, suggesting that the growth initially is chaotic, where

diffusion-driven growth forms the coalesced flakes. It is hypothesised that, at some point during the growth of the granular structure, a flat boundary is formed, where the favourable growth in the c -axis direction start to occur. The diffusion driven growth discussed in Sec. 3.2.3 mentions low roughness of GaN m -plane sidewalls, which makes diffusion easier as steps and terraces are less prominent. As found in Fig. 6.14 and 6.15, the sidewalls are far from homogeneous, which restricts further vertical growth of the protrusions. Fig. 6.15(a) shows a rough hexagonal top, which may help trapping adatoms. However, due to the limited sidewall diffusion, the only contribution to the lateral growth would occur from impinging particles directly on the top of the protrusions.

Subsequently, the effects of increasing temperature was investigated. In Fig. 6.16, two samples deposited for approximately 25min using at temperatures (a) 800°C (MOCVD1) and (b) 1000°C (MOCVD2), are presented. A distinct feature of the surfaces of both samples is the presence of three-dimensional flower-like structures, similar to those found on the Al catalyst-assisted AlN structures obtained by magnetron sputter deposition as shown in Fig. 6.12.

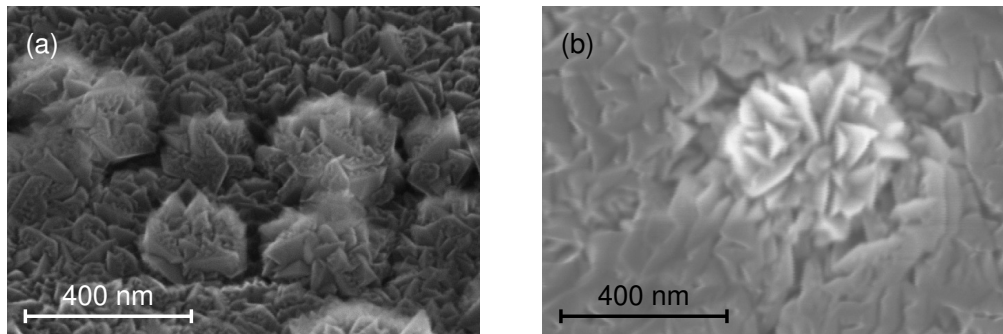


Figure 6.16 SEM images of the surface morphology of MOCVD grown samples at temperatures of (a) 800°C and (b) 1000°C, respectively.

The diameters of the nanoflowers shown in Fig. 6.16 are in the range of 200-400nm, and thus correspond roughly in size to those of the Au catalysts. This might indicate that the catalysts promote some growth in the vertical direction, but further investigation is needed to determine whether the nanoflowers actually grow from the catalyst or not. This tendency for AlN to form nanoflower structures is not a unique observation. Most notably, these nanoflowers are very similar to those found by Cimalla et al. [77], whose results were presented in Fig. 4.11 in Sec. 4.2.1. It was suggested that nanoflowers arise due to the relatively low diffusion of Al adatoms, which causes the formation of lamella on a catalyst particle, and that a more NW-like structure might form by increasing the temperature.

Comparing the nanoflowers found in Fig. 6.16(a) and (b), it can be seen, that raising the temperature from 800°C to 1000°C leads to a slightly smoother surface structure, which can be explained by the higher diffusion rate caused by the increase in kinetic energy of the surface adatoms. However, the protruding structures still resemble nanoflowers rather than NWs. It is possible, that AlN NWs cannot be obtained without increasing the temperature even further.

Since the temperature of the MOCVD system used in this study is limited to 1090°C, an

additional sample (MOCVD6) was made at this temperature. It was found that the temperature increase did not further promote vertical growth, and nanoflowers were still formed. However, the surface of sample MOCVD6 was found to exhibit areas with well-defined nanopores, as is shown in Fig. 6.17.

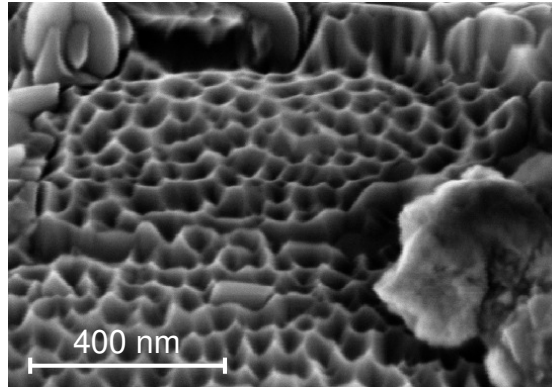


Figure 6.17 SEM image of the nanopore structure present on the sample grown at 1090°C (MOCVD6)

This surface is very similar in structure to the AlN buffer layers grown by Bertness et al. [62] as shown in Fig. 4.1 of Sec. 4.1.1, where the nanopores helped facilitate GaN NW growth. Achieving a homogeneous buffer layer of well-defined holes, without the protrusions or domain formation found in the current samples, may be used in a similar way to promote NW growth. However, optimisation of the growth process would be required.

In addition to the effects of temperature and deposition time, the influence of increasing the process pressure was investigated. The surface morphology of a sample grown at 50Torr (MOCVD6) and 200Torr (MOCVD7) can be seen in Fig. 6.18(a) and (b), respectively.

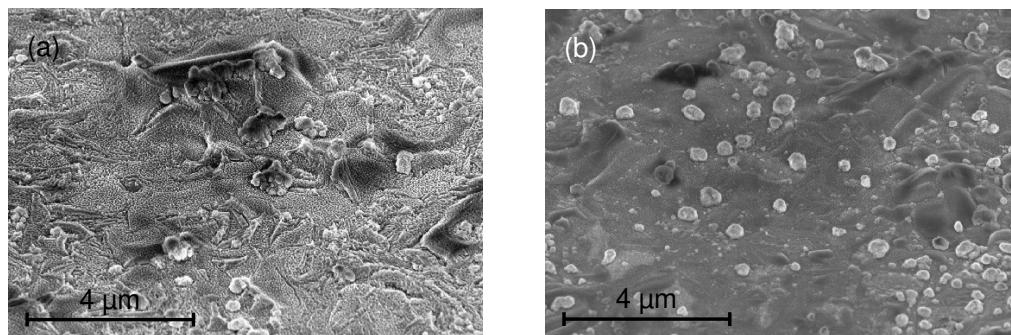


Figure 6.18 SEM images of samples grown at process pressures of (a) 50Torr (MOCVD6) and (b) 200Torr (MOCVD7), both at an 45° angle, illustrating the effects higher pressure has on the protrusion growth rate and overall roughness.

The formation of nanopores is suppressed as the process pressure is raised, and instead a more continuous surface is observed. This might allow adatoms to easier diffuse and aggregate into larger clusters, thus facilitating the diffusional growth of NWs. Furthermore, the protrusions become more distinguishable from the surroundings as the pressure is increased, and their structure is less like

nanoflowers, as otherwise shown in Fig. 6.16, but something more comparable to initial stages of NW growth.

This agrees with the findings of Ra et al. [76], as discussed in Sec. 4.2.1, where keeping the process pressure sufficiently high was crucial for promoting vertical growth. Here, short GaN NWs started forming at 200Torr, and became longer and more ordered as the pressure was further increased.

This effect can be explained through the findings of Ko et al. [31] which were described in Sec. 4.2.1. Here, performing MOCVD under high process pressure accentuated the differences in growth rates between crystalline planes. In particular, the growth rate of $(000\bar{1})$ -planes, which are expected to constitute the tops of WZ NWs, was found to increase as the process pressure was raised, promoting vertical growth. Note, that for this mechanism to facilitate vertical growth of the protrusions presented in Fig. 6.18, they should be relatively well-ordered, and oriented with the c -axis perpendicular to the sample surface.

If the competitive growth of differently oriented planes in the protrusions is dominated by a particular plane, the protrusions might become more well-ordered, but further investigations of the crystalline structure and orientation are required to confirm, if this is the case.

Lastly, it should be mentioned that a final sample (MOCVD8) was made where the pressure was kept at 200Torr. The ratio of NH_3 and TMAI was kept the same, but the total flow was greatly reduced. The hypothesis was, that lowering the flow would cause the collision rate of adatoms to decrease, allowing them to diffuse longer on the surface and thus promote growth on top of the protrusions. However, SEM images revealed that while the sample surface became slightly smoother, no significant difference could be found between the protrusion found on this sample and those on MOCVD7 depicted in Fig. 6.18(b).

The internal structure of a typical nanoflower found on the samples grown under low pressure can be seen in Fig. 6.19. Here, a SEM image reveals the cross-section of a nanoflower on MOCVD5.

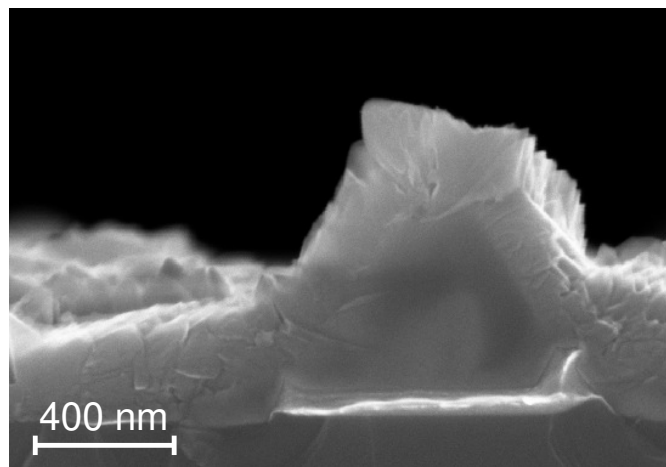


Figure 6.19 Cross-sectional SEM images of sample MOCVD5 showing the internal structure of the deposited material at and next to a nanoflower.

From Fig. 6.19 it can be seen that the structure within the nanoflower is very smooth, with a sharp boundary formed between the interior and the flaky surface on the outside. The smoothness of the structure indicates a good crystallinity, which may occur due to high adatom mobility in the initial stages of growth.

At the interface between the protrusion and the substrate, a bright layer can be seen in Fig. 6.19, which is believed to originate from the catalytic Au particle.

Further investigations on the presence or absence of Au on top of protrusions were conducted using EDX. Fig. 6.20 shows three points where the atomic composition were measured. Here, points 1 and 3 correspond to the top of protrusions, and 2 correspond to the surrounding surface. The resulting N, Al and Au atomic percentages can be found in Tab. 6.6.

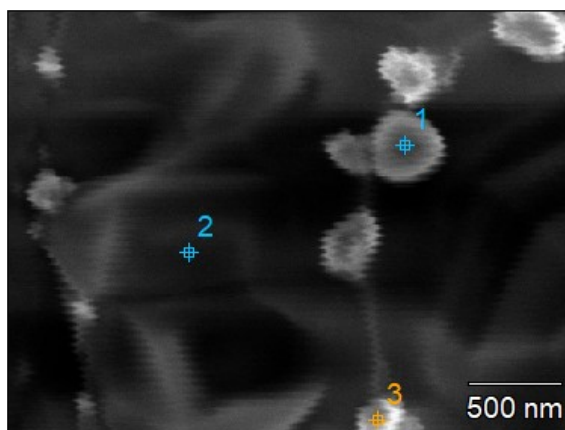


Figure 6.20 SEM image indicating the areas of EDX measurement of sample MOCVD8.

Table 6.6 Atomic percentages measured by EDX on the three points shown in Fig. 6.20.

Marker	Atomic Percentage of N [%]	Atomic Percentage of Al [%]	Atomic Percentage of Au [%]
1	44	2	3
2	48	2	0
3	37	6	9

As evident from Tab. 6.6, Au is not present on the surface as the atomic percentage here was found to be 0%. The low values of 3% and 9% on the protrusions for point 1 and 3, respectively, indicate that some Au is present at these particular protrusion. This suggests that the catalysts act as preferred nucleation sites for protrusions, and do indeed promote vertical growth. A similar tendency for catalysts to act as seeds for nucleation was also found by Ra et al. [76].

6.4 GaN Nanowires Grown by MBE

This section will discuss the results obtained for NWs grown using catalyst-free MBE, which have been produced at the Institute of Physics at the Polish Academy of Sciences, as explained in Ch. 5. As these NWs were of known quality, the point of interest were to study the features of successfully grown NWs, with an emphasis on the structural morphology and electrical properties.

6.4.1 Morphology of GaN Nanowires

During growth of the GaN NWs, the samples were subjected to a radial temperature gradient caused by the geometry of the substrate heater. Thus, the effects of temperature can be examined by inspecting different areas of a sample. Fig. 6.21 shows SEM images taken from a (a) low temperature, (b) intermediate temperature and (c) high temperature area of sample MBE2. For this sample, the highest temperature was $\approx 790^\circ\text{C}$ and the lowest $\approx 760^\circ\text{C}$.

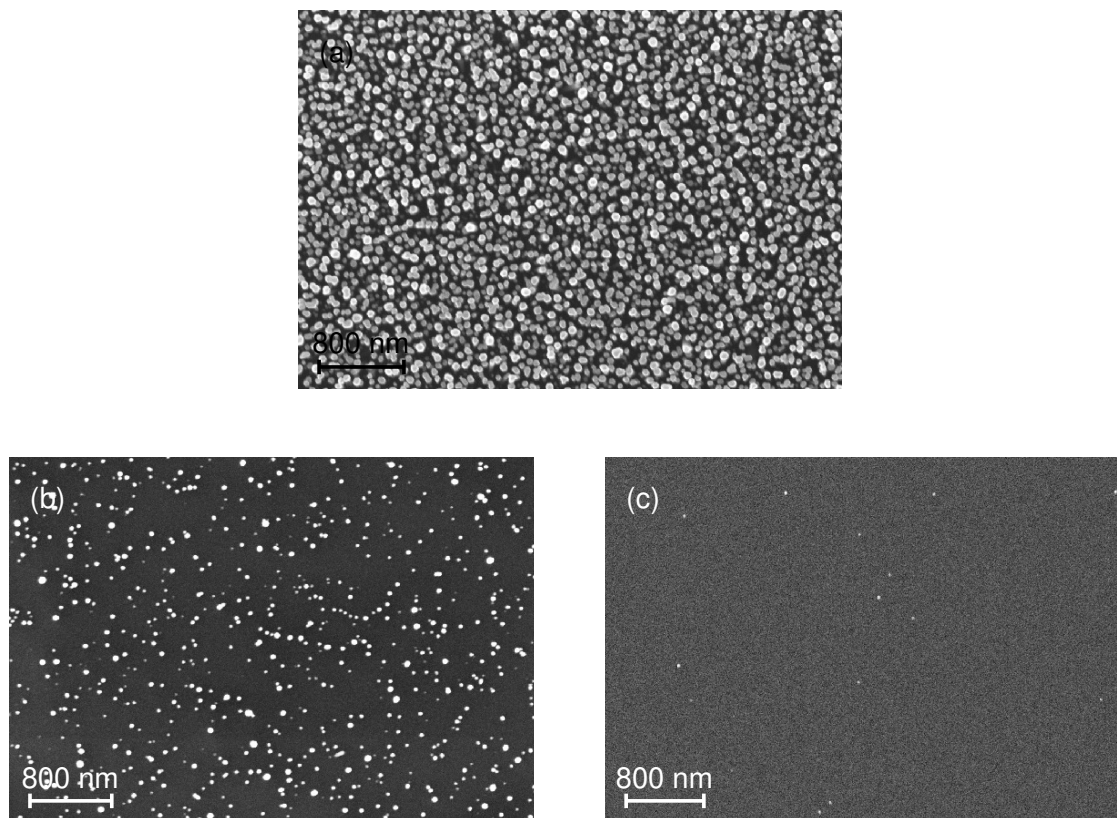


Figure 6.21 SEM images of GaN NWs on MBE2 in areas of (a) low temperature, (b) intermediate temperature and (c) high temperature.

It is evident from Fig. 6.21, that the surface density drastically decreases as the temperature is increased by only about 30°C . This observation can be understood in the framework of the model for catalyst-free growth mechanism described by Ristić [58], as discussed in Sec. 3.2.3. As Ga atoms are adsorbed onto the substrate surface, they diffuse across the surface of the substrate, where they either re-evaporate or collide with other atoms to form larger clusters. Eventually,

the clusters reach their critical size, and the surface density of these larger clusters will be equal to that of the resulting NWs. In the ideal case, the distance between stable clusters is equal to twice the diffusion length, which depends on the temperature in accordance with Eq. (3.3). Here, higher temperatures increases the distance between clusters, hence the surface density of NW is reduced. The exponential relation explains, why this decrease is quite drastic, even though the growth temperature of MBE2 spans only 30°C. In fact, a similar large reduction in the surface density of GaN NWs was found by Mata et al. [66] for growth temperatures in the range of 775-805°C, as shown in Fig. 4.2. This result emphasises that the temperature range for NW growth is quite narrow when using MBE.

In Fig. 6.22, a top-view of MBE1, which is the sample grown with the lowest temperature, can be seen.

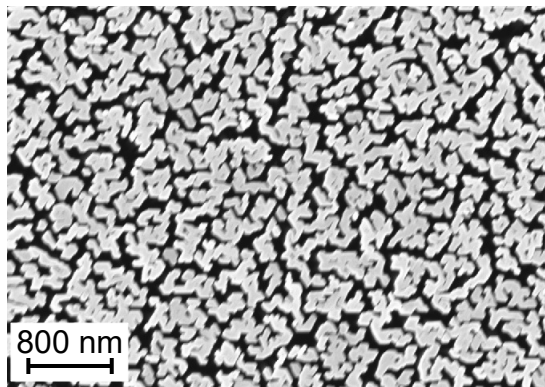


Figure 6.22 SEM images of GaN NW on MBE1, showing a low temperature area of the sample.

The short diffusion length of adatoms at low temperatures causes the surface density of the stable clusters to become too high, for the NWs to avoid coalescing during growth. As a consequence, the sample in Fig. 6.22 contains almost no free-standing NWs, but is instead covered by a maze-like structure of protruding columns. A similar result was found by Serban et al. [78], who reported that NW coalescence became increasingly prevalent as the temperature was decreased, eventually resulting in columnar thin film.

Apart from the surface density, the overall structure of the NWs is also affected by the temperature. Fig. 6.23 shows cross-sectional SEM images taken from varying substrate temperatures, where the temperature is gradually increasing from (a) to (c).

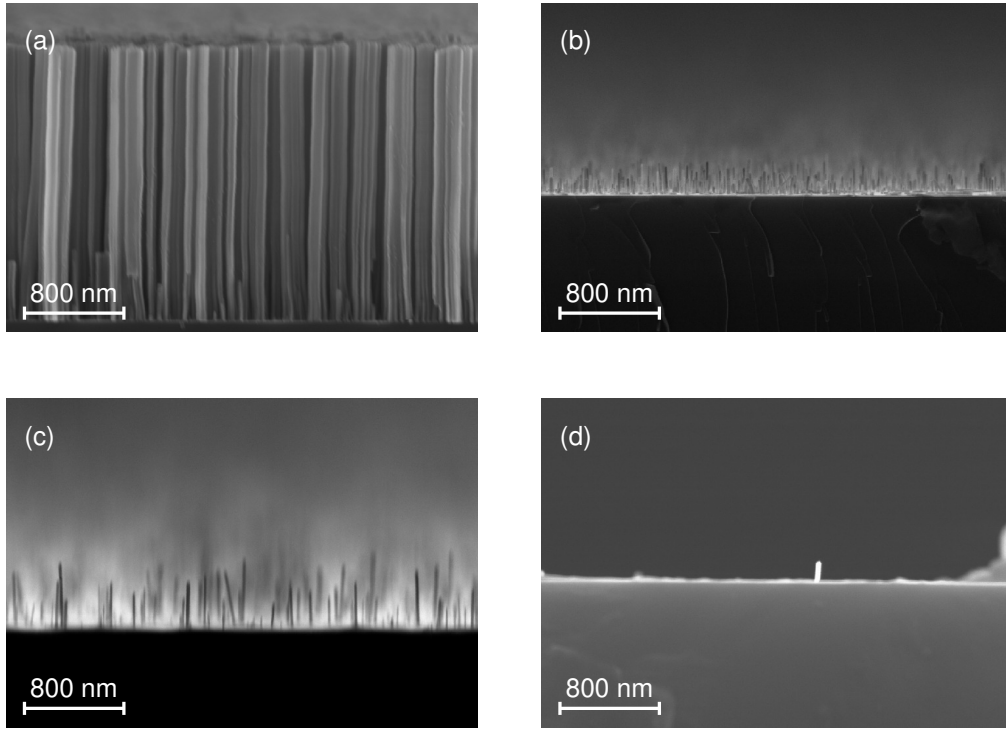


Figure 6.23 Cross-sectional SEM images of GaN NWs grown on samples: (a) MBE1, (b) MBE3, (c) MBE4 and (d) MBE2.

A clear difference between the samples in Fig. 6.12 can be seen in the dispersion of NW height. In Fig. 6.23(a) one can see the cross-section of NWs grown at the area with low temperature showing that the height is almost identical for each NW. The effect stems from the initial nucleation stage as described in Sec. 3.2.3. When the temperature is low, the adatoms are less likely to re-evaporate, and thus, clusters are expected to reach their stable size approximately simultaneously.

Increasing the temperature leads to a decrease in NW length and an increase in the dispersion of heights, as shown in panel (b) and (c). The higher rate of adatom desorption results in a bigger variation in the time it takes for each cluster to reach critical size during the initial nucleation stage. As a consequence, NWs begin growing at different times, hence height variations can be expected. The temperature of the sample shown in Fig. 6.23(d) is unknown. But the fact that a lone NW is found indicates that the local re-evaporation is very high, which would mean a relatively high temperature. Here the probability of clusters reaching critical size is too low for NWs to consistently form.

This is in agreement with what was found by Mata et al. [66], as shown in Fig. 4.2, where a larger height dispersion was found as the temperature was increased from 775-805°C, and no NWs were found at temperatures above 805°C.

The diameter of NWs also seem to depend on temperature, as the NWs shown in Fig. 6.23(a) have a larger diameter compared to the rest. This tendency actually disagrees with what was predicted by the NW growth model by Ristić et al. [58] presented in Sec. 3.2.3. Here, it was argued that higher temperatures leads to thicker NWs, because the critical size of clusters during

the nucleation stage is larger. However, the fact that the opposite is true in our case might be caused by a low flux of Ga. If the flux is not sufficiently high, the increased re-evaporation at high temperatures might instead cause the clusters to decrease in size, thus leading to thinner NWs.

6.4.2 Electrical Properties of GaN Nanowires

As mentioned in Sec. 2.1.2, the CPD of a NW is sensitive to its polarisation, as N- and Ga-polarised surfaces have different work functions. Hence, KPFM measurements may identify the polarisation of NWs, which is relevant for several application purposes.

KPFM measurements of a sample with low NW surface density is shown in Fig. 6.24, with the topography (a) and CPD map (b). Height and CPD profiles formed by the red and green lines in (a) and (b), are shown in the graphs of (c) and (d), respectively.

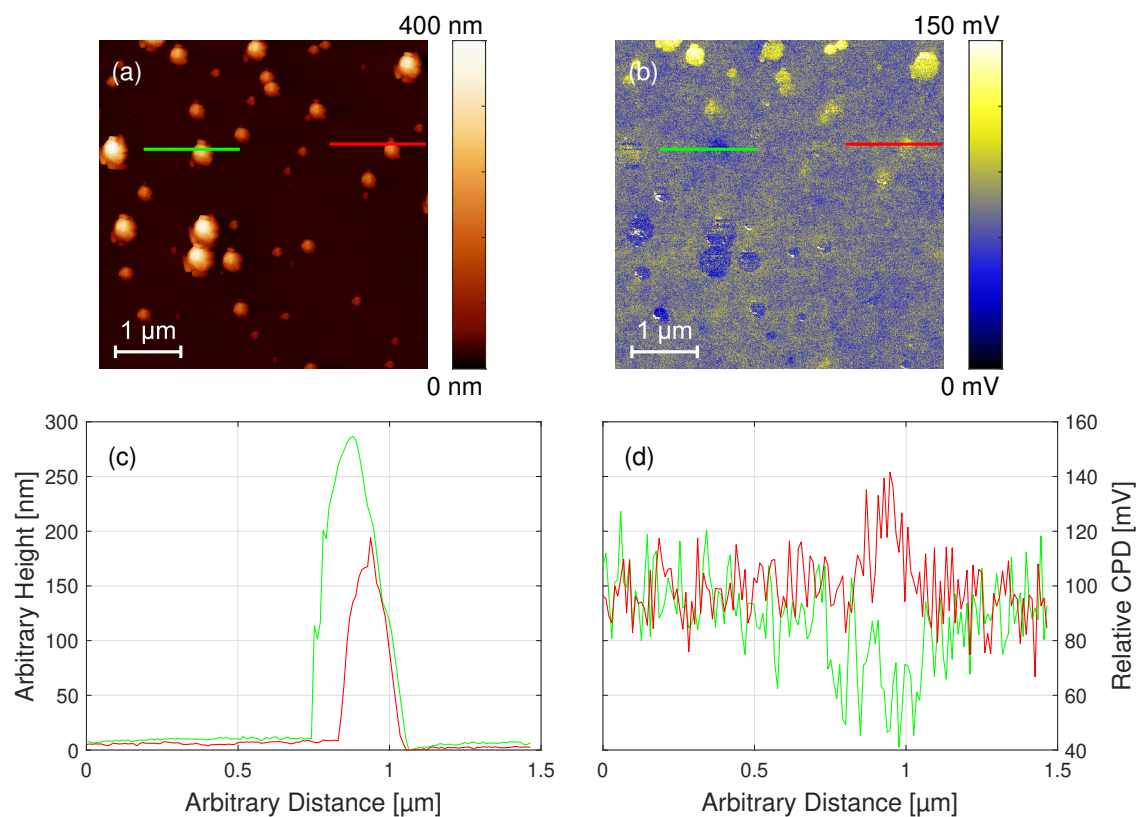


Figure 6.24 AFM images of (a) the topography of sample MBE4 and (b) the corresponding CPD map. Profiles taken from the red and green lines in (a) and (b), are shown in (c) and (d) for the height and CPD profiles, respectively.

The topography and CPD map clearly shows the existence of alternate CPD on different NWs. The line profiles in Fig. 6.24(d), shows an almost mirrored effect on the CPD, as both NWs have a difference of around 40mV in opposite directions, as compared to the surrounding material. This mirroring phenomenon is only observed on this particular sample. As mentioned in Sec. 2.1.2, Hetzl et al. [24] found Ga-polar NWs to exhibit a higher CPD compared to N-polar. Using this convention, the NW to the right (red line) in Fig. 6.24(d) may be classified as being Ga-polarised, and the NW to the left (green line) as N-polarised. However, whether or not it is the Ga- or

N-polar NW tops which has the highest CPD value is not agreed upon, and neither is their exact CPD values [24][22][26]. Furthermore, oxidation due to the ambient atmosphere, may alter the composition, and the work function of the surface. Other environmental factors, like humidity and contaminants would also affect the measurements. Thus, a more rigorous study would be required, in order to fully conclude on the polarisation states of the NWs.

The AFM and KPFM measurements presented in Fig. 6.25 show the topography (a) and CPD map (b) of the more densely packed GaN NWs on MBE3. Height and CPD profiles of NWs with distinct height differences are shown in Fig. 6.25(c) and (d).

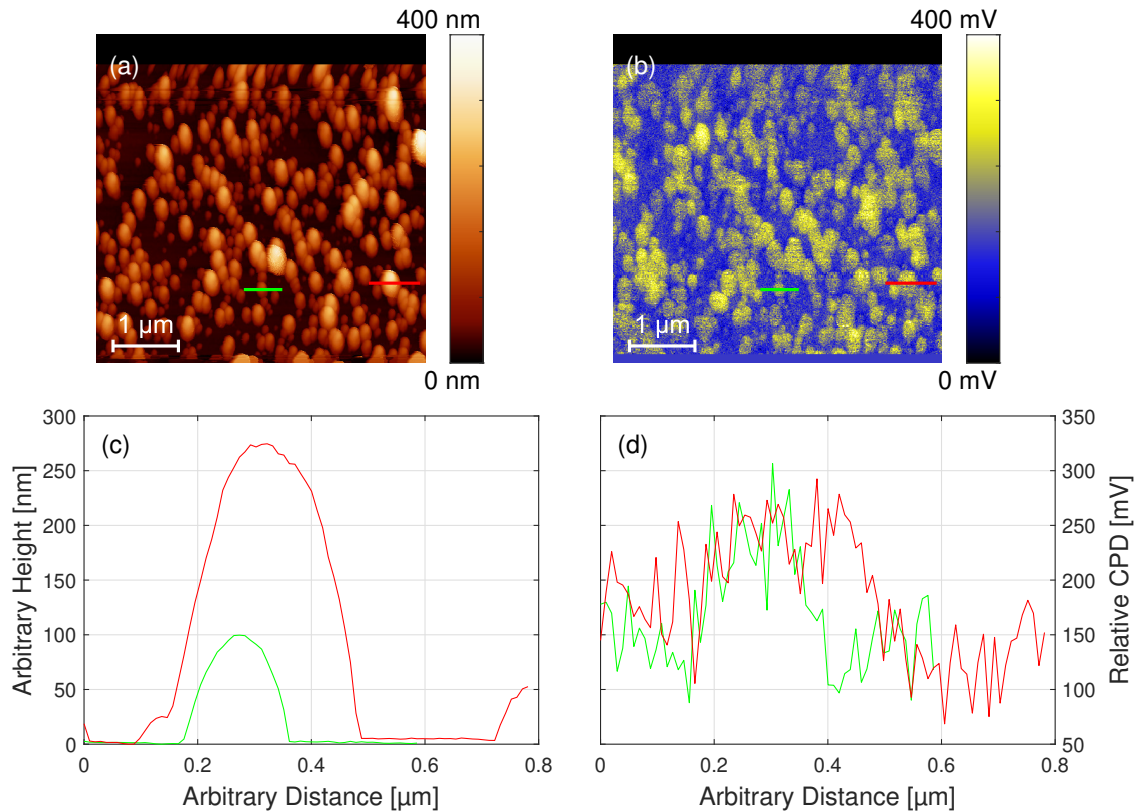


Figure 6.25 AFM images of (a) the topography of sample MBE3 and (b) the corresponding CPD. The plots in (c) and (d) corresponds to the height and CPD profiles, respectively.

The topographical profile in Fig. 6.25(c) show a NW with an approximate height of 100nm (green line), and a much higher NW around 270nm (red line). The corresponding CPD of these NWs are shown in Fig. 6.25(d). Despite the difference in height, the CPD for both NWs is almost identical, indicating the same polarity. From Fig. 6.25(b), one can see that no large difference in the CPD values are found for other NWs.

The NWs measured on this sample seem to be of the same polarity, as their corresponding CPDs are all similar and higher compared to that of the substrate surface. However, full knowledge on the possible presence of both N- and Ga-polar NWs is not evident. An analysis of the distribution of relative CPD was made in an effort to conclude on the presence of NWs with different polarity. However, the analysis was inconclusive, as further explained in App. G.

CONCLUSIONS

AlN nanostructures have been grown using DC magnetron sputtering and MOCVD. Subsequent analysis of these structures, along with MBE grown NWs is presented in the results and discussions of Ch. 6. The aim of this chapter is to elaborate on the most important conclusions which may be drawn.

Nanostructures by DC Magnetron Sputtering

Growth of ramified islands occurs at the early stages of magnetron sputter deposition. These islands are believed to consist of pure Al, since their prevalence and microstructure are similar regardless of whether or not N is supplied to the system during deposition. Island formation was found on all sputter-deposited samples and is thought to be a parasitic effect related to the initial target cleaning process in the particular sputter system used.

One more phenomenon of high fundamental interest for understanding the nucleation stage, is that the islands consist of layers, which grow in "magic" height steps of approximately 5.3nm. The magic heights are preserved independent of island size, deposition time and presence of N during deposition.

The surface coverage of the islands could be increased by extending the pure Al deposition time with shutter, before introducing N to the system. However, even when no N was supplied, the Al islands did not completely aggregate but stabilised at a surface coverage of approximately 14%. The islands which form when N is supplied from the very beginning expands more slowly in the lateral direction. This might be attributed to a decrease in sputtering yield due to a higher level of target poisoning, as well as a lower adatom diffusion caused by the increasing amount of N present on the substrate surface.

As the deposition time was increased, a continuous grainy layer of AlN began to grow on top of both islands and substrate surface. The atomic concentrations of Al and N were similar both on top of and away from islands, hence, islands did not act as preferred nucleation sites for diffusing AlN adatoms during the sputter deposition without shutter.

From the clear difference in CPD between Al islands and the material surrounding them, it can be concluded that they possess different elemental compositions.

Removing the shutter and excluding the supply of N during sputtering resulted in the growth of large spherical Al particles with diameters up to 200nm. When used as catalyst for further growth of sputter deposited AlN, the particles clearly served as nucleation sites for the growth of

separate pillars with flower-like structures. While increasing the growth temperature and thus the kinetic energy of adatoms should lead to more coalesced structures, it was found to cause unwanted removal of the Al catalysts in the early stages of growth.

The attempt of growing magnetron sputtered AlN NWs without the use of catalytic particles resulted in densely packed columnar structures, which coalesced into thin films. The diffusion length of adatoms is likely too small for well-separated NWs to form, and further adjustments of sputtering parameters are required for coalescing to be avoided.

Thus, the studies resulted in important findings which can be used for further improvements of the sputtering system in order to grow pure AlN structures, as well as to develop strategies on how to adjust the sputtering parameters in order to make a transition from planar 2D film growth towards 1D vertical nanostructures. However, further investigations are required for NW growth to be realised.

AlN Nanostructures by MOCVD

Growth of AlN nanostructures was found to be possible using MOCVD assisted by catalytic Au particles. On top of the catalysts, growth of protrusions with diameters in the range of 200-400nm were found. The protrusion formed flower-like structures due to limitations in the Al adatom diffusion. Raising the temperature increases adatom diffusion, which led to a smoother nanoflower surface, however, at a temperature of 1090°C the structure of protrusions were still distinctly flower-like.

For a deposition time of 25min at 1000°C, vertical growth of nanoflowers is favoured. However, at 1h of deposition, adatoms are incorporated at the sides of the nanoflowers rather than on top, likely due to the flaky structure limiting the diffusion on sidewall. The longer deposition time also resulted in hexagonal flakes forming on top of some protrusions likely corresponding to the {0001}-plane of wurtzite AlN.

Increasing the process pressure from 50Torr to 200Torr leads to a smoother surface with more distinguishable protrusions. These protrusions no longer have nanoflower structures, but resembles large uniform particles. This can be attributed to the increased pressure enhancing the growth rate of particular crystal planes, leading to smoother and more well-ordered surfaces. More studies involving adjustment of gas flows and gas ratios are required for better understanding on how to achieve 1D nanostructures.

GaN Nanowires by MBE

The growth temperature had a significant impact on the surface density and height dispersion of MBE-grown GaN NWs. At lower processing temperatures, NWs were closely spaced due to the small diffusion length of adatoms resulting in a high surface density of nucleation islands at the early stages of NW growth. The NWs were similar in height because the low rate of re-evaporation of adatoms causes the nucleation islands to reach critical size approximately simultaneously. In-

creasing the substrate temperature leads to the formation of NWs with low surface density, which exhibited a large dispersion in heights.

A distinct difference in the CPD was found between the NW tops and surrounding substrate stemming from the difference in elemental composition. On one of the samples with a relatively dense packing of NWs, the CPD was very similar on each NWs which indicates that they exhibit identical polarities. On a different sample grown at a higher temperature and exhibiting a lower surface density, approximately half of the NWs exhibited a distinctly lower CPD, while the other half displayed a higher one. This difference in CPD most probably originates from the NW tops being either Ga- or N-polarised. Further investigation is required in order to identify which polarisation corresponds to a particular CPD.

Final Note

In summary, it can be concluded that different methods can be used for the growth of III-V nanostructures. For both sputter deposited and MOCVD-grown AlN structures, the utilisation of pre-deposited catalyst particles was essential for promoting vertical growth. However, further optimisation of growth parameters must be explored in order to achieve AlN NWs. The characterisation techniques employed for MBE grown NWs has been found to accurately describe the morphology and electronic properties of NWs. However, KPFM on NWs requires a more rigorous study in order to fully determine their polarity.

BIBLIOGRAPHY

- [1] H. Morkoc. *Handbook of Nitride Semiconductors and Devices*. Wiley-VCH, 2008.
- [2] B. J. May, A. T. M. G. Sarwar, and R. C Myers. Nanowire LEDs Grown Directly on Flexible Metal Foil. *Applied Physics Letters*, 108:141103, 2016.
- [3] M. Ruzzarin, C. De Santi, F. Yu, M. F. Fatahilah, K. Stempel, H. S. Wasisto, A. Waag, G. Meneghesso, E. Zanoni, and M. Meneghini. Highly Stable Threshold Voltage in GaN Nanowire FETs: The Advantages of p-GaN Channel/Al₂O₃ Gate Insulator. *Applied Physics Letters*, 117, 2020.
- [4] Z. Wang, X. Pan, Y. He, Y. Hu, H. Gu, and Y. Wang. Piezoelectric Nanowires in Energy Harvesting Applications. *Advances in Materials Science and Engineering*, 2015:1, 2015.
- [5] N. Jamond, P. Chrétien, L. Gatilova, E. Galopin, L. Travers, J. C. Harmand, F. Glas, F. Houzè, and N. Gogneau. Energy Harvesting Efficiency in GaN Nanowire-Based Nanogenerators: The Critical Influence of the Schottky Nanocontact. *Nanoscale*, 9:4610, 2017.
- [6] C. Zhou, Y. Yang, H. Jin, B. Feng, S. Dong, Ren T. Luo, J. and, M. Chan, and C. Y. Yang. Surface Acoustic Wave Resonators Based on (002)AlN/Pt/Diamond/Silicon Layered Structure. *Thin Solid Films*, 548:425, 2013.
- [7] A. Stefanescu, A. Muller, I. Giangu, A. Dinescu, and G. Konstantinidis. Influence of Au-Based Metallization on the Phase Velocity of GaN on Si Surface Acoustic Wave Resonators. *IEEE Electron Device Letters*, 37:321, 2016.
- [8] J. W. Chung, W. E. Hoke, E. M. Chumbes, and T. Palacios. AlGa_N/Ga_N HEMT with 300-GHz f. *IEEE Electron Device Letters*, 31:195, 2010.
- [9] A. Bao. Group III-Nitride Nanowires. *Materials Science and Technology*, 33:765, 2017.
- [10] C. Kittel. *Introduction to Solid State Physics*. John Wiley & Sons, 2005.
- [11] M. Meneghini, G. Meneghesso, and E. Zanoni. *Power GaN Devices: Materials, Applications and Reliability*. Springer International Publishing AG, 2016.
- [12] H. Masui, S. C. Cruz, S. Nakamura, and S. P. DenBaars. Geometrical Characteristics and Surface Polarity of Inclined Crystallographic Planes of the Wurtzite and Zincblende Structures. *Journal of Electronic Materials*, 38:756, 2009.

- [13] Harmeet Bhugra and Gianluca Piazza. *Piezoelectric MEMS Resonators*. Springer International Publishing AG, 2017.
- [14] E. Li, S. Song, D. Ma, N. Fu, and Y. Zhang. Synthesis and Field Emission Properties of Helical GaN Nanowires. *Journal of Electronic Materials*, 43:1379, 2014.
- [15] Klaus Hermann. *Crystallography and Surface Structure: An Introduction for Surface Scientists and Nanoscientists*. Wiley-VCH, 2017.
- [16] K. M. Gupta and N. Gupta. *Advanced Electrical and Electronics Materials: Processes and Applications*. Wiley, 2015.
- [17] M. Zhong. Heterostructures of III-Nitride Semiconductors for Optical and Electronic Applications. In B. Roul, G. Chandan, S. Mukundan, and S. B. Krupanidhi, editors, *Epitaxy*, pages 171–201. IntechOpen, 2018.
- [18] M. Hardy, D. Feezell, S. Denbaars, and S. Nakamura. Group III-Nitride Lasers: A Materials Perspective. *Materials Today*, 14:408, 2011.
- [19] S. D. Carnevale, T. F. Kent, P. J. Phillips, A. T. M. G. Sarwar, C. Selcu, R. F. Klie, and R. C. Myers. Mixed Polarity in Polarization-Induced p-n Junction Nanowire Light-Emitting Diodes. *Nano Letters*, 13:3029, 2013.
- [20] N. Gogneau, P. Chrétien, E. Galopin, S. Guilet, L. Travers, J. C. Harmand, and F. Houzè. Impact of the GaN Nanowire Polarity on Energy Harvesting. *Applied Physics Letters*, 104:213105, 2014.
- [21] G. Naresh-Kumar, J. Bruckbauer, A. Winkelmann, X. Yu, B. Hourahine, P. R. Edwards, T. Wang, C. Trager-Cowan, and R. W. Martin. Determining GaN Nanowire Polarity and its Influence on Light Emission in the Scanning Electron Microscope. *Nano Letters*, 19:3863, 2019.
- [22] A. Minj, A. Cros, N. Garro, J. Colchero, T. Auzelle, and B. Daudin. Assessment of Polarity in GaN Self-Assembled Nanowires by Electrical Force Microscopy. *Nano Letters*, 15:6770, 2015.
- [23] L. Largeau, E. Galopin, N. Gogneau, L. Travers, F. Glas, and J. C. Harmand. N-Polar GaN Nanowires Seeded by Al Droplets on Si(111). *Crystal Growth & Design*, 12:2724, 2012.
- [24] M. Hetzl, M. Kraut, T. Hoffmann, and M. Stutzmann. Polarity Control of Heteroepitaxial GaN Nanowires on Diamond. *Nano Letters*, 17:3582, 2017.
- [25] T. Auzelle, C. Bougero, A. Minj, B. Haas, J. L. Rouviere, A. Cros, J. Colchero, and B. Daudin. The Influence of AlN Buffer Over the Polarity and the Nucleation of Self-Organized GaN Nanowires. *Journal of Applied Physics*, 117:245303, 2015.

- [26] M. Sobanska, N. Garro, K. Klosek, A. Cros, and Z. R. Zytckiewicz. Influence of Si Substrate Preparation Procedure on Polarity of Self-Assembled GaN Nanowires on Si(111): Kelvin Probe Force Microscopy Studies. *Electronics*, 9:1904, 2020.
- [27] M. Sumiya and S. Fuke. Review of Polarity Determination and Control of GaN. *MRS Internet Journal of Nitride Semiconductor Research*, 9:1, 2004.
- [28] V. G. Dubrovskii. *Nucleation Theory and Growth of Nanostructures*. Springer Berlin Heidelberg, 2014.
- [29] J. Zhang, Y. Zhang, K. Tse, B. Deng, H. Xu, and J. Zhu. New Approaches for Calculating Absolute Surface Energies of Wurtzite (0001)/(000-1): A Study of ZnO and GaN. *Journal of Applied Physics*, 119:205302, 2016.
- [30] D. Holec and P.H. Meyrhofer. Surface Energies of AlN Allotropes from First Principles. *Scripta Materialia*, 67:760, 2012.
- [31] S. M. Ko, J. H. Kim, Y. H. Ko, Y. H. Chang, Y. H. Kim, J. Yoon, J. Y. Lee, and Y. H. Cho. Growth Mechanism of Catalyst-Free and Mask-Free Heteroepitaxial GaN Submicrometer- and Micrometer-Sized Rods under Biaxial Strain: Variation of Surface Energy and Adatom Kinetics. *Crystal Growth & Design*, 12:3838, 2012.
- [32] K. W. Böer and U. W. Pohl. *Semiconductor Physics*. Springer International Publishing, 2018.
- [33] B. Du. Nguyen, A. M. Rausch, J. Steiner, P. Wellmann, and S. Sandfeld. On the Importance of Dislocation Flow in Continuum Plasticity Models for Semiconductor Materials. *Journal of Crystal Growth*, 532:125414, 2020.
- [34] Udo W Pohl. *Epitaxy of Semiconductors: Physics and Fabrication of Heterostructures*. Springer International Publishing, 2020.
- [35] J. E Van Nostrand, K. L. Averett, R. Cortez, J. Boeckl, C. E. Stutz, N. A. Sanford, A. V. Davydov, and J. D. Albrecht. Molecular Beam Epitaxial Growth of High-Quality GaN Nanocolumns. *Journal of Crystal Growth*, 287:500, 2006.
- [36] W. Borchardt-Ott. *Crystallography: An Introduction*. Springer-Verlag Berlin Heidelberg, 2012.
- [37] D. V. Beznasyuk, P. Stepanov, J. L. Rouvière, F. Glas, M. Verheijen, J. Claudon, and M. Hocevar. Full Characterization and Modeling of Graded Interfaces in a High Lattice-Mismatch Axial Nanowire Heterostructure. *Physical Review Materials*, 4:074607, 2020.
- [38] K. A. Bertness, N. A. Sanford, and A. V. Davydov. GaN Nanowires Grown by Molecular Beam Epitaxy. *IEEE Journal of Selected Topics in Quantum Electronics*, 17:847, 2011.

- [39] F. Meng, M. Estruga, A. Forticaux, S. A. Morin, Q. Wu, Z. Hu, and S. Jin. Formation of Stacking Faults and the Screw Dislocation-Driven Growth: A Case Study of Aluminum Nitride Nanowires. *ACS Nano*, 7:11369, 2013.
- [40] K. W. Kolasinski. Growth and Epitaxy. In *Surface Science: Foundations of Catalysis and Nanoscience, Third Edition*, pages 305–352. John Wiley & Sons, Ltd, 2012.
- [41] H. Lüth. *Solid Surfaces, Interfaces and Thin Films*. Springer, 2015.
- [42] R. Grinham and A. Chew. A Review of Outgassing and Methods for its Reduction. *Applied Science and Convergence Technology*, 26:95, 2017.
- [43] A. Prabaswara, J. Birch, M. Junaid, E. A. Serban, L. Hultman, and C. L. Hsiao. Review of GaN Thin Film and Nanorod Growth Using Magnetron Sputter Epitaxy. *Applied Sciences*, 10:3050, 2020.
- [44] K. Choi, M. Arita, and Y. Arakawa. Selective-Area Growth of Thin GaN Nanowires by MOCVD. *Journal of Crystal Growth*, 357:58, 2012.
- [45] R. S. Wagner and W. C. Ellis. Vapor-Liquid-Solid Mechanism of Single Crystal Growth. *Applied Physics Letters*, 4:89, 1964.
- [46] Z. M. Wang. Study of Nanowire Growth Mechanisms: VLS and Si Assisted. In H.D. Park and S.M. Prokes, editors, *One-Dimensional Nanostructures*, pages 1–16. Springer, 2008.
- [47] G. Suo, S. Jiang, J. Zhang, J. Li, and M. He. Synthetic Strategies and Applications of GaN Nanowires. *Advances in Condensed Matter Physics*, 2014:1, 2014.
- [48] M. Verma and R. Mukherjee. Nanoparticle Formation through Dewetting of a Solid-State Thin Film on a Substrate: A phase-Field Study. *Journal of Alloys and Compounds*, 835:155163, 2020.
- [49] A. J. Ferrer, A. Halajko, and G. G. Amatucci. Direct-Write Dewetting of High Melting Temperature Metals on Flexible Substrates. *Applied Sciences*, 9:3165, 2019.
- [50] J. Park, R. Navamathaven, and C. Lee. Size Effects of Nano-Pattern in Si(111) Substrate on the Selective Growth Behaviour of GaN by MOCVD. *Material Research Bulletin*, 47:836, 2012.
- [51] J. Li, C. Lu, B. Maynor, S. Huang, and J. Liu. Controlled Growth of Long GaN Nanowires from Catalyst Patterns Fabricated by "Dip-Pen" Nanolithographic Techniques. *Chemistry of Materials*, 16:1633, 2004.
- [52] K. W. Kolasinski. Catalytic Growth of Nanowires: Vapor-Liquid-Solid, Vapor-Solid-Solid, Solution-Liquid-Solid and Solid-Liquid-Solid Growth. *Current Opinion in Solid State and Materials Science*, 10:182, 2006.

- [53] J. Johansson, C. P. T. Svensson, T. Mårtensson, L. Samuelson, and W. Seifert. Mass Transport Model for Semiconductor Nanowire Growth. *The Journal of Physical Chemistry B*, 109:13567, 2005.
- [54] C. B. Maliakkal, N. Hatui, R. D. Bapat, B. A. Chalke, A. A. Rahman, and Bhattacharya A. The Mechanism of Ni-Assisted GaN Nanowire Growth. *Nano Letters*, 16:7632, 2016.
- [55] V.G. Dubrovskii, N.V. Sibirev, G.E. Cirlin, J.C. Harmand, and V.M. Ustinov. Theoretical Analysis of the Vapor-Liquid-Solid Mechanism of Nanowire Growth During Molecular Beam Epitaxy. *Physical Review E*, 73:021603, 2006.
- [56] A.I Persson, M.W. Larsson, S. Stenström, B.J. Ohlsson, L. Samuelson, and L.R. Wallenberg. Solid-Phase Diffusion Mechanism for GaAs Nanowire Growth. *Nature Materials*, 3:677, 2004.
- [57] Y. Cai, T.L. Wong, S.K. Chan, I.K. Sou, D.S. Su, and N. Wang. Growth Behaviours of Ultrathin ZnSe Nanowires by Au-Catalized Molecular-Beam Epitaxy. *Applied Physics Letter*, 93:233107, 2008.
- [58] J. Ristić, E. Calleja, S. Fernández-Garrido, L. Cerutti, A. Trampert, U. Jahn, and K. H. Ploog. On the Mechanisms of Spontaneous Growth of III-nitride Nanocolumns by Plasma-Assisted Molecular Beam Epitaxy. *Journal of Crystal Growth*, 310:4035, 2008.
- [59] T. Zywiets, J. Neugebauer, and M. Scheffler. Adatom Diffusion at GaN (0001) and (000 $\bar{1}$) surfaces. *Applied Physics Letters*, 73:487, 1998.
- [60] N. Gogneau, N. Jamond, P. Chrétien, F. Houzé, E. Lefeuvre, and M. Tchernycheva. From Single III-Nitride Nanowires to Piezoelectric Generators: New Route for Powering Nomad Electronics. *Semiconductor Science and Technology*, 31:103002, 2016.
- [61] S. Zhao and Z. Mi. Recent Advances on *p*-Type III-Nitride Nanowires by Molecular Beam Epitaxy. *Crystals*, 7:268, 2017.
- [62] K. A. Bertness, A. Roshko, L. M. Mansfield, T. E. Harvey, and N. A. Sanford. Mechanism for Spontaneous Growth of GaN Nanowires with Molecular Beam Epitaxy. *Journal of Crystal Growth*, 310:3154, 2008.
- [63] N. Gogneau, P. Chrétien, E. Galopin, S. Guilet, L. Travers, J. C. Harmand, and F. Houzé. GaN Nanowires for Piezoelectric Generators. *Physica Status Solidi RRL*, 8:414, 2014.
- [64] J. E. Kruse, L. Lymperakis, S. Eftychis, A. Adikimenakis, G. Doundoulakis, K. Tsagaraki, M. Androulidaki, A. Olziersky, P. Dimitrakis, V. Ioannou-Sougleridis, P. Normand, T. Koukoulou, T. Kehagias, P. Komninou, G. Konstantinidis, and A. Georgakilas. Selective-Area Growth of GaN Nanowires On SiO₂-Masked Si(111) Substrates by Molecular Beam Epitaxy. *Journal of Applied Physics*, 119:2224305, 2016.

- [65] A. Roshko, M. Brubaker, P. Blanchard, T. Harvey, and K.A. Bertness. Selective Area Growth and Structural Characterization of GaN Nanostructures on Si(111) Substrates. *Crystals*, 8:366, 2018.
- [66] R. Mata, K. Hestroffer, J. Budagosky, A. Cros, C. Bougerol, H. Renevier, and B. Daudin. Nucleation of GaN Nanowires Grown by Plasma-Assisted Molecular Beam Epitaxy: The Effect of Temperature. *Journal of Crystal Growth*, 334:177, 2011.
- [67] O. Landré, V. Fellmann, P. Jaffrennou, C. Bougerol, H. Renevier, A. Cros, and B. Daudin. Molecular Beam Epitaxy Growth and Optical Properties of AlN Nanowires. *Applied Physics Letter*, 96:061912, 2010.
- [68] S. Zhao, A. T. Connie, M. H. T. Dastjerdi, X. H. Kong, Q. Wang, M. Djavid, S. Sadaf, X. D. Liu, I. Shih, H. Guo, and Z. Mi. Aluminum Nitride Nanowire Light Emitting Diodes: Breaking the Fundamental Bottleneck of Deep Ultraviolet Light Sources. *Scientific Reports*, 5:8332, 2015.
- [69] H. Amano. MOCVD of Nitrides. In T. F. Kuech, editor, *Handbook of Crystal Growth (Second Edition)*, pages 683–704. North-Holland, 2015.
- [70] F. H. Yang. Modern Metal-Organic Chemical Vapor Deposition (MOCVD) Reactors and Growing Nitride-Based Materials. In *Nitride Semiconductor Light-Emitting Diodes (LEDs)*, pages 27–65. Elsevier Ltd, 2014.
- [71] J. An, X. Dai, Q. Zhang, R. Guo, and L. Feng. Gas-Phase Chemical Reaction Mechanism in the Growth of AlN during High-Temperature MOCVD: A Thermodynamic Study. *ACS Omega*, 5:11792, 2020.
- [72] R Köster. *Self-Assembled Growth of Catalyst-Free GaN Wires by Metal-Organic Vapour Phase Epitaxy*. PhD thesis, Université Joseph-Fourier - Grenoble I, 2010.
- [73] J. H. Kang, Q. Gao, P. Parkinson, H. J. Joyce, H. H. Tan, Y. Kim, Y. Guo, H. Xu, J. Zou, and C. Jagadish. Precursor Flow Rate Manipulation for the Controlled Fabrication of Twin-Free GaAs Nanowires on Silicon Substrates. *Nanotechnology*, 23:415702, 2012.
- [74] Y. Liu, Y. Peng, J. Guo, D. La, and Z. Xu. The Effect of V/III Ratio on the Morphology and Structure of GaAs Nanowires by MOCVD. *AIP Advances*, 8:55108, 2018.
- [75] S. Paiman, Q. Gao, H. Joyce, Y. Kim, H. H. Tan, C. Jagadish, X. Zhang, Y. N. Guo, and J. Zou. Growth Temperature and V/III Ratio Effects on the Morphology and Crystal Structure of InP Nanowires. *Journal of Physics D: Applied Physics*, 43:44, 2010.
- [76] Y. H. Ra, R. Navamathavan, Y. M. Lee, D. W. Kim, J. S. Kim, I. H. Lee, and C. R. Lee. The Influence of the Working Pressure on the Synthesis of GaN Nanowires by Using MOCVD. *Journal of Crystal Growth*, 312:770, 2010.

- [77] V. Cimalla, Ch. Foerster, D. Cengher, K. Tonisch, and O. Ambacher. Growth of AlN Nanowires by Metal Organic Chemical Vapour Deposition. *Physica Status Solidi B*, 243:1476, 2006.
- [78] E. A. Serban, J. Palisaitis, M. Junaid, L. Tengdelius, H. Högberg, L. Hultman, P. O. Å. Persson, J. Birch, and C.L. Hsiao. Magnetron Sputter Epitaxy of High-Quality GaN Nanorods on Functional and Cost-Effective Templates/Substrates. *Energies*, 10:1322, 2017.
- [79] M. Junaid, C. L. Hsiao, Y. T. Chen, J. Lu, J. Palisaitis, P. Persson, L. Hultman, and J. Birch. Effects of N₂ Partial Pressure on Growth, Structure, and Optical Properties of GaN Nanorods Deposited by Liquid-Target Reactive Magnetron Sputter Epitaxy. *Nanomaterials*, 8:223, 2018.
- [80] E. A. Serban, J. Palisaitis, P. O. Å. Persson, L. Hultman, J. Birch, and C. L. Hsiao. Site-controlled Growth of GaN Nanorod Arrays by Magnetron Sputter Epitaxy. *Thin Solid Films*, page 950, 2018.
- [81] C. H. Verbeno, A. C. Krohling, T. C. Freitas, T. E. P. Bueno, M. A. Schettino, J. C. González, C. Larica, V. P. Nascimento, and E. C. Passamani. Tungsten Self-Organization Nanowires Prepared by DC Magnetron Sputtering. *Applied Surface Science*, 464:360, 2019.
- [82] S. Mukherjee and D. Gall. Structure Zone Model for Extreme Shadowing Conditions. *Thin Solid Films*, 527:158, 2013.
- [83] A. Wierzbicka, Z. R. Zykiewicz, S. Kret, J. Borysiuk, P. Dluzewski, M. Sobanska, K. Klosek, A. Reszka, G. Tchutchulashvili, A. Cabaj, and E. Lusakowska. Influence of Substrate Nitridation Temperature on Epitaxial Alignment of GaN Nanowires to Si(111) Substrate. *Nanotechnology*, 24:035703, 2013.
- [84] S. S. Kushvaha, H. Xu, W. Xiao, H. L. Zhang, A. T. S. Wee, and X. S. Wang. Scanning Tunneling Microscopy Investigation of Growth of Self-Assembled Indium and Aluminum Nanostructures on Inert Substrates. *Thin Solid Films*, 517:4540, 2009.
- [85] L. Bardotti, P. Jensen, A. Hoareau, M. Treilleux, B. Cabaud, A. Perez, and F. C. S. Aires. Diffusion and Aggregation of Large Antimony and Gold Clusters Deposited on Graphite. *Surface Science*, 367:276, 1996.
- [86] K. W. Kolasinski. *Surface Science : Foundations of Catalysis and Nanoscience*. Wiley, 2012.
- [87] K. Kyuno and G. Ehrlich. Diffusion and Dissociation of Platinum Clusters on Pt(111). *Surface Science*, 437:29, 1999.
- [88] W. M. Haynes. *CRC Handbook of Chemistry and Physics*. CRC Press, 2017.
- [89] J. Tournet. Growth and Characterization of Epitaxial Al Layers on GaAs and Si Substrates for Superconducting CPW Resonators in Scalable Quantum Computing Systems. Master's thesis, University of Waterloo, 2015.

-
- [90] H. Liu, Y. F. Zhang, D. Y. Wang, M. H. Pan, J. F. Jia, and Q. K. Xue. Two-Dimensional Growth of Al Films on Si(111)- 7×7 at Low-Temperature. *Surface Science*, 571:5, 2004.
- [91] K. J. Taylor, C. L. Pettiette, M. J. Craycraft, O. Chesnovsky, and R. E. Smalley. UPS of Negative Aluminum Clusters. *Chemical Physics Letters*, 152, 1988.
- [92] B. Samanta, T. Sengupta, and S. Pal. Aluminum Cluster for CO and O₂ Adsorption. *Journal of Molecular Modeling*, 25, 2019.
- [93] J. A. Thornton. Influence of Apparatus Geometry and Deposition Conditions on the Structure and Topography of Thick Sputtered Coatings. *Journal of Vacuum Science & Technology*, 11:666, 1974.
- [94] F. D. Pietrantonio, M. Fosca, M. Benetti, D. Cannatà, C. Verona, R. Teghil, A. De Bonis, and J. V. Rau. Flower-Like Aluminium Nitride Nanostructures Deposited by RF Magnetron Sputtering On Superhard Rhodium Boride Films. *Applied Physics A*, 125:681, 2019.
- [95] P. B. Barna and M. Adamik. Fundamental Structure Forming Phenomena of Polycrystalline Films and the Structure Zone Models. *Thin Solid Films*, 317:27, 1998.

GROWTH PARAMETERS OF SAMPLES GROWN USING DC MAGNETRON SPUTTERING

Various parameters need to be taken into account when producing samples in the Flextura 200 system, thus, a more comprehensive explanation of the processes will be given here. When producing a sample only a few parameters are usually of interest: the temperature, process pressure, Ar flow, N flow, sputtering power and deposition time. But for analysis of the initial growth, the preliminary process before the main deposition must be taken into consideration as well. These are ramp up/down time of the magnetron, target cleaning time and reactive gas time before the sample shutter is removed.

During the ramp up process the plasma will ignite and initiate sputtering when a sufficient field strength is achieved. As the specific moment of this is unknown, the time span of this process is desired to be as small as possible. It should be noted that too low ramp time minimises the lifetime on the magnetron controller, and can lead to short circuits in the electronics.

Following the ramp up process is the target cleaning process. Here, the ionised Ar atoms in the ignited plasma are bombarded into the target for a predetermined amount of time. As this process is running before the sample shutter is removed, the idea is to sputter off any contaminating materials such as N from previous depositions or O from leakage or sample exchange.

Lastly before the actual sputter deposition where the sample shutter is removed, the reactive gas process is initiated. This process is only being run if a pre-set value of reactive gases is present for the main deposition process. As this process essentially is target cleaning with reactive gases, it will be referred to as part of the target cleaning process.

After the target cleaning process the sample shutter is removed and the main deposition begins. When the main deposition is finished, the magnetron ramps down and the sample is removed from the chamber. As mentioned the target cleaning process and reactive gas process is considered the same, thus, the parameter given in Tab. A.1 for these two processes is called [material] deposition with shutter, whereas the main sputter deposition is called [material] deposition without shutter.

Table A.1 Flextura parameters under production of samples related to the islands growth investigations.

Sample Name	Temperature [°C]	Process Pressure [Pa]	Ar Flow [sccm]	N Flow [sccm]	Partial N Concentration	Sputtering Power [W]	Ramp Up Time [s]	Al Deposition with Shutter [s]	AlN Deposition with Shutter [s]
AlNW60	450/43	0.4	6.9	14.5	0.68	300	1	0	20
AlNW60	703/38	0.4	18.3/7	0/14.5	0/0.67	300	1	0	20
AlNW10	700/883	0.41/0.4	19/6.5	0/14.5	0/0.69	300	1/1	0/0	0/20
IslAl160	703	0.4	18.1	0	0.00	300	20	160	0
IslAlNoShutter	678	00.41	19	0	0.00	300	1	0	0
IslAlNOnly	707	00.38	6.5	14.5	0.69	300	1	0	50
IslAl	711	0.4	18.3	0	0.00	300	20	20	0
IslAl140	702	0.4	18.5	0	0.00	300	20	40	0
IslAlN	706	0.4	14.8/5.5	0/14.5	0.73	300	10	0	20
IslRT	20	0.4	8	14.5	0.64	300	20	20	20
Isl5	709	0.4	7	14.5	0.67	300	20	20	20
Isl15	716	0.4	8	14.5	0.64	300	20	20	20
Isl30	753	0.4	5.9	14.5	0.71	300	20	20	20
Isl60	701	0.4	5.2	14.5	0.74	300	20	20	20
Isl180	752	0.4	5.8	14.5	0.71	300	20	20	20
Isl360	720	0.4	7.5	14.5	0.66	300	20	20	20
Isl720	659	0.4	7.6	14.5	0.66	300	20	20	20
RTHP	35	0.85	19.9	20	0.50	300	20	20	20
RT	27	0.4	11.7	10	0.46	300	20	20	20
GR07	697	0.4	5.2	14.5	0.73	300	20	20	20

Table A.1 continued

Sample Name	Al Deposition without Shutter [s]	AlN Deposition without Shutter [s]	Ramp Down Time [s]	Total Time [s]
Al ₁ NW60	0	3600	1	3622
Al ₁ NW60	40/0	3600	1	42/3622
Al ₁ NW10	40/0	0/600	1/1	42/622
Is ₁ Al ₁ 60	0	0	20	200
Is ₁ Al ₁ 60	40	0	1	42
Is ₁ Al ₁ N ₀ Shutter	0	0	1	52
Is ₁ Al ₁ N ₀ Only	0	0	20	60
Is ₁ Al ₁	0	0	20	80
Is ₁ Al ₁ 40	0	0	20	41
Is ₁ Al ₁ N	0	1	10	110
Is ₁ RT	0	30	20	85
Is ₁ 5	0	5	20	95
Is ₁ 15	0	15	20	110
Is ₁ 30	0	30	20	140
Is ₁ 60	0	60	20	260
Is ₁ 180	0	180	20	440
Is ₁ 360	0	360	20	800
Is ₁ 720	0	720	20	3680
RTHP	0	3600	20	3680
RT	0	3600	20	3680
GR07	0	3600	20	3680

GROWTH PARAMETERS OF SAMPLES GROWN USING MOCVD

Table B.1 Parameters for the MOCVD system during production of samples related to attempts of AlN nanowire growth.

Sample Name	Temperature [°C]	Rotation [rpm]	Process Pressure [Torr]	NH ₃ Flow [sccm]	TMAI Flow [sccm]	Time [s]
MOCVD1	800	500	50	500	20	1200
MOCVD2	1000	500	50	500	20	1500
MOCVD3	1000	500	50	300	20	3600
MOCVD4	1000	500	50	500	20	3600
MOCVD5	1000	500	50	500	17	3600
MOCVD6	1090	500	50	500	20	3600
MOCVD7	1090	500	200	2000	20	3600
MOCVD8	1090	500	200	500	5	3600

GROWTH PARAMETERS OF SAMPLES GROWN USING MBE

Table C.1 Known parameters for the MBE grown NWs from the Institute of Physics at the Polish Academy of Sciences.

Sample Name	Temperature [°C]	Temperature Gradient Direction	N/Ga	Substrate Resistivity [Ωcm]
MBE1	790	positive	2	0.01 – 0.02
MBE2	Unknown	negative	Unknown	0.01 – 0.02
MBE3	794	negative	Unknown	1 – 30
MBE4	798	negative	2	1 – 30

COVERAGE ANALYSIS OF RAMIFIED ISLANDS

In order to use SEM images for a quantitative coverage analysis, different aspects must be into account. First the contrast and brightness has been adjusted to span over the full colour scale achieving 256 data points and making it possible to standardise the following procedure for all sample. Then, a flattening process of the surface has been conducted, here the images were treated as a matrix where each entry describes the colour, going from 0 (black) to 255 (white). A second degree polynomial fit was applied to each column were all entries with values more than 100 below the maximum had been excluded, to avoid unwanted distortion from the islands. This procedure was then repeated five times. A new threshold value was then determined for each sample, to precisely describe when an entry corresponded to an island. All entries below that value were then plotted over the flattened image to visualise the efficiency of the process, and a manual verification of the method was conducted.

An example of the finished result of the analysis, conducted on the measurement displayed in Fig. 6.1(a), can be seen in Fig. D.1 where the entries determined as "island" is blue. The coverage was then calculated as island entries per number of overall entries or matrix size.

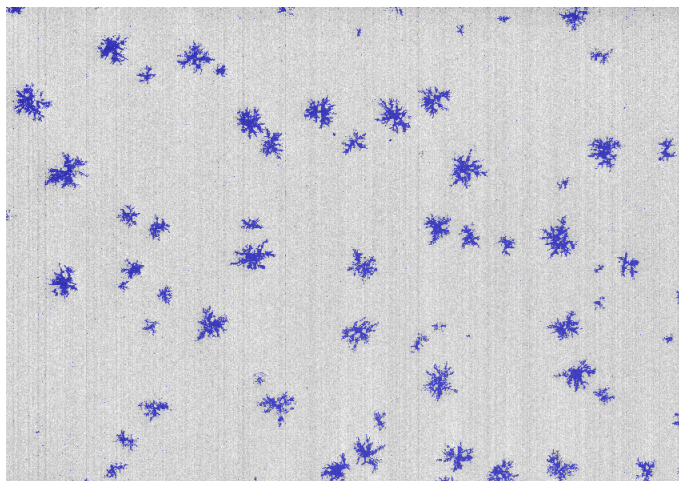


Figure D.1 Product of coverage analysis used on SEM image of ramified islands. Blue areas corresponds to the areas recognised as "island". Original image can be found in Fig. 6.1(a).

AL CLUSTER-CHAIN FORMATION

In the study by Kushvaha et al. [84], scanning tunneling microscopy (STM) images of Al cluster-chains were found, as shown in Fig. E.1(a). The string-like features arose from the local step edges of the substrate, which controlled the width of the chains. Increasing the deposition time lead to the formation of triangular clusters forming either between or on the sides of existing cluster-chains, as found in Fig. E.1(b).

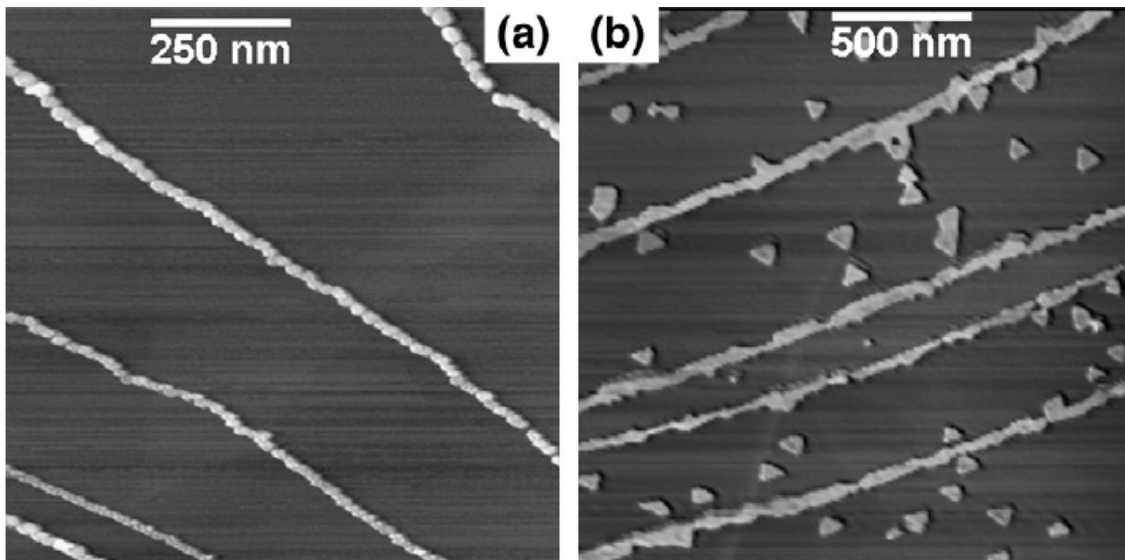


Figure E.1 STM image of cluster-chains of Al (a) string-like formation of cluster-chains after low deposition time and (b) formation of triangular islands situated between and on the cluster-chains at increased deposition time. Reprinted from [84], with permission from Elsevier.

THE STRUCTURE ZONE MODEL

The morphology of thin films and NWs grown by magnetron sputtering are highly dependent on the deposition pressure and substrate temperature. This is made evident from the work of J. A. Thornton [93] who developed the SZM. The SZM correlates the Ar pressure during deposition and the homologous temperature, $\theta = T/T_m$, where T is the substrate and T_m is the melting point of the deposited material, with the internal structure of thin films grown by magnetron sputtering. An increase of substrate temperature leads to increased diffusion lengths, which alters the microstructure. The SZM is illustrated in Fig. F.1, where the Zone I and T are of particular interest when trying to achieve NW growth, as these zones are characterised by tapered columnar structures separated by voids. The low temperatures in these zones makes growth predominantly controlled by the direction and flux of the incoming particles, along with shadowing effects, as little diffusion occurs.

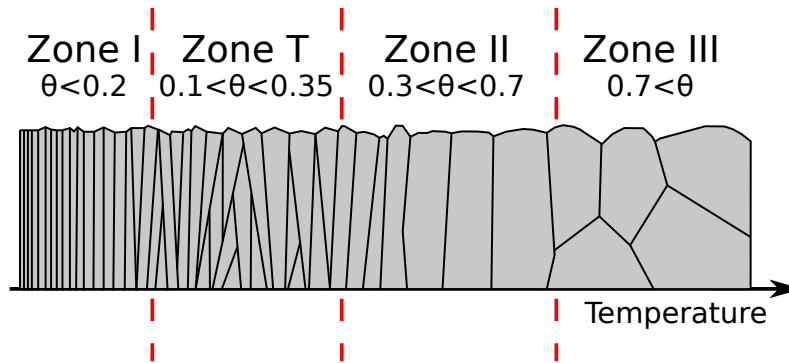


Figure F.1 The four zones of the SZM and their corresponding homologous temperature θ . Inspired by [95].

DISTRIBUTION ANALYSIS OF NANOWIRE CPD

By the adopted convention, N-polar NWs should lead to a lower CPD value compared to Ga-polar, which should make it possible to determine if both polarities are present from the CPD map. A difference in CPD values are not readily seen in the CPD map of Fig. 6.25(b), but a more elaborate analysis may help shed light on this issue. A histogram of the counts of measured CPD values has been plotted, revealing the presence of a skewed distribution of relative CPD values. It is believed that the main contributions arise from the material surrounding the NWs, along with polar NWs which is responsible from the skewness. A final contribution is found from the bump in the number of counts close to the apex of the histogram data. The CPD distribution is a convolution of three Gaussian distributions, as shown in Fig G.1.

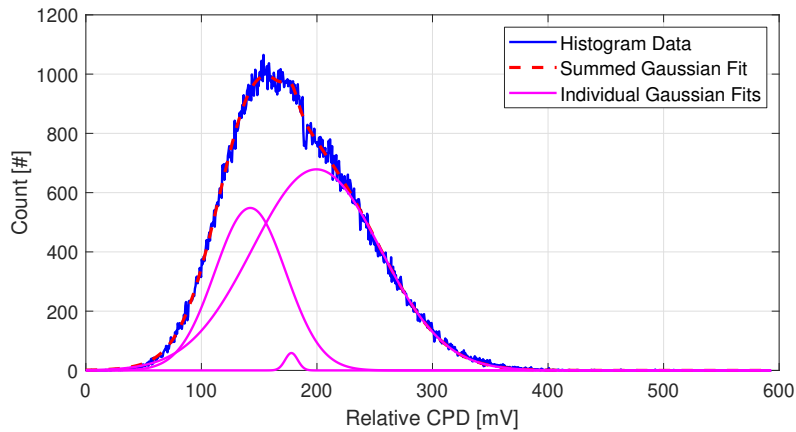


Figure G.1 Histogram of relative CPD taken from the image displayed in 6.25(b), along with a fit constructed from three individual Gaussian distributions.

The mean of the relative CPD for the left-most Gaussian fit is believed to stem from the contribution from the material surrounding the NWs, due to its relatively high number of counts. The Gaussian fit to the right with an even higher mean relative CPD is believed to be the contribution from Ga-polar NWs, as these should result in the highest CPD value. The high number of counts for this fit tells that the sample has a large majority of Ga-polar NWs. The origin of the Gaussian peak in the middle was hoped to be the presence of N-polar NWs, however the low number of counts makes this point unclear. It is more possible that it is related to the fitting procedure, or several NWs which are affected by oxidation leading to differences in their CPD.